DEVELOPMENT AND USE OF CONTACTLESS MAGNETIC MANIPULATION METHODOLOGIES FOR THE FORMATION OF 3D CARDIAC MODELS

A Thesis Submitted to
the Graduate School of Engineering and Sciences of
İzmir Institute of Technology
in Partial Fulfillment of the Requirement for the Degree of

DOCTOR OF PHILOSOPHY

in Bioengineering

by
Rabia ÖNBAŞ

December 2022
İZMİR

ACKNOWLEDGEMENTS

First and foremost, I would like to express my sincere gratitude to my supervisor Assoc. Prof. Dr. Ahu Arslan Yıldız for her guidance, experience, encouragement, and motivation throughout my Ph.D. thesis. I am also grateful to the thesis monitoring committee members Prof. Dr. Funda Tıhmınlıoğlu and Prof. Dr. Pınar Akan for their valuable comments and contributions during meetings. I had a chance to collaborate on a project during my Ph.D. thesis with the Department of Applied Stem Cells Technologies at the University of Twente, The Netherlands. I would like to thank Prof. Dr. Robert Passier and Dr. Verena Schwach for supervising me during the project. Also, I would like to thank AST research group members.

I would like to gratefully acknowledge The Scientific and Technological Research Council of Turkey with the grants of 2211-A National Ph.D. Scholarship Program and 2214-A International Doctoral Research Fellowship Program. Also, I would like to acknowledge the support of the Council of Higher Education Ph.D. Scholarship at 100/2000 program in the field of Biomaterials and Tissue Engineering. Moreover, financial support from the IZTECH-Scientific Research Project (2020IYTE0006) and The Scientific and Technological Research Council of Turkey (119Z569) are gratefully acknowledged.

I am very thankful to Biomimetics Research Group; Basak Çoban, Alper Baran Sözmen, Duygu Arslantaş, Ece Özmen, Meltem Güzelgülgen, Özum Yıldırım, Rumeysa Bilginer, and all current and alumni members for creating a friendly working environment with their friendship, help, and motivation.

I also want to express my special thanks to my friends Zulal Kızılaslan, Ecem Saygılı, Ceyhan Deliklitaş, and İrem Cemre Türü for their understanding, support, and motivation even though we were not living in the same city and country.

The biggest thanks are to my beloved family; my mother Ayşe Önbaş, my father Mehmet Akif Önbaş, and my sister Şerife Ardıç for their endless love, support, and encouragement whole my life.

ABSTRACT

DEVELOPMENT AND USE OF CONTACTLESS MAGNETIC MANIPULATION METHODOLOGIES FOR THE FORMATION OF 3D CARDIAC MODELS

In this thesis, two contactless magnetic manipulation methodologies were introduced, which are magnetic levitation (MagLev) and biopatterning techniques. The optimization steps of both techniques were completed with NIH/3T3 mouse fibroblast cells. Later, 3D cardiac models were developed using H9c2 rat cardiomyocytes. For the MagLev technique, tunable 3D spheroids were obtained with changing initial cell seeding number, gadobutrol concentrations, and culturing time. For the biopatterning approach, a new bio-ink formulation, which comprises alginate, magnetic nanoparticles, and cells, was developed. Further, biopatterned cellular structures were fabricated in different shapes such as discs, rings, and rectangles under an external magnetic field. Later, characterization was done successfully via immunostaining of collagen I, F-actin, and DAPI. Moreover, cardiac-specific markers; cardiac troponin T and MYH6 were analyzed for both 3D cardiac spheroids and patterned 3D cardiac structures. Finally, doxorubicin was applied to evaluate the drug responses. IC_{50} values were calculated as 14.7 μM and 8.1 μM for 3D cardiac spheroids and 3D cellular structures respectively, while standard 2D cell culture was 3.5 μM which indicated 3D cardiac models were more resistant to drug exposure. In the last part of thesis, patterned 3D cardiac structures were fabricated using co-cultured hiPSC-derived cardiomyocytes and cardiac fibroblast cells via biopatterning methodology. Characterization was carried out successfully by immunostaining of α-actinin, collagen I, Cx-43, Troponin T, and DAPI. Taken together, to fabricate 3D cell culture models, MagLev and biopatterning-based contactless manipulation methodologies may be good alternatives to conventional 2D cell culture methods for tissue engineering applications, especially for drug screening.

ÖZET

3B KARDİYAK MODELLERİN OLUŞTURULMASI İÇİN TEMASSIZ MANYETİK MANİPÜLASYON METODOLOJİLERİNİN GELİŞTİRİLMESİ VE KULLANILMASI

Bu tezde, manyetik levitasyon ve manyetik biyo-kalıplandırmaya dayalı iki yeni yöntem geliştirilmiştir. Her iki tekniğin optimizasyon basamakları NIH/3T3 hücreleri ile gerçekleştirilmiştir. Optimizasyon aşamasından sonra H9c2 rat kardiyomiyosit hücreleri kullanılarak 3 boyutlu (3B) kardiyak modeller oluşturulmuştur. Manyetik levitasyon tekniği ile başlangıç hücre sayısı, gadobutrol konsantrasyonu ve kültür süresi degiştirilerek boyutları ayarlanabilir 3B sferoidler elde edilmiştir. Biyo-kalıplandırma yönteminde ise aljinat, manyetik nanopartikül ve hücre içeren biyomürekkep formülasyonu geliştirilmiştir. Ardindan, 3B hücresel yapılar disk, halka ve dikdörtgen şeklinde elde edilmistir. Karakterizasyon aşamasında ise kolajen I, F-aktin ve DAPI immun boyama ile başarılı bir şekilde analiz edildi. Ayrıca bunlara ek olarak kardiyak troponin T ve MYH6 kardiyak spesifik belirteçleri gösterildi. Son olarak, 3B kardiyak modellerin ilaç yanıtlarının değerlendirilmesi için doksorubusin uygulanmıştır. Manyetik levitasyon ve manyetik biyo-kalıplandırma yöntemleri ile elde edilen 3B kardiyak modeller için IC_{50} değerleri sırasıyla 14.7 µM ve 8.1 µM olarak elde edilmiştir. Standard 2B hücre kültürü için ise IC_{50} degeri 3.5 µM olarak hesaplanmıştır. 3B kardiyak modeller 2B kontrol grubu ile karşılaştırıldığında ilaç uygulamasına daha çok direnç göstermektedir. Tezin son aşamasında, 3B kardiyak yapılar birlikte kültürlenen WTC kardiyomiyosit ve kardiyak fibroblast hücreleri kullanılarak biyokalıplandırma yöntemi ile elde edilmiştir. Kardiyak yapının karakterizasyonu ise α-aktinin, kolajen-I, Cx-43, Troponin T, and DAPI immun boyama yöntemi ile gerçekleştirilip başarılı bir şekilde gözlenmiştir. Bu sonuçlar göz önüne alındığında manyetik levitasyon ve manyetik biyo-kalıplandırma yöntemi ile oluşturulan 3B kardiyak modellerin birçok doku mühendisliği uygulamaları özellikle ilaç tarama çalışmaları için geleneksel yöntemlerle karşılaştırıldığında iyi bir alternatif olabilecektir.

Dedicated to my family…

TABLE OF CONTENTS

LIST OF FIGURES

Figure **Page**

Figure **Page**

Figure **Page**

Figure **Page**

Figure **Page**

Figure **Page**

LIST OF TABLES

Table **Page**

CHAPTER 1

INTRODUCTION

1.1. Motivation and Scope of the Thesis

In this thesis, new methodologies based on contactless magnetic manipulation approaches were developed to fabricate 3D cardiac models for drug screening studies. For this aim, magnetic levitation (MagLev) and biopatterning methodologies were utilized to fabricate 3D cardiac models. These methodologies provide biofabrication of spheroids and patterned 3D cellular structures in rapid, easy, and cost-effective way with simple components.

Here, specific aims of the thesis are listed;

- Development of a new MagLev setup and optimization of parameters to obtain 3D spheroids using NIH/3T3 cells
- Biofabrication of 3D cardiac spheroids using H9c2 rat cardiomyocytes via MagLev methodology, and investigating the doxorubicin (DOX)-induced cardiotoxicity through this model
- Development of a new biopatterning methodology to fabricate biopatterned 3D cellular structures and optimization of parameters by experimental design models
- Biofabrication of biopatterned 3D cardiac structures using H9c2 rat cardiomyocytes via developed bipatterning methodology and investigating the DOX-induced cardiotoxicity on this model
- Biofabrication of biopatterned 3D cardiac structures using hiPSC-derived cardiomyocytes via developed biopatterning methodology and investigating the functionality of cardiac model

The novelty of this thesis is the biofabrication of 3D cardiac models using MagLev and magnetic biopatterning methodologies for DOX induced cardiotoxicity. Overall, results indicated that 3D cardiac models were more resistant to drug exposure

compared to conventional 2D cell culture. These above mentioned methodologies can be considered as an alternative route of fabricating 3D cardiac models for cardiac tissue engineering applications, particularly drug screening studies.

1.2. Tissue Engineering

Traditional tissue engineering consists of the principle of engineering and life sciences to develop biological tissues by applying three principles, which are isolation of cells and adding appropriate signal molecules and materials to put into cells. [1] The main goal of tissue engineering is to fabricate tissues with their capacity to function, grow, repair, and remodel. [2] The development of traditional tissue engineering or, in other words, scaffold-based tissue engineering is strongly related to the use of bioactive materials for the goal of tissue repair. [3] To achieve this goal, it is important to create a three-dimensional environment which can mimic the natural extracellular matrix (ECM) of the tissue and represent specific surface chemistries, architectures, and degradation properties; in that way, cells are able to attach, migrate, proliferate, and differentiate. [4–6] An ideal scaffold design that also refers to matrix, construct, and artificial ECM should also carry main characteristics such as biocompatibility, biodegradability, and mechanically appropriate properties. Once the scaffold interacts with the physiological environment, ECM proteins of fibronectin and vitronectin are non-specifically adsorbed on to it. Integrins are known as the cell membrane proteins of cells that indirectly interact with scaffold surfaces with the help of the adsorbed ECM proteins. Specific domains of adsorbed ECM proteins arginine-glycine-aspartate (RGD) and Proline-Histidine-Serine-Arginine-Asparagine (PHSRN) bind to integrin to trigger cell proliferation and differentiation. Therefore, scaffold surface properties are critical and significant in that they affect ECM protein adsorption and act on cell behaviour and function. [6–9] Cell interaction is strongly connected with the surface properties of the scaffold such as a rough surface, and high surface free energy triggers cell adhesion and proliferation, a positive surface charge feature that positively affects cell adhesion due to the negative charge of cells. Amino, carboxy sulfonic, and acyl amino groups of surface chemical structures and hydrophilic surfaces benefit cell adhesion and growth. [6,10]

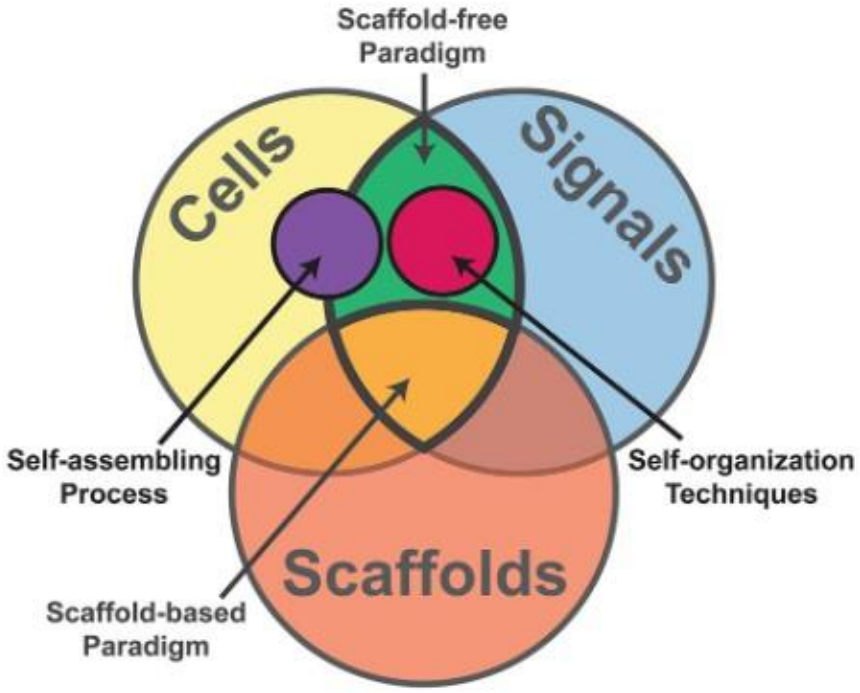

Figure 1.1. Traditional tissue engineering and, as a new approach, scaffold-free engineering with their components. [11]

Recently, a new approach "scaffold-free tissue engineering" was introduced, which does not need a scaffold for cell seeding or adherence to fabricate functional tissues, as given in Figure 1.1. This approach is mainly comprised of many steps, which are cell condensation, cell proliferation, cell differentiation, ECM production, and tissue maturation. Also, scaffold tissue engineering has two sub-categories: self-organization and self-assembly. Self-organization is defined as the process that occurs via the application of external forces. Contrary to the self-organization process, which is an open system, the self-assembly process occurs without applying external forces, which are called a closed system. [11,12]

Scaffold-free tissue engineering has various advantages over traditional scaffold-based tissue engineering. First, it does not require any harsh processes to produce a scaffold, which avoids the formation of cytotoxicity. Also, scaffold-free tissue engineering decreases the foreign material-associated immune response and release of by-products during degradation without utilizing any materials. During the

fabrication stages, it allows for a high degree of cell-cell interaction that results in increased ECM production. [12,13]

1.3. Cardiac Tissue Engineering

The aims of cardiac tissue engineering can be classified into two groups to treat cardiovascular diseases: i) treatment and repair of the heart via the implantation of fabricated functional cardiac tissue; ii) developing *in vitro* cardiac tissues for both healthy and diseased cardiac tissues as in *in vitro* models. [14,15] Cardiovascular diseases are one of the main reasons for deaths worldwide. Heart failure is a process that starts with damage to the heart muscle. The heart cannot repair itself because adult heart muscle cells (cardiac myocytes) cannot divide; thus, it is not possible for the heart to replace injured tissue. [16]

The heart is a very complex organ that has four heart chambers and related valves that control the flow of blood in ventricular cardiac muscle fibres to generate force to pump blood to the body. [17] The sinoatrial node is responsible for the generation of action potential, and the nervous system modulates the frequency. [18] To mimic and recreate the heart's architecture for *in vitro* or *in vivo* purposes is challenging. Also, it would be costly and unnecessary for drug screening studies. Preferably, 3D models of the heart focus mainly on mimicking the structures within the myocardium, which provides electrical propagation and force in the ventricle as a minimal functional unit of the heart, and can thus represent and model the drug responses and disease conditions, as given in Figure 1.2. [19] In the myocardium, cardiomyocytes make up 70% to 85% of the heart's volume. [20] The myocardium not only contains cardiomyocytes but also varied significant cell types such as conduction cells, endothelial cells, fibroblasts, and immune cells which form particular structural arrangements. [21] Moreover, myocardial ECM contributes to creating a complex 3D structure and also reinforces cells during contraction which are fibrous proteins (collagen, elastin), adhesive glycoproteins (laminin, fibronectin), and proteoglycans. [22]

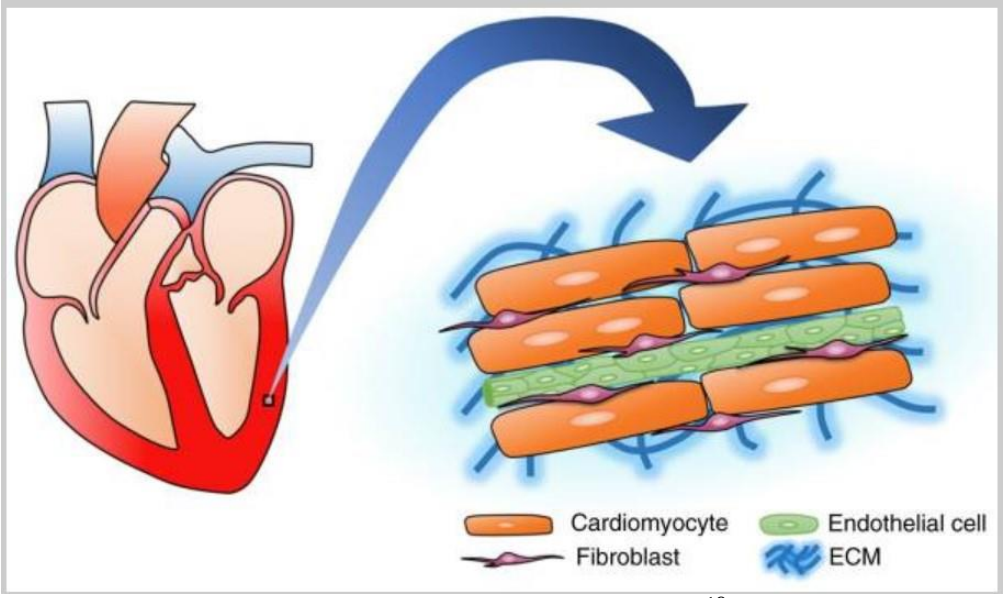

Figure 1. 2. The cardiac microenvironment. [19]

In conventional cardiac tissue engineering, cardiac cells cultured with scaffolds or hydrogels are used and cultured in bioreactors to mimic the ECM of an *in vivo* environment. Both natural and synthetic polymers are used to fabricate scaffolds. [23–25] On the other hand, decellularized tissues and scaffold-free approaches have been used to fabricate engineered cardiac tissues. [26–28] Lately, stem cells were involved in the fabrication of cardiac tissues to create more realistic *in vitro* models for drug screening and disease models. [15] Recently vascularized 3D iPSC CM tissues were fabricated by a newly developed filtration- Layer-by-Layer (LbL) technique. This technique provides fabrication of nanometer-sized extracellular matrices (ECM), fibronectin, and gelatin (FN–G), films onto iPSC CM surfaces without any damage and with high yield. The fabricated FN–G nanofilms interacted with integrin molecules on the cell membrane to construct 3D-tissues. It was also stated that adding normal human cardiac fibroblasts (NHCFs) into the iPSC–CM tissues modulated organization and synchronous beating depending on NHCF ratios. Moreover, blood capillary-like networks in 3D iPSC CM tissues were obtained. To evaluate the drug response of the vascularized 3D iPSC CM tissues, DOX was applied. Toxicity responses of the vascularized 3D iPSC CM tissues were significantly different compared to 2D iPSC CM cells. It was concluded that the constructed vascularized 3D iPSC CM tissues would be a promising tool for tissue regeneration and drug screening studies. [29] Another scaffold-based study was introduced

using synthetic material to fabricate organized neo-myocardium constructs via an electrospinning technique for cardiac tissue regeneration. For this aim, the biocompatibility of elastomeric electrospun degradable polar/hydrophobic/ionic polyurethane (D-PHI) composite scaffold was investigated using human-induced pluripotent stem cell-derived cardiomyocytes (hiPSC-CMs). High cell viability was observed for 7 days culture on the scaffolds with nanofibres oriented in aligned or random directions. Aligned sarcomeres oriented parallel to the direction of the fibers, while the cells on random scaffolds and a tissue culture polystyrene control did not demonstrate such an organized morphology. These results support that D-PHI elastomeric scaffolds provide significant cardiomyocyte characteristics for cardiac tissue engineering applications. [30] Also, scaffold-free approach was developed via 3D bioprinter using hiPSC-CMs. To evaluate the drug response of fabricated 3D cardiac constructs contractile force and beating rate were measured by analyzing changes for the movement of the needle tip. Cardiotoxicity was evaluated by applying DOX and low cell viability was obtained. These results support that utilized approach can be an alternative to current methods for the measurement of the contractile force. [31]

1.3.1. Cell Sources to Engineer Cardiac Tissue

To screen drug candidates for cardiotoxicity, various cell lines have been widely used such as H9c2 (myoblast cells, non-beating), HL-1 (arterial cells, beating), and AC16 (ventricular cell line, beating). H9c2 is a cardiomyoblast cell line obtained from an embryonic rat heart, often used as an alternative for cardiomyocytes in *in vitro* studies on, for instance, cardiotoxicity and stress-induced hypertrophy since its morphological parameters are similar to immature embryonic cardiomyocytes in terms of cardiac-specific genes. [32–35] This cell line, which has multinucleated cells, has been used as a model cell line due to its electrophysiological and biochemical properties that closely mimic native cardiomyocytes. [36] However, the use of H9c2 cell lines is limited in tissue engineering because they lack a beating feature due to the absence of contractile proteins, gap junctions, T-tubules, and myofibrils with organized sarcomeres. [37,38] On the other hand, stem cell-derived CMs offer a promising alternative to fabricating *in vitro* models for cardiac development and disease. [39,40] Moreover, stem cells allow us to obtain cells from humans without a tissue biopsy. Stem cells are

defined as cells that can self-renew and have the potential to differentiate into specialized cell types. The types of stem cells are known as embryonic stem cells (ESCs), induced pluripotent stem cells (iPSCs), and adult stem cells (ASCs) and are used for drug testing and disease modelling studies. [41,42] Human pluripotent stem cells can be produced from human embryos or somatic cells by reprogramming. Especially in human pluripotent stem cell lines, both hESC or hiPS cells are seen as encouraging for drug discovery since they can be obtained through healthy controls and can form the basis of a disease model via gene targeting. [43]

1.4. Drug-Induced Cardiotoxicity

Cardiovascular disease (CVD) is one of the main health problems that affect many people worldwide. [44,45] According to records, in the United States (2011), of 800.000 people that were killed by CVDs, approximately 60% of these were known as coronary heart disease (such as myocardial infarction) and hypertensive heart disease. Various interventional and pharmacological agents have been used to treat these CVDs. However, many developed drugs resulted in adverse side effects for patients. The number of approved cardiovascular drugs decreased each year. According to reports, the budget requirement for a new developing drug is about $1.2 billion U.S. dollars. Despite an intensive, long, and expensive preclinical research period, drug candidates fail in clinical trials. The main reasons are known as clinical safety (toxicity) and efficacy, which lead to about 30% of drug project failures. [46] Cardiotoxicity-based failure of the drug is not only seen during drug development but also after being approved by the Food and Drug Administration (FDA). The success rate of clinical trials was about 20% between 1991 and 2000. Moreover, since 1997, the withdrawal rate of drugs on the market increased to 33.3% from 5.1% due to cardiotoxicity. [47] The main reason for the failure of cardiovascular drugs was adverse side effects such as arrhythmia. Drugs were withdrawn due to arrhythmia, which had different medical purposes such as antibacterial, antidiabetic, antihistaminic, and antiarrhythmic purposes between 1990–2010. [47]

Moreover, chemotherapic agents are one of the main reasons for cardiotoxicity such as DOX, daunorubicin or fluorouracil which lead to cardiotoxicity in >20% of patients treated with them. [48] Cardiac cells are more sensitive to the long-term effects of

drugs used for cancer treatment. DOX is one of the most efficacious anti-cancer anthracycline antibiotics that has been used against numerous types of cancer such as solid malignancies and hematologic neoplasia. [49–51] In DOX-induced cardiotoxicity, oxidative stress occurs due to the accumulation of DOX in mitochondria, which is the main affected organelle. DOX-induced cardiotoxicity is mainly caused by reactive oxygen species (ROS) generation. Apoptosis is another response of DOX-induced cardiotoxicity, which is probably related to cardiomyocyte death; however, the exact mechanism is still unclear. [52,53]

1.5. Conventional Drug Discovery and Development Process

The drug discovery and development process involves preclinical and clinical phases, as seen in Figure 1.3. [54] Firstly, the candidate drug is examined on non-human targets, which are cells and animal models. These studies aim to obtain preliminary result about drug toxicity, efficacy, and pharmacokinetics. If the preclinical phase result of the drug candidate shows very limited toxicity, it must be confirmed by the ethics committee to continue testing the drug in the clinical phase. In phase I, a small group of healthy volunteers are used to assess the safety of the drug and its dose. Many drugs fail at this phase. If it is successful, the drug moves to phase II, which is comprised of tests on a bigger group of volunteers to evaluate the efficacy of the drug. Finally, if the results are successful, the drug is tested on patients to evaluate the therapeutic effect of the drug at Phase III. If the results are obtained as predicted, the drug is put on the market. But, if the drug fails at phase I, the reasons are probably related to 2D culture and animal models. [46,55] Since these models are insufficient for evaluating the drug efficiency and toxicity that leads to failure of the drug in the clinical phase or after approval of the drug by the FDA, [56] adverse side effects should be predicted in the preclinical phase of drug discovery and development. For that reason, principal motto of numerous pharmaceutical companies is the ‘‘fail early, fail cheap’’. [57]

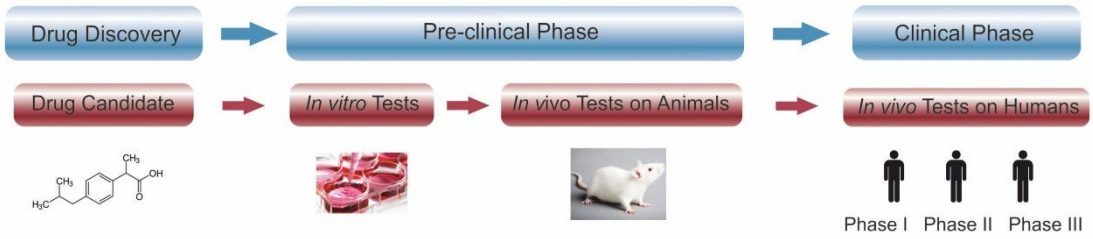

Figure 1. 3. Schematic of conventional drug discovery and development phases. [54]

The studies show that in 2D cell culture conditions, cell behaviour is not similar compared with human tissues/organs in terms of morphology, extracellular matrix interaction, cell-cell interactions, and receptor expression. For that reason, it is not possible to represent drug metabolism *in vivo.* [58,59] Animal models are used in *in vivo* studies to test drug efficacy, yet this also has varied drawbacks such as ethical issues, the necessity of a high budget for experiments, and the need for a long time period to get the result. Furthermore, using animal models does not necessarily result in the same response as the human body's response since chemical compounds are generally metabolized specifically for every species. [60,61] However, three-dimensional cell culture models have been a promising method of overcoming the problems in the traditional methods of the preclinical phase for screening drugs. The studies show that the cells in 2D and 3D cell cultures give different responses in terms of growth, proliferation, migration and invasion, morphology, and drug sensitivity, and that responses in 3D cell culture are more alike cells in *in vivo* conditions. [62–65] Moreover, the 3D cell culture offers spatial cell-cell interactions and cell–ECM interactions, and it is possible to co-culture various types of cells to create more realistic tissue and organ structures. [66,67] Therefore, 3D cell culture is a promising approach to overcoming the problems of conventional methods in the preclinical phase of drug screening and development.

1.6 *In vitro 3D* Cell Culture Models for Drug Development and Screening

3D cell culture models are classified into three subgroups that are known as scaffold-based, scaffold-free, and specialized platforms. [68] Scaffold-based 3D cell culture models provide physical support as an ECM-like structure where cells can aggregate, proliferate, and migrate. There are various parameters to consider when

designing a scaffold such as biocompatibility, bioactivity, biodegradability, etc. For this aim, scaffolds can be fabricated from biological (collagen, matrigel, alginate) or synthetic origin (polyethylene glycol (PEG), polylactic acid (PA), polyglycolic acid (PGA)) materials to obtain suitable properties such as stiffness, surface charge, wettability, and topography. [68,69] However, scaffold-based methods have various limitations such as reproducibility, sensitivity, compatibility, and the ability to scale up or down. In addition to this, scaffolds include too many constituents to fabricate that are complex, laborious, and expensive. [70,71] On the contrary, scaffold-free 3D culture methods are working based on the self-aggregation of cells which are mostly forminga spheroid. Spheroids are one of the well-characterized scaffold-free approach studies because it is possible to fabricate and reproduce them by using simple methods compared to scaffold-based methods. [59,72–76] There are various traditional methods to form spheroids that are hanging drop, low attachment plate, spinner flask, and magnetic levitation. Low attachment plates and spinner flasks are simple methods and they allow mass production. However, it is not possible to control cell number and spheroid size/shape. [77,78] The hanging drop method has been used to form a uniform-sized spheroid with a controllable and easy methodology, but it has important drawbacks. First, spheroid formation occurs in very low-volume media, and it is not possible to change the medium, which results in a limitation of spheroid growth. Second, the mass production of a spheroid is laborious. [79]

The last category for 3D cell culture formation is comprised of patterning and manipulation techniques. Micropatterned plates can be produced by microfabrication technology to create imprinted micropatterns on the surface of plates. These plates can create both scaffold-based 3D models and scaffold-free models. [68] Cell patterning and manipulation techniques have been used to create 3D cell culture models for various tissue engineering applications such as drug screening studies, [80–82] stem cell differentiation, [83–85] and regenerative medicine. [86,87] There are various cell patterning and manipulation techniques for fabricating 3D cellular structures that are mainly used such as lithography,[88,89] soft lithography techniques, [89,90] inkjet cell printing, [91] acoustic force manipulation,[92,93] and magnetic cell manipulation. [94–97] Lithographic techniques [98,99] and soft lithographic techniques [100,101] are known as conventional methods and use an elastomeric stamp to obtain a nano/micro-scale pattern. These techniques mostly require a high budget due to the need for cleanroom facilities and special equipment for

cell patterning. [84,102] In the ink-jet cell printing technique, patterned cells are obtained via a computer-aided model, which does not require a mask and thus saves time when fabricating patterned cell structures. In general, this technique can be adaptable, and it has a moderate cost compared to conventional methods. [103,104] However, parameters of formed droplets should be considered during the patterning of cells using this technique because its viscosity, elasticity, and surface tension can be a limitation for its application and the cell viability. Also, it needs an external power source, which is another limitation of this technique. [105,106] The acoustic force manipulation technique accomplishes patterned 3D self-assembly structures in a rapid way and high cell viability via a piezoelectric platform. [107,108] However, this technique requires a specialized set-up for cell manipulation and patterning that includes electrode fabrication, a piezoelectric surface, and an external power source. [105]

1.6.1. Magnetic Manipulation-based 3D Cell Culture Models

Magnetic manipulation-based techniques are promising approaches to fabricate 3D cell culture models. It can be classified as magnetic nanoparticle-based [86,94,95,109–111] and paramagnetic agent-based [76,112–118] manipulations.

In the magnetic nanoparticle-based magnetic manipulation technique, magnetic nanoparticles (MNPs) are targeted to accumulate in cells via electrostatic interaction between the cell membrane and MNPs. After that, cell patterning is accomplished by an external magnetic force. [86,94] Recently, a new biopatterning technique was introduced by Souza et. al (2013), which provides a different point of view for drug screening studies. In their first paper, human embryonic kidney cells (HEK293) and tracheal smooth muscle cells (SMCs) were incubated with MNPs which are non-specifically and electrostatically bound to cells. Then, cells were patterned on the plate surface while applying an external magnetic field that formed a 3D ring structure and was tested with ibuprofen and sodium dodecyl sulfate (SDS). The ring-closing rate was an important parameter for toxicity evaluation and the dose-dependent response obtained compared to 2D control. [110] The method was also applied to vascular smooth muscle cells to represent blood vessel segments. The aim of this study was to validate ring contraction as a measure of vasoactivity therefore the varied concentration of blebbistatin was applied as vasodilators. Blebbistatin had a dilatory effect on ring contraction, and higher

concentrations resulted in reduced contractions. The advantage of this assay was the ability to perform high throughput screening using the ring structure without using animals as cell sources. In this way, this technique will aim to reduce the usage of animal models. [111]

MNP manipulation-based technique which is called magnetic levitation (MagLev) has been also used for fabrication of spheroids. In this technique, cells are incubated with magnetic iron oxide-containing hydrogels and magnetic nanoparticles taken by cells or remain membrane-bound. Cells are accumulated on an air/liquid interface with the help of externally applied magnetic field on top of the well plate. After a certain time, cell-cell aggregation turns into a spheroid which was introduced by Souza et al. (2010). Human glioblastoma cells were turn into spheroids in 24 hr culture time. It was also indicated that control of 3D structure is possible by using this technique. [119] Also, same technique was used to fabricate 3D cellular structures using varied cell lines; HEK293, human tracheal smooth muscle cells, human pulmonary fibroblasts, human glioblastoma, H-4-II-E, MDA-231, human umbilical vein endothelial cells (HUVECs), MCF-10A, LNCaP, HepG2, A549 and 3T3-L1. Interestingly, cell lines behaviour was varied in terms of their size and morphology; 3T3-L1 cells formed small and dense clusters, while A549 cells formed less-dense and sparse structures. [120] In another study, 3D co-culture model was obtained using four human cell types in the bronchiole; endothelial cells, smooth muscle cells (SMCs), fibroblasts, and epithelial cells (EpiCs). These cell layers were first cultured in 3D by MagLev, and then manipulated into contact with a custom-made magnetic pen. It was reported that MagLev is capable of creating layered and organized co-cultures. [121]

MagLev can also accomplish the formation of spheroids and 3D cellular structures by using paramagnetic agents instead of MNPs. [76,112–114,122] The principle of this technique relies on the levitation of cells in paramagnetic fluid, which is obtained using Gd^{3+} ion salts under a magnetic field gradient which is provided by two magnets, where the same poles are facing each other in an anti-Helmholtz coil configuration. At the equilibrium height, buoyancy forces are balanced by the magnetic and gravitational forces while cells move from a location with a larger magnetic field strength to a location with a lower magnetic field strength, as shown in Figure 1.4. After that, accumulated cells at a certain levitation height increase cell-cell interaction, which leads to cellular aggregate and spheroid formation. [76,116] In this scaffold-free technique, cells can create their own ECM microenvironment. Recently, cell spheroids and cell

strings were reported by Turker et al. (2018) based on MagLev technique. It was indicated that the structure and dimension of the cellular assembly can be tuned by initial cell number. Also, cell high cell viability was observed in both NIH/3T3 cell spheroids and cell strings. [76] MagLev technique was also used for tissue construct bioassembly by Perfenov et al. (2018). For this aim, a new set-up was developed that contain two annular neodymium magnets, placed with the same poles face to each other and glass cuvette placed in the axial hole of the magnets. Tissue spheroids were obtained using ultra-low adhesion spheroid microplates. Those chondrospheres were assembled into 3D tissue construct rapidly in the permanent magnetic field in the presence of gadolinium. [114]

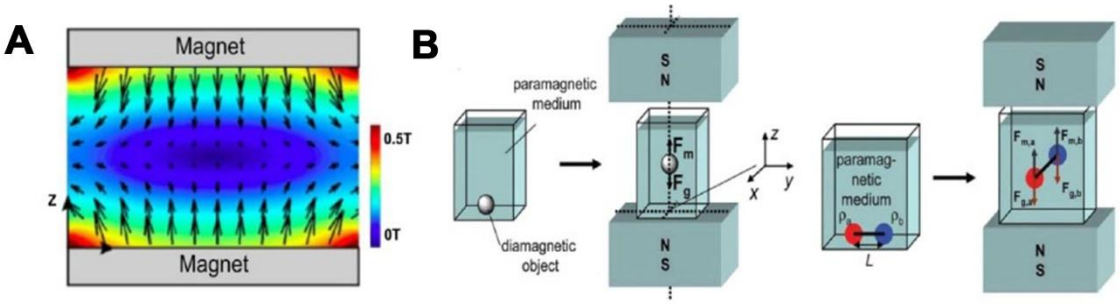

Figure 1.4. A) 3D magnetic field simulation in the X−Z plane, B) Schematic representation of basic MagLev setup showing the magnetic ($F^{\rightarrow}m$) and gravitational forces ($F^{\rightarrow}g$) that levitate the object [115].

CHAPTER 2

MATERIALS AND METHODS

2.1. Fabrication of MagLev Set-up

To investigate the levitation behaviour of cells, and formation of 3D spheroids and cellular structures, 40×5 mm and 30×15 mm N35 Neodymium (NdFeB) magnets (Mıknatıs Teknik Company) were used. The magnetic field strength of magnets was measured as 0.15 and 0.4 T for 40×5 mm and 30×15 mm magnets respectively, by using a GM07&GM08 Gaussmeter (Hirst Magnetic Instruments Ltd.). As shown in Figure 2.1, each pair of magnets was inserted into polymethyl methacrylate (PMMA) holders in an anti-Helmholtz configuration and fixed with screws. The MagLev setups were sterilized both with 70% ethanol and UV prior to 3D cell culture studies. A petri dish (Ibidi- 80131, 800 µl) consists of cells, a complete cell medium, and a paramagnetic agent Gx (Gadobutrol/Gadovist, Bayer) was placed within the setup among the magnets for cell culture experiments.

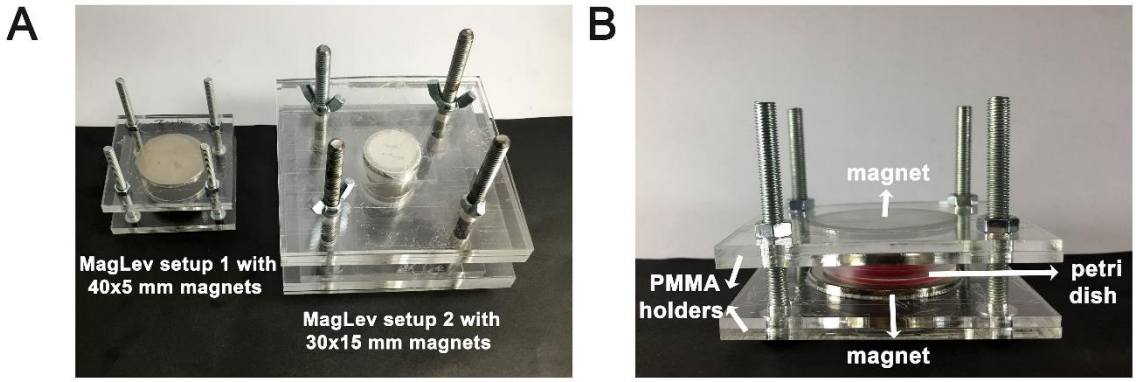

Figure 2.1. MagLev set-ups with dimensions of 40×5 mm and 30×15 mm magnets for 3D cellular structure formation. A) Top view, and B) Side view of MagLev set-up.

2.2. Fabrication of Biopatterning Set-up

For the biopatterning study, a polymethylmethacrylate (PMMA) holder was used to secure disc magnets (N35) with the dimensions of 7×18 mm, and all magnets were assembled as shown in Figure 2.2. Neodymium disc magnets and rectangular magnets (N35) with the dimensions of 7×18 mm and 15×10 mm respectively were purchased from Mıknatıs Teknik Co. (Turkey), and a ring magnet (N52) with a dimension of 6.5×32 mm was purchased from K&J magnetics (USA).

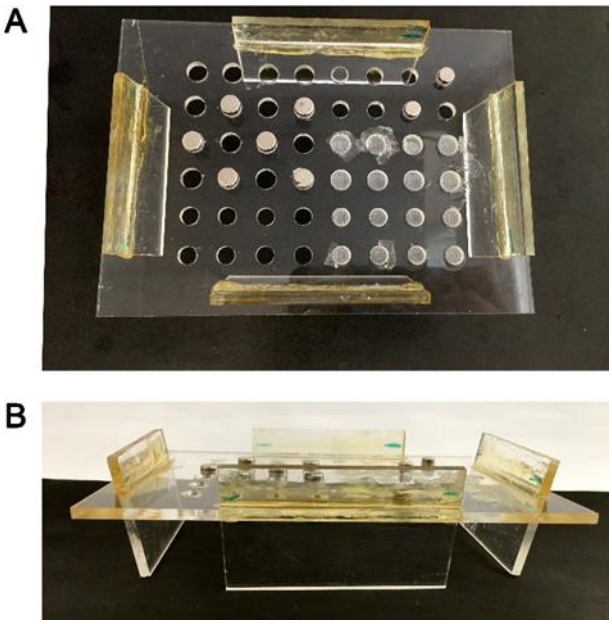

Figure 2. 2. PMMA holder for magnets. A) Top view, B) Side view.

2.3. Cell Culture

NIH/3T3 (mouse fibroblast cells, ATCC CRL-1658), MCF7 (human epithelial breast adenocarcinoma, ATCC HTB-22), MDA-MB-231 (human epithelial breast adenocarcinoma, ATCC HTB-26), HeLa (human epithelial cervix adenocarcinoma, ATCC CCL-2), SH-SY5Y (human bone-marrow neuroblastoma, ATCC CRL-2266), PC-12 (rat adrenal gland pheochromocytoma, ATCC CRL-1721), MDA-MB-231 dsRED and MDA-MB-231 GFP cells were cultured in high glucose DMEM (GIBCO, Thermo Fischer Scientific) containing L-glutamine and supplemented with 10% Fetal Bovine Serum (FBS) (GIBCO, Thermo Fischer Scientific) and 1%

penicillin/streptomycin (GIBCO, Thermo Fischer Scientific). The cells were cultured up to ~ 90% confluency in a humidified environment (5% CO_2, 37 °C). The harvested NIH/3T3 cells were used further for optimization steps of biopatterning and MagLev studies. After optimization, MCF7, MDA-MB-231, HeLa, SH-SY5Y, PC-12, MDA-MB-231 dsRED and MDA-MB-231 GFP cells were used to fabricate tumoroid and co-culture models for further studies.

H9c2(2-1) (ATCC CRL-1446) rat cardiomyocyte cells were cultured in high glucose DMEM (Biological industries, 01-052-1A) containing L-glutamine and supplemented with 1% penicillin/streptomycin (GIBCO, Thermo Fischer Scientific), Na-pyruvate (Biological industries, 03-042-1B), and 10% FBS(Biological industries, 04-127-1A). The cells were cultured up to ~ 80% confluency in a humidified environment (5% CO_2, 37 °C) and then cells were used for furtherstudies.

The hiPSC-CMs (WTC cardiomyocytes, GM25256) and cardiac fibroblast cells (cFBs DRRAGN 3A1) were frozen after differentiation for long-term storage in liquid nitrogen. The cells were thawed, counted and resuspended with a high glucose cardiomyocyte maturation TDI medium and then used for further studies.

2.4. Biofabrication of 3D Spheroids

In this study, 3D spheroids were fabricated using MagLev technique. [76] For this aim MagLev set-up was used as shown in Figure 2.1. 3D cell culture parameters were optimized for MagLev methodology by using NIH/3T3 fibroblast cells as a model cell line. First, initial cell number and spheroid size relation was investigated for the developed MagLev setup which has high working volume (800 µl). Varied cell numbers; 2.5/5/10/25/50/100×10^3 at a 10 mM Gx (Gadobutrol) concentration and 0.15 T magnetic field were used. After that, the toxicity of Gx were analysed for 10/30/50/100 mM Gx at 0.15 T. As a final step, spheroids were cultured for 1/3/5/7 days at 2.5×10^3 NIH/3T3, 30 mM Gx, and 0.15 T to determine long-term cell viability and the morphological changes. Cell viability (%), spheroid area and circularity analyses were accomplished by ImageJ software (NIH).

Further applicability of the MagLev platform was investigated for 3D tumor and co-culture formation. To fabricate 3D tumour models, various cancer cell lines were utilized such as MCF7, MDA-MB-231, HeLa, SH-SY5Y, PC-12. For this aim, cell number and Gx concentration were kept at 10×10^3, and 10 mM respectively. On the

other hand, the magnetic field was applied 0.4 T (30×15mm magnet) for MDA-MB-231 and HeLa cell lines to decrease incubation time and obtain 3D cellular structures while it was 0.15 T (40×5mm magnet) for MCF7, SH-SY5Y, and PC-12 cell lines. Moreover, to fabricate a 3D co-culture model 10×10^3 MDA-MB-231 dsRED and MDA-MB-231 GFP cell lines were cultured at 50 and 100 mM Gx and 0.4 T.

The relation of initial cell number and spheroid size were examined first for biofabrication of 3D cardiac spheroids where culture parameters for various cell numbers; $2.5/5/10/25/50/100\times10^3$ were investigated at a 10 mM Gx, 0.15 T magnetic field and 24 hr culturing time. After that, the toxicity of Gx were analysed for 10/30/50/100 mM Gx at 0.15 T. 2.5×10^3 H9c2 cells were cultured for 1/2/3/4/5 days at 10 mM Gx and 0.15 T to determine long-term cell viability and the structural features of spheroids. Cell viability (%), spheroid area and circularity analyses were accomplished by ImageJ software (NIH).

2.5. Biofabrication of Biopatterned 3D Cellular Structures

The schematic of developed biopatterning methodology is shown in Figure 2.3. Bio-ink, which consists of either NIH/3T3 or H9c2 cells, MNPs, and alginate was prepared to pattern cells in the shape of the magnet. Firstly, a well plate (tissue culture treated, Thermo Scientific) was placed onto the PMMA magnet holder. Bio-ink was added into a well that contains $CaCl_2$ solution for crosslinking of alginate (Figure 2.3A). After gelation was completed $CaCl_2$ solution was replaced with cell culture medium (Figure 2.3Bb) and cells were patterned in the shape of the magnet. Later, citrate buffer was applied 3 times for 15 min to disassociate alginate and to remove MNPs (Figure 2.3C). Borders and center of patterned structure was monitored by light microscopy to evaluate the patterning efficiency and cell adhesion before and after disassociation steps.

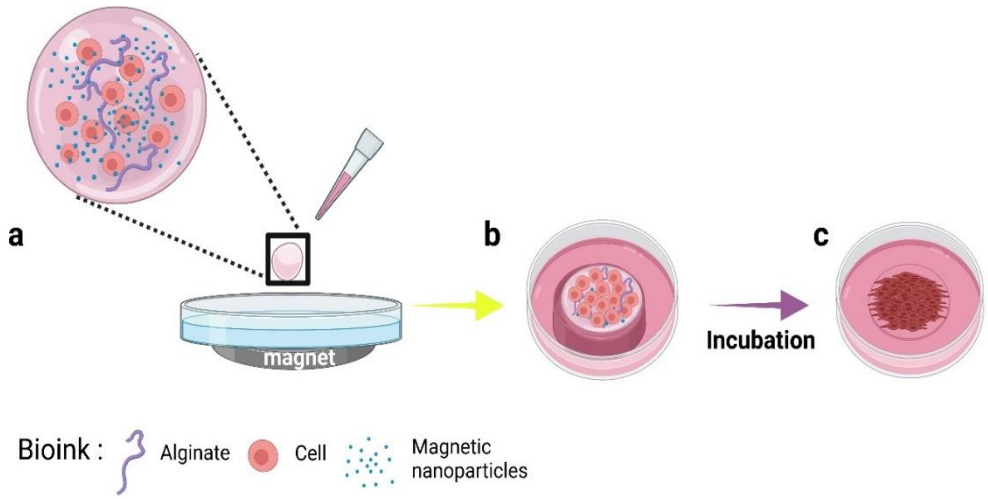

Figure 2.3. Schematic of developed biopatterning methodology. A) Bio-ink is patterned as a disc shape and crosslinked with $CaCl_2$ solution B) $CaCl_2$ solution is replaced with cell culture medium C) Patterned 3D cellular structures are obtained after disassociation of alginate (The illustration was created with BioRender.com).

Na alginate (Sigma Aldrich, 71238) in varied concentrations; 0.05, 0.08, 0.09, 0.1 and 0.5 (w/v) % and $CaCl_2$ (Sigma Aldrich, C8106) in varied concentrations; 5, 7.5, 10, and 20 mM, and citrate buffer (100 mM) were prepared, and filter sterilized. Fe_3O_4 MNPs (1 mg/ml) were synthesized as described elsewhere [123]. Optimization studies were carried out by analyzing the concentration of alginate, MNP, $CaCl_2$; cell number; alginate and MNP volume; incubation time of $CaCl_2$ and bio-ink. Plackett-Burman design model, which is a classical method to screen a large number of variables, was used to distinguish critical parameters. [124,125] For this aim, a total of 12 runs were applied, which includes 8 parameters as effective factors in corresponding range given in Table 2.1. Here, the response value is given as the efficiency of cell patterning and surface coverage. Further, the Box-Behnken design was applied to form an experimental model while using distinguished critical parameters to determine optimum values. [126] In this model, 16 runs were evaluated for a 3-level factorial design with 4 replicates on the center point. Design-Expert 7.0.0 (2005, Stat-Ease, Inc.) was used to generate experimental runs for both Plackett-Burman design and Box-Behnken design models. Each run was evaluated based on patterning efficiency and patterned structures, and then each response was scored between 0-100 after the dissociation step. A mathematical model of patterned cells was obtained according to the experiment results. ANOVA was used to evaluate the models.

Table 2. 1. Experimental parameters that were used in the Plackett-Burman design

Parameters	**unit**	**low**	**high**
Alginate concentration	w/v %	0.08	0.5
Fe_3O_4 concentration	µg/ml	400	800
Cell number		5×10^5	1×10^6
Alginate volume	µl	4	6
Fe_3O_4 volume	µl	2	6
$CaCl_2$ concentration	mM	5	20
$CaCl_2$ incubation time	min	3	5
Bio-ink incubation time	h	4	5

To examine the patterning capability of bio-ink and the formation of sharp structures such as corners and linear patterns, ring and rectangular magnets were used. In these experiments, the formulation of bio-ink was modified to pattern bio-ink and fabricate 3D cellular structures. For this aim, the MNP concentration was increased to 800 µg/ml from 600 µg/ml, while other parameters were kept constant. The total bio-ink volume was applied as 10 and 20 µl for the ring and rectangular magnets respectively.

Prior to hiPSC-CMs seeding, well surfaces were coated with Matrigel (1:100, Corning) and geltrex (1:100) in DMEM/F12 (DMEMF12 1:1 (1x) + GlutaMAX-I, Gibco). Coating solution was added to wells and incubated for 90 min at 37 °C. After aspiration of the coating solution, DMEM/F12 with 10% Fetal Bovine Serum (FBS, Gibco) was added to wells and incubated overnight. The hiPSC-CMs (WTC cardiomyocytes) and cardiac fibroblast cells (cFBs DRRAGN 3A1) were thawed and the cell suspension was filtered using a polystyrene tube with a cell strainer cap (pore size: 35 µm, Corning). The cells were counted and resuspended with a high glucose cardiomyocyte maturation TDI medium. To fabricate ring shape patterned cardiac structure, total bio-ink volume was kept as 30 µl for the N52 ring magnet (9.5×3.2 mm). Bio-ink components which are cell number, alginate and MNP concentrations were applied as 4×10^5 - 8×10^5 (in 12 µl culture medium), 0.08 % (in 12 µl) and 800 µg/ml (in 6 µl) respectively.

2.6. Cell Viability Analysis

To examine the cytotoxic response of paramagnetic agents on H9c2 cells, the Live/Dead and Alamar Blue assays were performed. For this aim, 5000 H9c2 cells were cultured in 2D with commercial paramagnetic agents such as gadobutrol (Gadovist, Bayer), gadoteric acid (Dotarem, Guerbet), and gadodiamid (Omniscan, GE) in varied concentrations (10/30/50/100 mM) for days 1/3/5/7. [76]

For the Live/Dead assay, cells were stained with CytoCalcein™ Green and Propidium Iodide (PI) dyes (AAT Bioquest) which were added into the assay buffer solution in equal proportions and incubated at 37 °C for 30 min. Then, viability analysis was carried out using a fluorescence microscope (Zeiss Axio Observer).

For the Alamar Blue (Chem Cruz) assays, a 0.01% resazurin sodium salt reagent was used and cells were incubated in it for 4 hrs. Measurements were performed by the Multiskan™ GO Microplate Spectrophotometer (Thermo Fischer Scientific) at 570–600 nm.

For MTT analysis, the reagent was added (final concentration was 0.5 mg ml^{-1}) to wells and incubated for 4 hr for both 2D control and 3D cellular structures. After that, formazan crystals were solubilized by using DMSO, and measurements were performed by a Multiskan™ GO Microplate Spectrophotometer (Thermo Fischer Scientific) at 565-650 nm.

2.7. Immunostaining of 3D Cellular Structures

The cellular and extracellular matrix (ECM) components of the 3D spheroids and biopatterned 3D cellular structures using either NIH/3T3 or H9c2 cells were characterized in terms of nucleus, cytoskeleton, and collagen staining for short-term and long-term. Fixation of 3D spheroids and biopatterned 3D cellular structures were performed with 4% paraformaldehyde for 20 min. Permeabilization and blocking were applied as 0.1% Triton X-100 in PBS for 5 min, and 1% BSA in PBS for 30 min respectively. For F-Actin labeling, TRITC-conjugated Phalloidin (Sigma-Aldrich) was applied for 60 min at room temperature (RT). After incubation, rinsing was done three times for 10 min. To label collagen I of the extracellular matrix, anti-collagen Type I-

FITC (Sigma-Aldrich) was applied for 50 min at RT. After the washing step, DAPI AAT BIOQUEST) solution was applied for 5 min and rinsed with wash buffer three times for 5 min.

Also specific cardiac markers; cardiac troponin T and MYH6 were investigated for short- and long-term. Fixation (4% paraformaldehyde), permeabilization (0.1% Triton X-100 in PBS), and blocking (1% BSA, 10% FBS in PBS) steps were applied, as stated above. The primary antibody of MYH6 (Abclonal) and cardiac Troponin T (Bioss) was applied and incubated overnight at +4 ℃. After the rinsing step, rhodamine (TRITC) conjugated anti-rabbit secondary antibody (Abclonal) was added and incubated for 60 min. DAPI (Sigma-Aldrich) solution was applied for 5 min. Rinsing was done three times for 5 min and stained spheroids and 3D cardiac cellular structures were analysed under a fluorescence microscope (Zeiss Observer Z1).

To characterize and investigate cellular and extracellular components of the biopatterned cardiac structures using co-cultured hiPSC derived cardiomyocytes and cardiac fibroblast cells; α-actinin, collagen I, Cx-43, Troponin T, and DAPI staining was done at day 13. Patterned structures were fixed with 4% paraformaldehyde for 20 min, permeabilized with 0.1% Triton X-100 (Sigma-Aldrich) in PBS for 8 min, then blocked with 2 % BSA and 5 % goat serum in DPBS for 60 min. Primary antibodies of α-actinin (Sigma), collagen I (Sigma), Cx-43 (Sigma), and Troponin T (Sigma) were applied and incubated overnight at +4 ℃. Secondary antibodies of Goat-anti-Mouse Alexa Fluor 647 (Invitrogen) and Goat-anti-Rabbit (Invitrogen) 488 were prepared in a blocking solution and incubated for 90 min at RT. After rinsing, DAPI (Sigma-Aldrich) solution was applied for 5 min. After staining, patterned structures were visualized under Zeiss FSM 880 confocal microscope.

2.8. Doxorubicin-Induced Cardiotoxicity Study

To investigate DOX-induced cardiotoxicity, 1, 5, 10, 25, 50 µM DOX (HY-15142-100, Doxorubicin hydrochloride, MEDCHEM) was separately applied to both 2D (5000 cells/well) and 3D cell culture (2.5×10^3 cells for 3D cardiac spheroids and 4×10^5 cells for biopatterned 3D cardiac structures) using H9c2 cells. DOX toxicity was investigated via a MTT (Sigma, Aldrich) assay. MTT analysis was done while adding the reagent (final concentration was 0.5 mg ml^{-1}) to wells and incubated for 4 hr for

both 2D control and 3D cardiac spheroids and patterned 3D cellular structures. For 3D cardiac cellular structures fabricated via the biopatterning method, DOX was applied after 48 hr cultured patterned 3D cardiac structures. After that, formazan crystals were solubilized by using DMSO, and measurements were done by a Multiskan™ GO Microplate Spectrophotometer (Thermo Fischer Scientific) at 565–650 nm. For 3D cardiac spheroids that were fabricated by MagLev, DOX was applied to 24h cultured 3D cardiac spheroids. The cell viability of 3D cardiac spheroids was analysed based on formazan intensity by using ImageJ software. For this analysis, similar sizes of spheroids were utilized, and relative dose-response values were calculated. IC_{50} values were obtained by using GraphPad Prism 8 software.

2.9. Statistical Analysis

All data are expressed as the standard error of the mean (±SEM). Statistical analysis for the dose-response of the 3D cardiac models and 2D control was performed using an unpaired two-tailed t-test by using GraphPad Prism 8 software. A $p < 0.05$ was considered as statistically significant.

CHAPTER 3

RESULTS AND DISCUSSION

3.1. Biofabrication of 3D Cell Culture Models via the Magnetic Levitation Methodology

3.1.1. Biofabrication of 3D Spheroids Using NIH/3T3 Cells

When MagLev technique is used cells are magnetically guided towards a lower magnetic field area from a higher magnetic field area in the presence of paramagnetic agent. Under these conditions, buoyancy forces are equalized by magnetic and gravitational forces [76,116] and cellular clusters start to form at the centre of the petri dish or any container that is associated with MagLev setup. Magnetically guided and accumulated cells form 3D cellular structures and spheroids due to increased cell-cell interactions at a certain levitation height, as shown in Figure 3.1.

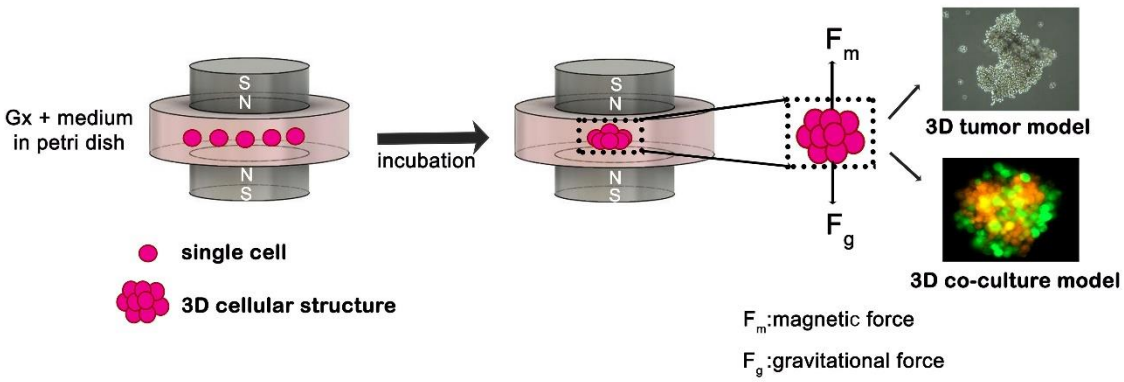

Figure 3. 1.Schematic illustration of developed MagLev methodology.

MagLev set-ups that are shown in Fig. 2.1 were used to biofabricate 3D spheroids and cellular structures, and NIH/3T3 cell line used as a model to optimize the parameters. This newly designed setup configuration provides a way of tuning the size and other properties of 3D cellular structures. It *(i)* allows the easy and rapid fabrication of tunable 3D cellular structures at high volume and in a low magnetic field, *(ii)* provides easy imaging and analysis of spheroids in real-time, *(iii)* enables large scale production, and, moreover, *(iv)* its simplicity, low cost, and portability makes it a favorable platform for use in resource-limited settings.

At first, cellular assembly in 3D and spheroid formation via MagLev screened in real-time for NIH/3T3 cells at 0, 2, 3, 5, 8, 12, 22, and 24 hr by light microscopy as given in Fig. 3.2. Light microscopy images were taken directly from the top of the petri dish. At 0 hr, cells were suspended by magnetic forces at a certain levitation height, and at 2 hr, cells started to accumulate at the centre. Cellular aggregation was observed at around 5 hr, and cellular aggregates were assembled to form larger 3D structures at 8 hr. After 12 hr culturing, loose cellular aggregates became denser and started to form more compact spheroid structures, where circular structures were obtained after 24 hr. [132]

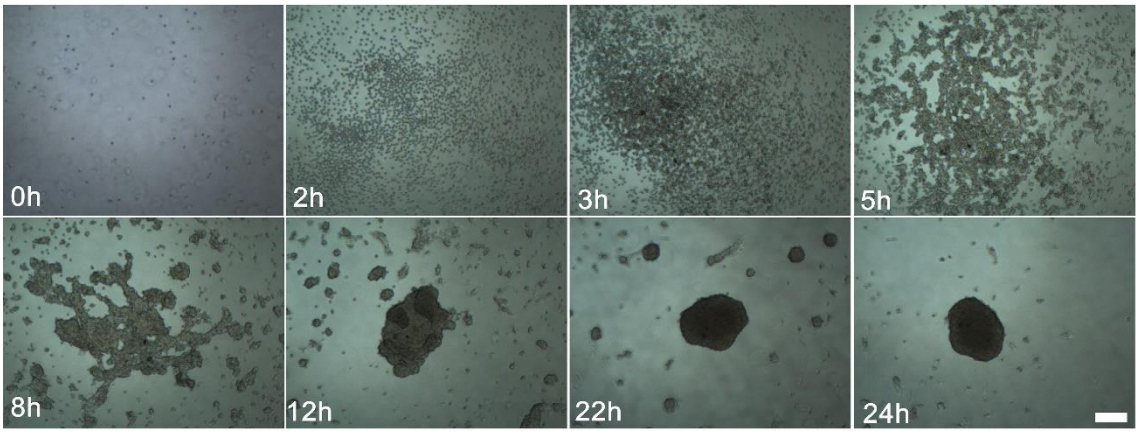

Figure 3. 2. Time-dependent light microscopy images of spheroid formation for NIH/3T3 cells using magnetic levitational assembly at 0, 2, 3, 5, 8, 12, 22, and 24 hr. Scale bar: 200 µm.

Circularity is another significant characteristic for 3D cellular structures, which represents the ideal circular structure of a spheroid when the value is close to 1 [127]. Circularity is described as the following:

$$\text{Circularity} = 4\pi(\text{area}/\text{perimeter}^2)$$

As given in Figure 3.3., the circularity of spheroids was calculated as 0.76, 0.85, and 0.89 at the 12, 22, and 24 hr culturing times respectively. As a result, it was indicated that increased culture time improved circularity of spheroids.

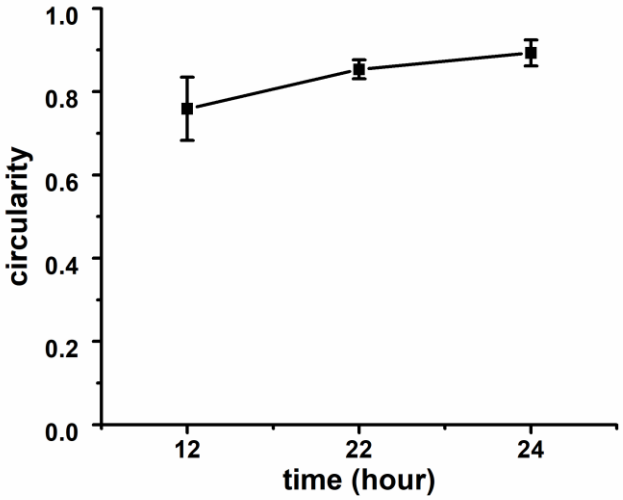

Figure 3. 3. Circularity versus time graph for 25×10^3 NIH/3T3 cells at 12, 22 and 24 hr.

3.1.2. Effect of Initial Cell Seeding Number

To investigate and then evaluate the effect of initial cell seeding number on spheroid size and area, varied cell numbers; 2.5, 5, 10, 25, 50, 100×10^3 were cultured in 3D at 10 mM Gx. As given in Figures 3.4 and 3.5, the low cell number (2.5, 5, 10×10^3) provided high cell viability that ranged between 50% to 100%, while the viability decreased below 50% with the high cell number (25, 50, 100×10^3). When high cell number is used low cell viability was observed due to the diffusion limitation. It is well-known fact that when the size of spheroid is above 200 µm the diffusion of O_2 and nutrients inside the spheroid is limited, and also insufficient mass transport results in the accumulation of metabolic waste. [128,129] It was obvious that spheroids obtained with low cell number overcame diffusion limitations and resulted in high cell viability. In addition to cell viability, spheroid area change was also analysed for varied cell numbers, where small spheroids were obtained with low cell number and bigger spheroids were obtained with high cell number as given in Figure 3.4. The area of spheroids was calculated as 0.26, 0.59, 2.22, 3.38, 4.94, and 21.2×10^4 µm^2, for 2.5, 5,

10, 25, 50, and 100×10^3 cell numbers, respectively. The size of a spheroid is one of the important parameters that affect the use of the spheroid in varied tissue engineering applications like drug screening. Results affirm that spheroid size and area can be tuned by changing the initial cell seeding number.

It is known that large spheroids have diffusional gradient zones: (i) an outer layer consisting of viable cells that can proliferate due to a well-oxygenated zone, and (ii) the inner layer, known as the necrotic core, which has hypoxic quiescent cells; when they cannot receive enough O_2, metabolites and waste accumulation occurs in the core. [130,131] These models are representative alternatives especially for 3D tumor models. [128,132] Here, these layers were observed in large spheroids as given in Figure 3.4.

Moreover, Figure 3.6 shows circularity values against initial cell seeding numbers. The circularity of spheroids in varied cell densities ranged between 0.69 and 0.86, while the maximum circularity was obtained for 25×10^3 NIH/3T3 cells; still, the high circularity value was obtained for all cell densities, showing that there is no correlation between cell seeding number and circularity.

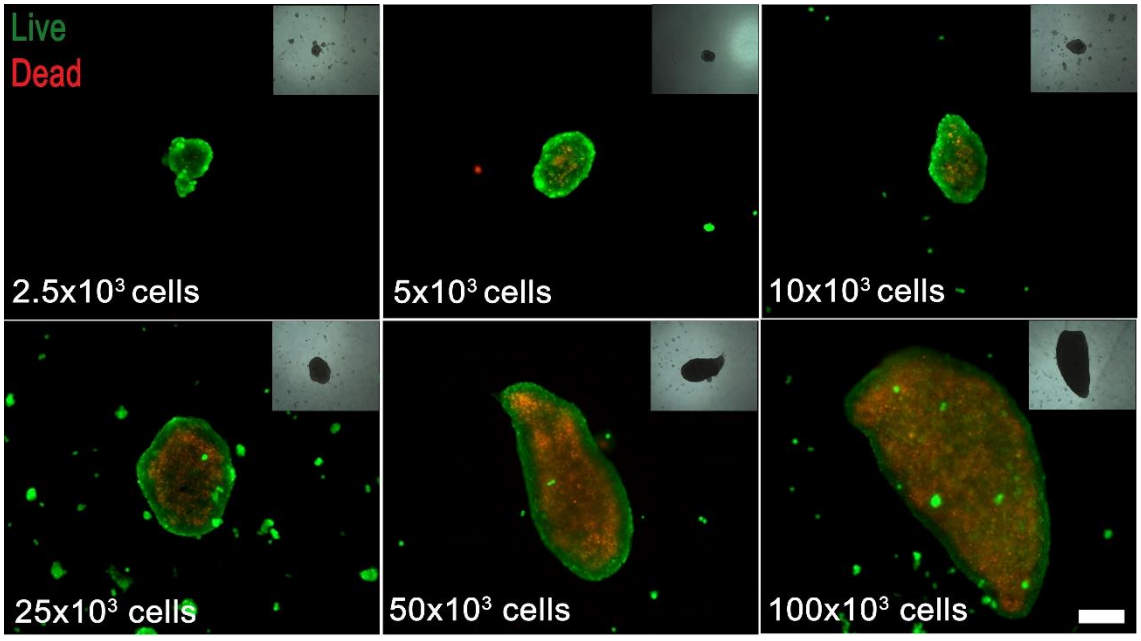

Figure 3.4. Cell viability images of NIH/3T3 spheroids at varied cell seeding numbers; 2.5, 5, 10, 25, 50, 100×10^3 (green: live cells, red: dead cells). Scale bar: 200 µm.

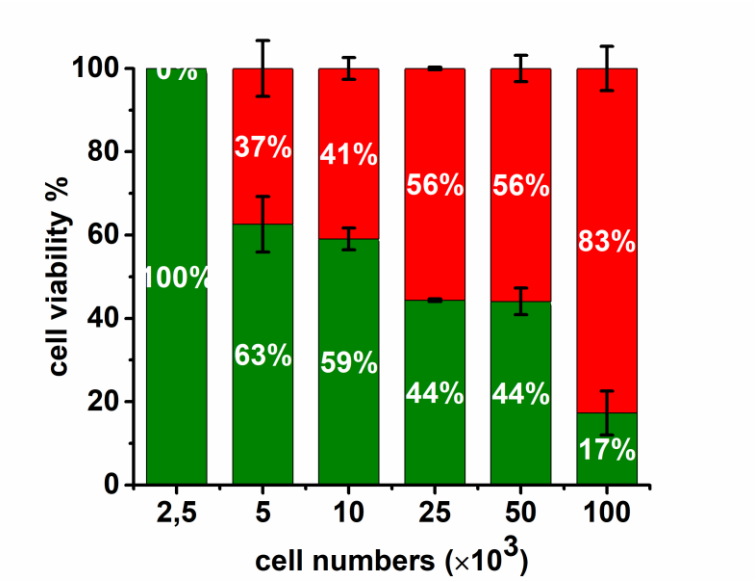

Figure 3.5. Cell viability values of NIH/3T3 spheroids at varied cell seeding numbers; 2.5, 5, 10, 25, 50, 100×10^3.

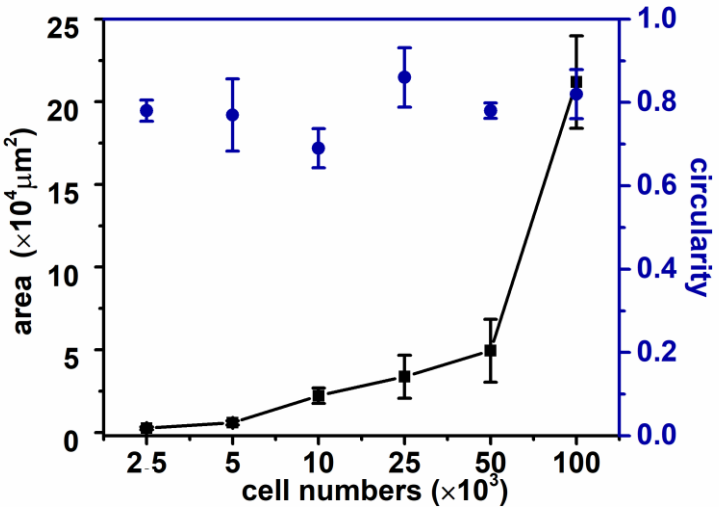

Figure 3.6. Representative spheroid area versus circularity at varied cell seeding numbers; 2.5, 5, 10, 25, 50, 100×10^3.

3.1.3. The Effect of the Paramagnetic Agent

Recently, various Gd^{3+} chelates and salts such as gadobutrol, gadoteric acid, and gadodiamide were utilized as a paramagnetic agents, and they were investigated in terms of cellular toxicity. The lowest toxicity on 2D cultured NIH/3T3 cells was obtained by gadobutrol (Gx) compared to other paramagnetic agents; [76] therefore, Gx was used as a paramagnetic agent in this study. 10, 30, 50, and 100 mM Gx were investigated in terms of levitation capability and cytotoxic effect on NIH/3T3 cells. However, the spheroid formation was not obtained for 2.5×10^3 cell number when 10 mM of Gx is used. The reason might be that 10 mM of Gx was not enough to gather cells and form spheroid at low cell number (2.5×10^3).

Also, the Live/Dead analysis was done and high cell viability was obtained for the spheroids formed with low cell number (2.5×10^3) that was cultured for 24 hr at 30, 50, 100 mM Gx, as shown in Figures 3.7 and 3.8. The diameters of spheroids were below 200 μm. These results support that diffusion limitation was overcome with low cell seeding number. Moreover, high Gx concentrations such as 50 and 100 mM did not affect the viability of spheroids, which is contrary to 2D standard cell culture results. [76] That result supports that when cells are cultured in 2D and 3D different responses are obtained with the same agents, since the 3D microenvironment provides better resistance against toxic substances. [133,134] It is worth mentioning that recently the influence of Gx on cell viability was also investigated in 3D spheroids, and it was reported that 50 mM Gx provides around 87% viability, which correlates well with our findings. [113,114]

Spheroids formed in varied Gx concentrations were also investigated in terms of spheroid area and circularity, as given in Figure 3.9. Increased Gx concentrations resulted in increased spheroid area; 2.6, 3.6, 6.8×10^3 μm^2 for 30, 50, 100 mM Gx respectively, as given in Figure 3.9. High paramagnetic agent concentrations provide better magnetization, therefore more cells were gathered and accumulated in the centre close to each other, which triggered the formation of bigger spheroids. Moreover, circularity was obtained as 0.714, 0.843, and 0.905 for 30, 50, and 100 mM Gx respectively (Figure 3.9). Those results affirm that high Gx concentration not only supports the formation of larger spheroids, but also improves the circularity of the spheroids. As a result, it was shown that both spheroid size and circularity could be also tuned by applying different Gx concentrations.

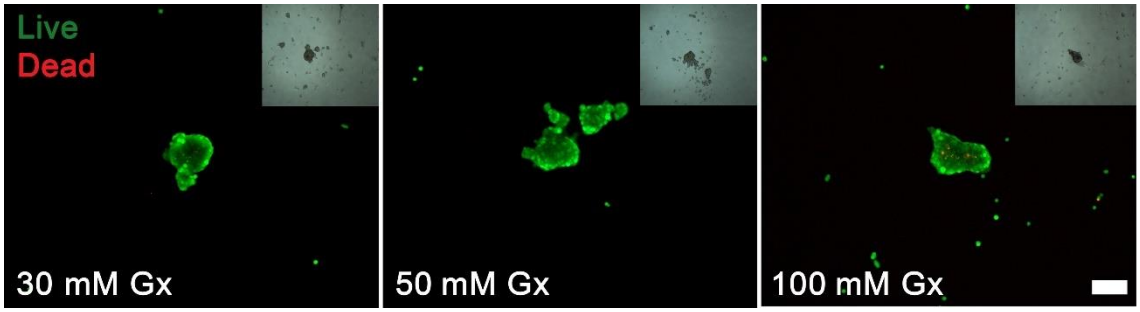

Figure 3.7. Cell viability images of NIH/3T3 spheroids at varied Gx concentrations; 30/50/100 mM for 2.5×10^3 cell seeding number. Scale bar: 200 µm.

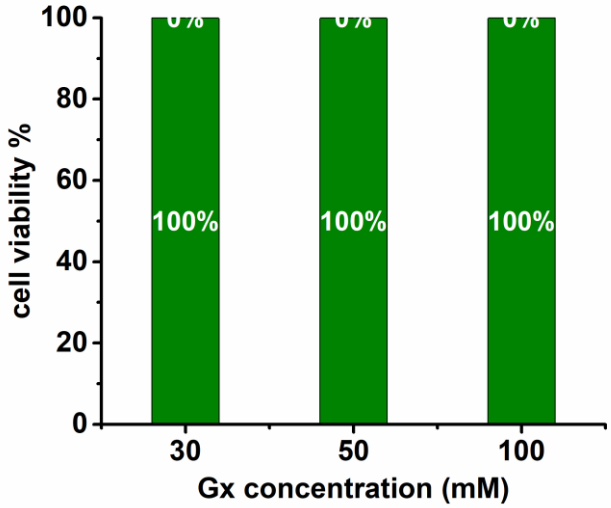

Figure 3.8. Cell viability values of NIH/3T3 spheroids at varied Gx concentrations; 30/50/100 mM for 2.5×10^3 cell seeding number.

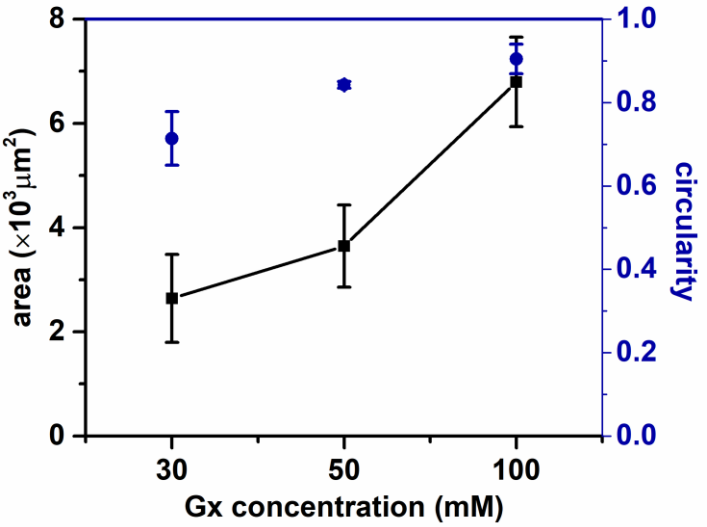

Figure 3.9. Representative spheroid area versus circularity at varied Gx concentrations; 30/50/100 mM.

3.1.4. The Effect of Culture Time

Culture time is another significant parameter that influences the cell viability, spheroid size, structure, and other properties. Here, cell viability and morphological changes of spheroids were evaluated with NIH/3T3 cells for 1/3/5/7 day culture times. Cell viability decreased with increased culture time, while necrotic core formation was observed starting from day 3 as given in Figures 3.10 and 3.11. On day 3, the diameter of the spheroid reached to 200 µm and cell viability was observed as 92%.Moreover, on day 5 and day 7 cell viability decreased to 81% and 58% respectively due to diffusion limitation. As explained previously, diffusion limitation occurs if the spheroid diameter is above 200 µm, and results in low cell viability. As shown in Figure 3.10 and 3.12, with increased culturing time, bigger spheroids and larger spheroid area were obtained. The spheroid areas were obtained as 2.6, 6.2, 10.9, and 14.2×10^3 μm^2 for day 1, 3, 5, and 7 respectively. Calculated circularity values (Figure 3.12) ranging between 0.78 and 0.9 affirmed that the spheroid structure was maintained for long culture times as well.

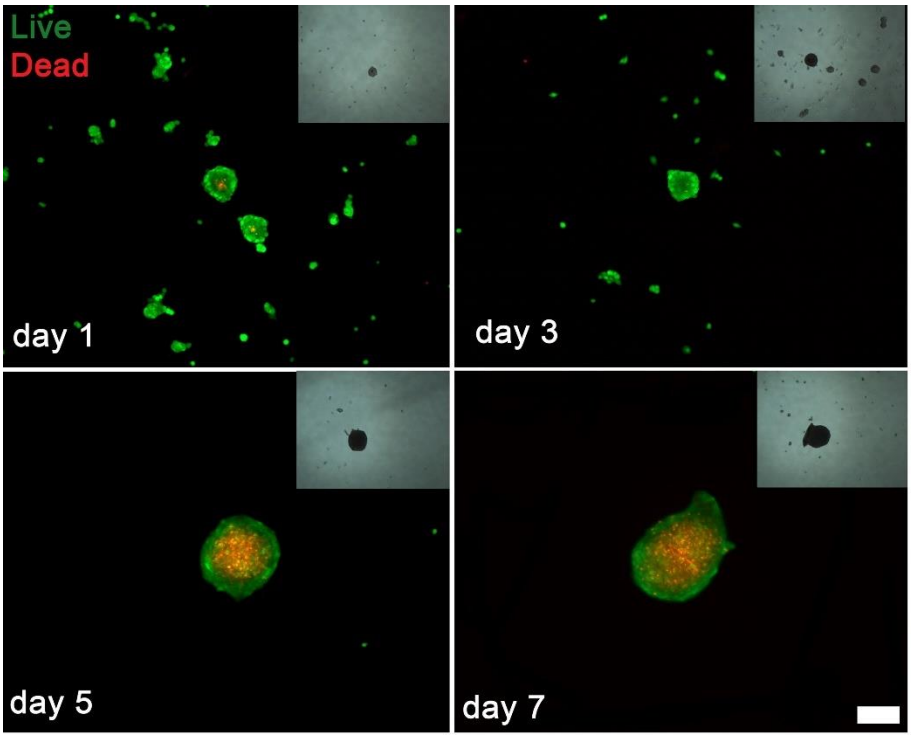

Figure 3.10. Cell viability images of NIH/3T3 spheroids for varied cell culture times on day 1, 3, 5,7 (green: live cells, red: dead cells). Scale bar: 200 µm

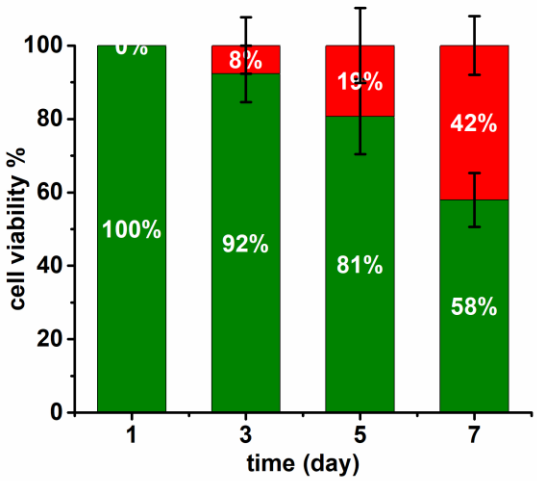

Figure 3.11. Cell viability images of NIH/3T3 spheroids for varied cell culture times on day 1,3, 5,7.

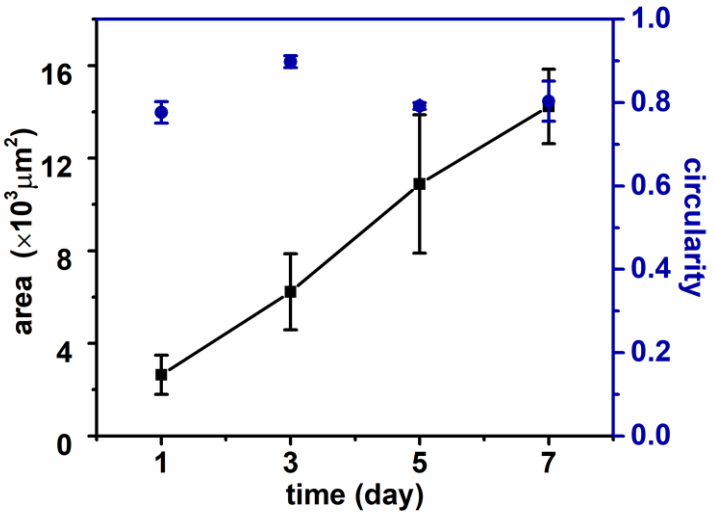

Figure 3.12. Representative spheroid area versus circularity for varied cell culture times on day 1, 3, 5, 7.

In tissue engineering applications, spheroids are classified and used according to their sizes, especially spheroids ranging 10-100 µm are used in drug screening studies and fundamental studies [135] and spheroids between 100-1000 µm are utilized in transplant models for *in vivo* research of animal models and the replacement of organs, [136–138] and larger spheroids around 1000±300 µm can be used in regenerative medicine applications. [139,140] Not only spheroid size but also necrotic core formation is a significant property for a tumour model to represent in vivo tumour microenvironment very closely. It is well known fact that spheroid models with necrotic core formation are more resistant to chemo- and radiotherapies compared to 2D cell cultures. [73,141] For that reason, we foresee that developed 3D spheroid models of this work would be good alternatives to conventional methodologies for the formation of 3D spheroids with tunable properties, and also they would be an alternative platform for 3D tumour models with studies as well.

Moreover, these results support that it is possible to obtain tunable 3D cellular structures by changing initial cell number, Gx concentration and culture time using this developed MagLev methodology.

3.1.5. Characterization of 3D Cellular Structures

Immunostaining of F-Actin, nuclei, and Collagen Type-I was carried out to analyzethe presence of cellular and extracellular components of short-term (day 1) and long-term (day 7) cultured spheroids. As given in Figure 3.13A, cells started to interact with each other starting from day 1 and formed 3D cellular structures, where the nuclei of cells and actin filaments were observed clearly. Actin is one of the cytoskeleton molecules that has important tasks such as adhesion, cell motility, and signalling. [142] The role of actin filaments in spheroid formation is that they organize ordered structures while maintaining their conformational changes. [77] During spheroid formation, spontaneous cell-cell interaction forms cellular aggregation and cells start to secrete their ECM molecules into the aggregate to form a solid spheroid structure. [143] Cells continued to proliferate and form much larger spheroid structures on day 7, as shown in Figure 3.13B. Collagen is one of the main ECM components, therefore ECM secretion was affirmed within the 7-day cultured spheroids by positive staining for Collagen Type-I, while no Collagen formation was obtained for 1-day cultured spheroids, indicating that 24 hr culture time is not enough for Collagen secretion.

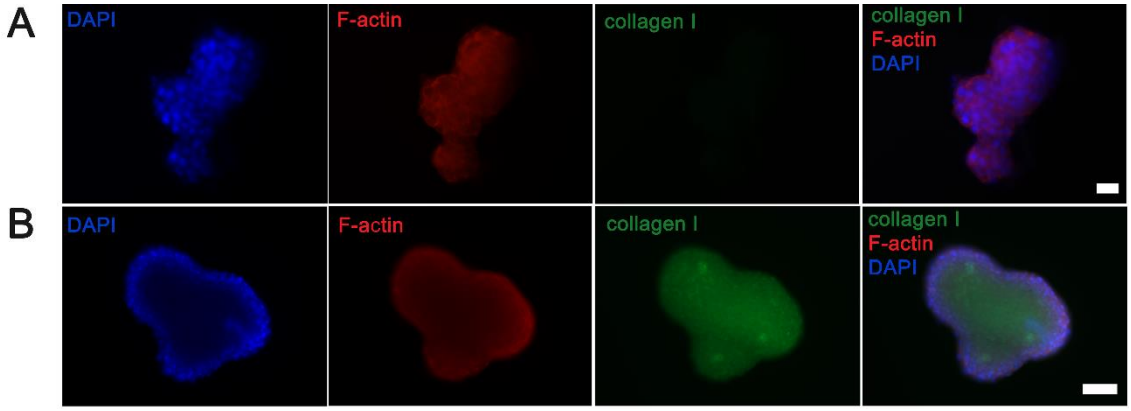

Figure 3.13. Immunofluorescence staining of NIH/3T3 spheroids on A) day 1 scale bar: 20 µm and B) day 7 scale bar: 50 µm.

3.1.6. Fabrication of 3D Tumour Structures via Magnetic Levitation

Applicability of the developed MagLev system was examined for biofabrication of 3D tumour models by using different cell lines. Varied cancer cell lines; MCF7, MDA-MB-231, HeLa, SH-SY5Y, PC-12 were investigated in terms of spheroid formation. 10×10^3 cells and 10 mM Gx were used during culturing for all cancer cell lines. However, unlike the MCF7, SH-SY5Y, and PC-12 cell lines, the magnetic field was not enough to levitate the MDA-MB-231 and HeLa cell lines. Therefore it was increased from 0.15 T (40×5 mm magnet) to 0.4 T (30×15 mm magnet) to obtain levitated 3D structures. Figure 3.14 shows the light microscopy and cell viability images of spheroids that were obtained from various cancer cell lines at different incubation times. A small and compact 3D self-assembly structure was obtained with a SH-SY5Y cell line at 24 hr, as seen in Figure 3.14A. However, other cancer cell lines like MDA-MB-231, MCF7, PC-12 and HeLa formed the less-dense 3D structures o as shown in Figure 3.14 B, 3.14 C, 3.14 D and 3.14 E respectively.

In contrast to the 3D structure of the SH-SY5Y cell line, which had a very tight structure, the PC-12 cell line formed a less dense 3D structure, as seen in Figure 3.14D. This was achieved by the cell adhesion molecules, which has a significant role in cell-cell contact and tissue development. [144] This behaviour of SH-SY5Y cell line overlaps well with the current literature findings where CAM and ECM proteins for spheroids of the SH-SY5Y cell line were investigated for first time by Jung et al. (2013). Spheroids were obtained by using hydrophobic surfaces of the thermally collapsed elastin-like polypeptide for 48 hr. CAM protein levels of SH-SY5Y cell line spheroids were compared to 2D cell culture that result in higher levels of N-cadherin (3-fold) which are probably related to the tight structure of the spheroid. [149148]

At first, to obtain 3D structures for the MDA-MB-231 cell line (human breast adenocarcinoma cell line, estrogen-independent), a 40×5 mm magnet was used and various Gx concentrations were applied (10, 30, and 50 mM). However, levitated 3D structures were not obtained. Therefore, magnetic field strength was increased to 0.4 T by using a 30×15 mm magnet. Levitated but less dense 3D structures were obtained after 48 hr and the cell viability was high, as given in Figure 3.14B. This is probably related to the adhesion molecule integrin β1 and the tight junction protein claudin4 of MDA-MB-231.[145] On the other hand, the MCF7 cell line (human breast

adenocarcinoma cell line, estrogen-dependent) formed 3D structures at around 12 hr (Figure 3.14C). However, to observe morphological changes during culture time it was incubated for 72 hr. The 3D structure was not as compact as the spheroid structure of NIH/3T3 or SH-SY5Y cells at 72 hr. Ivascu and Kubbies (2007) investigated the spheroid formation of eight breast cancer cell lines in terms of cellular adhesion molecules. Their studies showed that different adhesion molecules participate in the spheroid formation of breast cancer cell lines. E-cadherin intercedes the formation of the spheroid in MCF7. However, MDA-MB-231 cells have no cadherin molecules: their spheroid formation is conducted by the collagen I/integrin ß1 interaction. In addition to this, as seen in Figure 3.14B, high cell viability was observed in larger 3D structures. Since lose 3D structures were obtained for these cells no diffusion gradient occurred.

Smaller and intermittent the 3D structure formation was observed for Hela cell line at 96 hr with high cell viability (Figure 3.14E). Compared to other cell lines, a very small (below 200 µm) and a high number of spheroids were obtained. In literature it is reported that HeLa cells synthesize N-cadherin and catenin that build cell-cell junctions for spheroid formation. Cadherins connect with the actin cytoskeleton, which results in strong cell-cell adhesion. [146] Also, Ho et al. (2010) reported that F-actin is responsible for the reorganization of the cytoskeletal structure via the formation of intercellular linkages in spheroid formation because high-level F-actin was observed in 3D cell culture compared to 2D cell culture. [147]

These results explain that spheroid morphology is mainly related with the type of the cell line but can also be manipulated by changing system parameters. Taken together, these results further indicate the applicability of the MagLev methodology on 3D tumour spheroid formation while emphasizing the effect of CAM and ECM molecules to support cell-cell adhesion and cellular assembly.

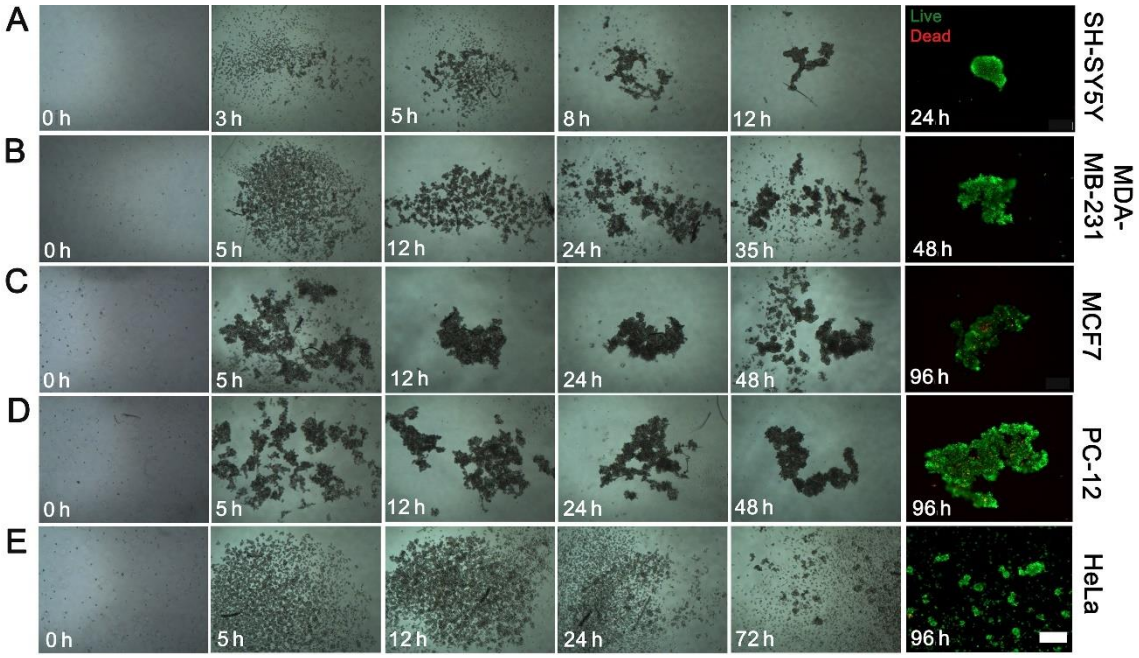

Figure 3.14. Time-dependent light microscopy images of 3D tumour spheroid formation with using magnetic levitational assembly and cell viability of 3D tumour spheroids for different cancer cell lines. A) SH-SY5Y, B) MDA-MB-231, C) MCF7, D) PC-12, and E) HeLa. Scale bar: 100 µm.

3.1.7. Fabrication of 3D Co-Culture Models via Magnetic Levitation

Again, to show the applicability of the MagLev system for co-culture formation, MDA-MB-231 GFP and MDA-MB-231 dsRED cell lines were used to form a co-culture model. Co-cultured spheroids were obtained with 10×10^3 cells, 30×15 mm magnet (0.4 T), while the Gx concentrations were kept as 50 mM and 100 mM, as seen in Figures 3.15 and 3.16 respectively. Gx concentration effect can be observed with regard to spheroid formation time and spheroid morphology. Aggregation was observed at 24 hr and small and compact 3D structures were obtained at 120 hr (Figure 3.15) when 50 mM Gx was applied. On the contrary, a higher Gx concentration (100 mM) promoted faster and bigger co-culture assembly, where cellular aggregates started to form at around 5 hr. A 3D co-culture structure was observed at 72 hr that had a less dense structure, as seen in Figure 3.16. Co-culture techniques are significant models for forming tissue structures to investigate cell-cell interactions. These interactions occur through direct intercellular contact and signalling molecules that are synthesized by cells. [148] For that reason, co-culture models are more dependable systems for mimicking

in vivo tissue models for many tissue engineering studies such as drug research on tumoroid models. [149,150] This application showed that the formation of a co-culture model was possible by using a MagLev setup.

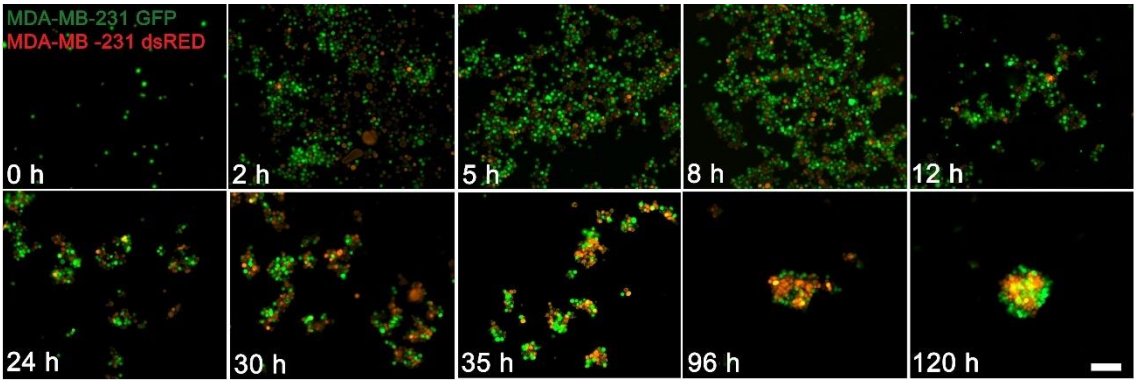

Figure 3.15. Time-dependent fluorescent microscopy images of 3D co-culture model formation at 50 mM Gx. Scale bar: 100 µm.

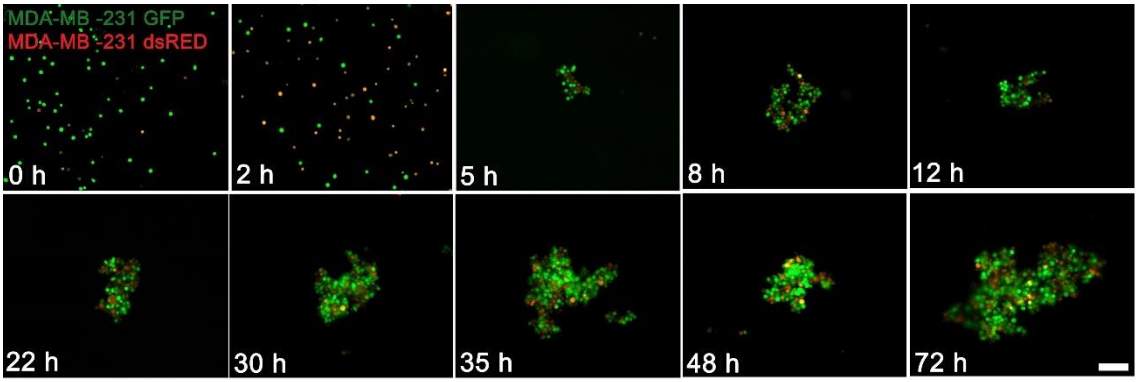

Figure 3.16. Time-dependent fluorescent microscopy images of 3D co-culture model formation at 100 mM Gx. Scale bar: 100 µm.

3.1.8. Cytotoxicity Screening of Paramagnetic Agents on H9c2 Rat Cardiomyocytes

Three commercially available paramagnetic agents gadobutrol (Gx), gadodiamide (Ox), and gadoteric Acid (Dx) were investigated in 2D cell culture to evaluate their cytotoxicity on H9c2 cell line. These paramagnetic agents were choosen based on their ionic/non-ionic, macrocyclic/linear chain characteristics. [76] As given in

Figure 3.17, Gx has a low cell toxicity effect on H9c2 cells compared to the control group which was not treated with any paramagnetic agents. Dx has moderate toxicity on cells, as observed in Figure 3.18. However, Ox had a high cytotoxic effect compared to other paramagnetic agents on H9c2 cells for short- and long-term incubation. As observed in Figure 3.19, increased Ox concentrations resulted in high cell cytotoxicity. Also, as shown in Figures 3.20, 3.21, and 3.22, the Alamar Blue assay results support the Live/Dead assay analysis, and Gx was found to be the most appropriate paramagnetic agent for cell culture studies. The reason for the toxicity of these agents was the release of free gadolinium ions and that related to the stability and half-life of agents. Gx showed low toxicity on 2D cultured cells compared to other agents due to their longer half-life, and longer half-life resulted in the low release of the Gadolinium ion. A main reason for the higher toxicity of Ox is the fast dissociation of its ligand, releasing gadolinium ions due to its linear chain ligand structure. The half-life of Ox is 0.01 hr, which is ~ 700- and ~ 2300-fold faster than those of Dx and Gx, respectively. [76,151] Therefore, Gx was used during 3D cell culture studies due to its low toxic effect on H9c2 cells.

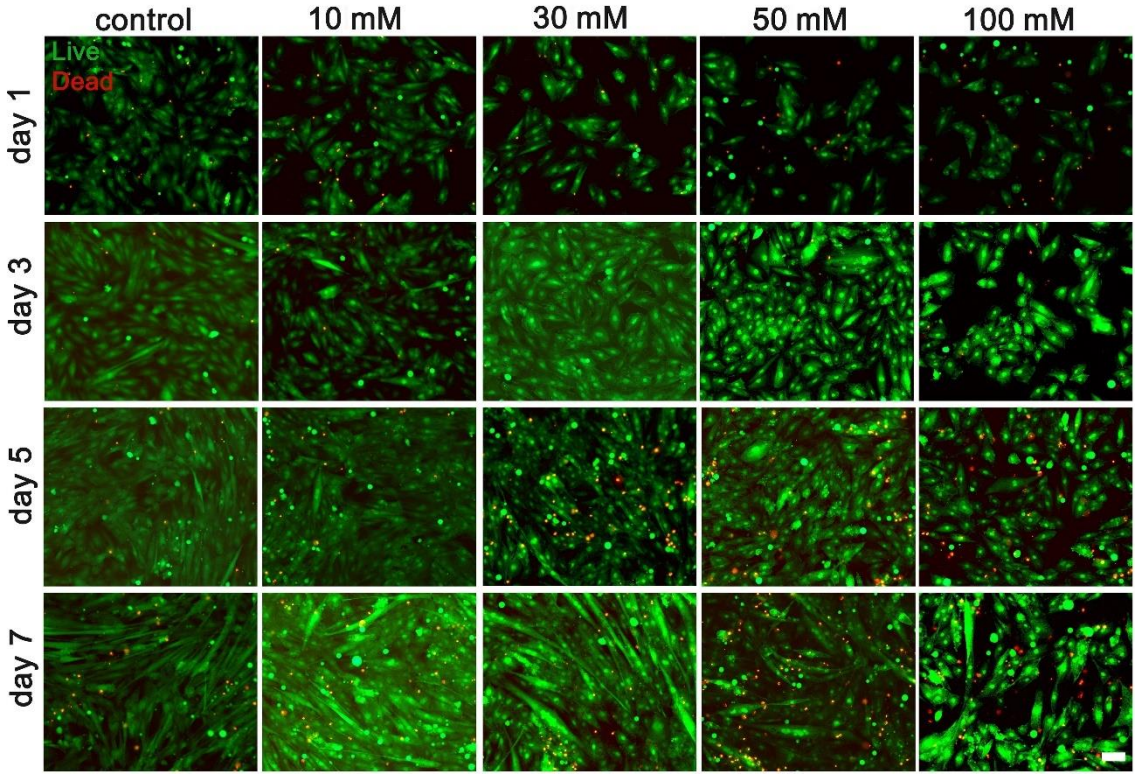

Figure 3.17. Cell viability images of H9c2 cells treated with Gx in varied concentrations (0/10/30/50/100 mM) in long-term culture (1/3/5/7 days). Scale bar: 100 μm.

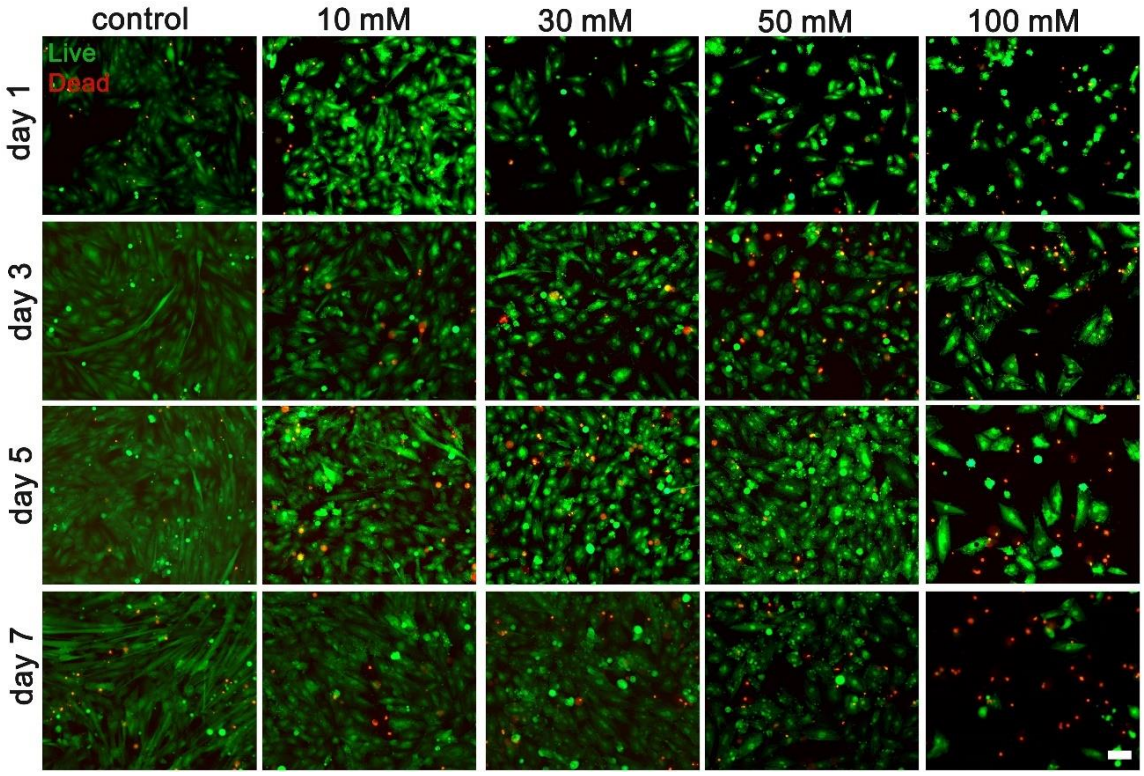

Figure 3.18. Cell viability images of H9c2 cells treated with Dx in varied concentrations (0/10/30/50/100 mM) in long-term culture (1/3/5/7 days). Scale bar: 100 µm.

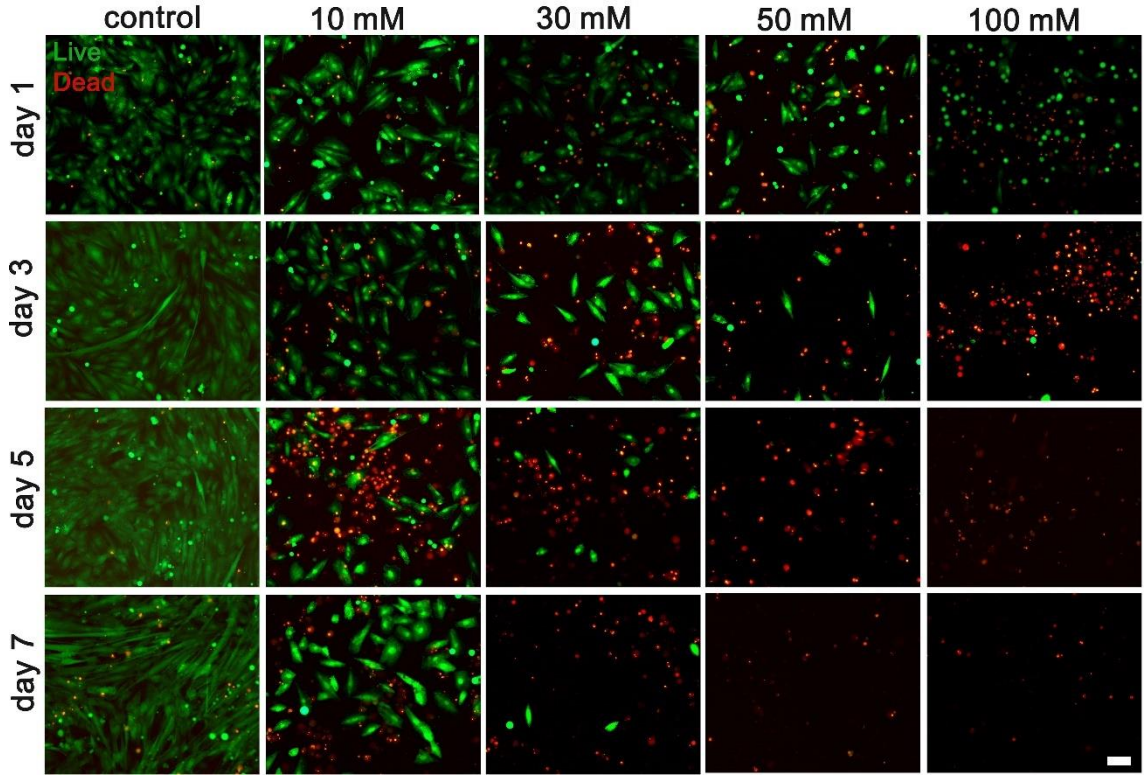

Figure 3.19. Cell viability images of H9c2 cells treated with Ox in varied concentrations (0/10/30/50/100 mm) in long-term culture (1/3/5/7 days). Scale bar: 100 µm.

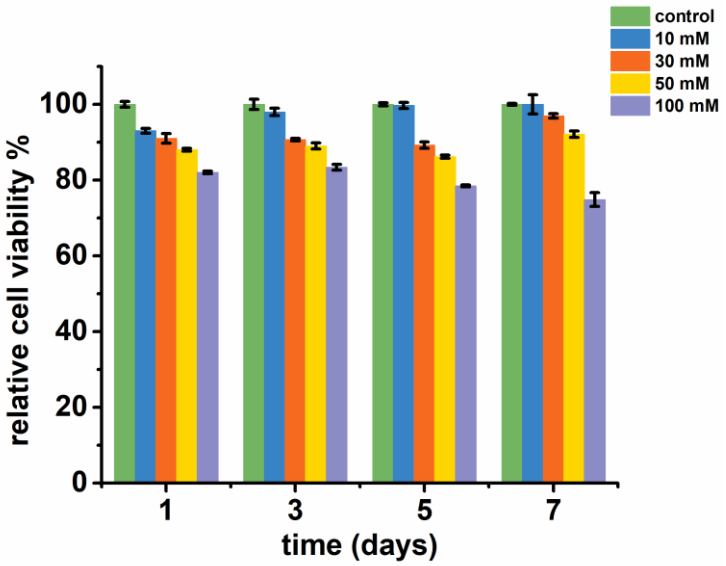

Figure 3.20. Relative cell viability % of H9c2 cells treated with Gx in varied concentrations (0/10/30/50/100 mM) in long-term culture (1/3/5/7 days).

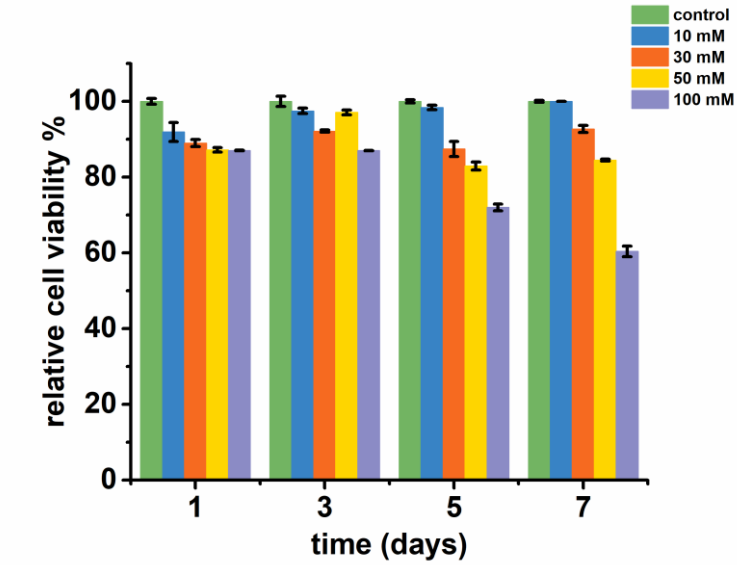

Figure 3.21. Relative cell viability % of H9c2 cells treated with Dx in varied concentrations (0/10/30/50/100 mM) in long-term culture (1/3/5/7 days).

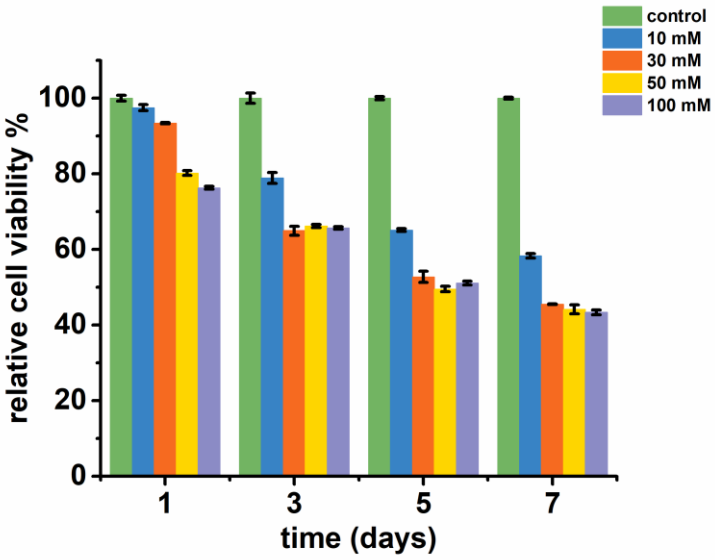

Figure 3.22. Relative cell viability % of H9c2 cells treated with Ox in varied concentrations (0/10/30/50/100 mM) in long-term culture (1/3/5/7 days).

3.1.9. Biofabrication of 3D Cardiac Spheroids

Prior to the biofabrication of 3D cardiac spheroids, cell seeding number, Gx concentration and culture time was optimized. Effect of cell seeding numbers: 2.5, 5, 10, and 25×10^3 were investigated first, as given in Figure 3.23. As given in Figures 3.23 and 3.24, low cell number (2.5 and 5×10^3 cells) resulted in high cell viability (above 50% cell viability) compared to high cell number (10 and 25×10^3 cells). The reason for low cell viability is diffusion limitation as explained previously. Later, circularity values were calculated for 3D cardiac structures where the circularity of spheroids was calculated as 0.79, 0.87, 0.85, and 0.89 for 2.5, 5, 10, and 25×10^3 cell densities respectively (Figure 3.25). These results showed that spheroids obtained through varied cell numbers are close to an ideal spheroid shape. In addition to the circularity values of spheroids, area change was calculated against increasing cell number. As shown in Figure 3.25, spheroid areas were obtained as 2.8, 5.6, 8.7, and 35.3×10^4 μm^2 for 2.5, 5, 10, and 25×10^3 cell numbers respectively. These results also support that the spheroid size and area can be tuned by changing initial cell number, also confirming the previous result that was observed by using NIH/3T3 cells.

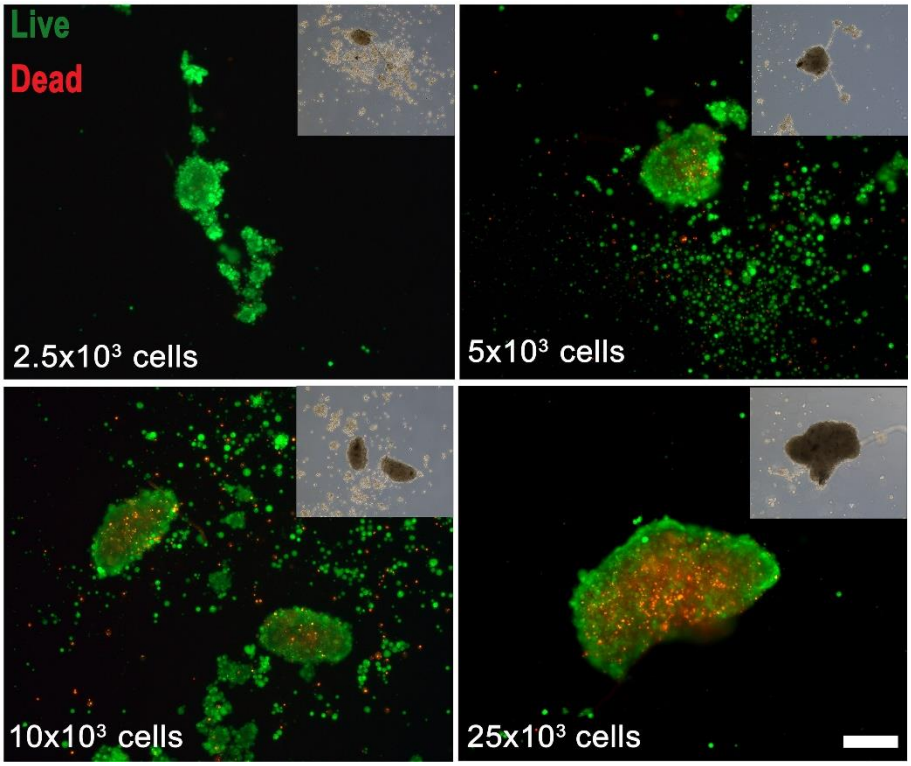

Figure 3.23. Cell viability images of H9c2 spheroids for various initial cell numbers; 2.5, 5, 10, 25×103. Scale bar: 200 µm.

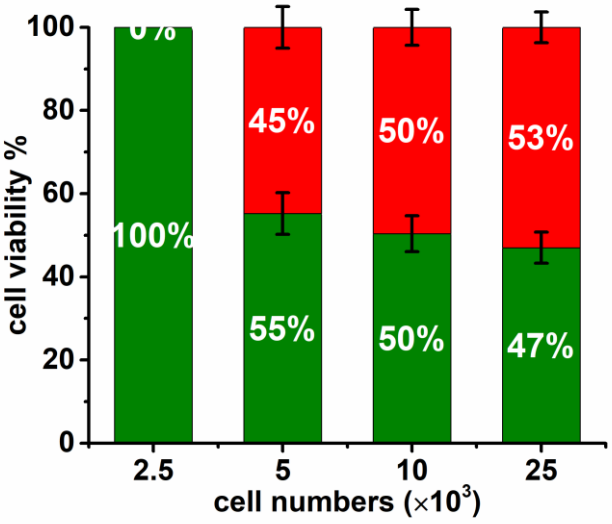

Figure 3.24. Cell viability % values of H9c2 spheroids for various initial cell numbers; 2.5, 5, 10, 25×10^3.

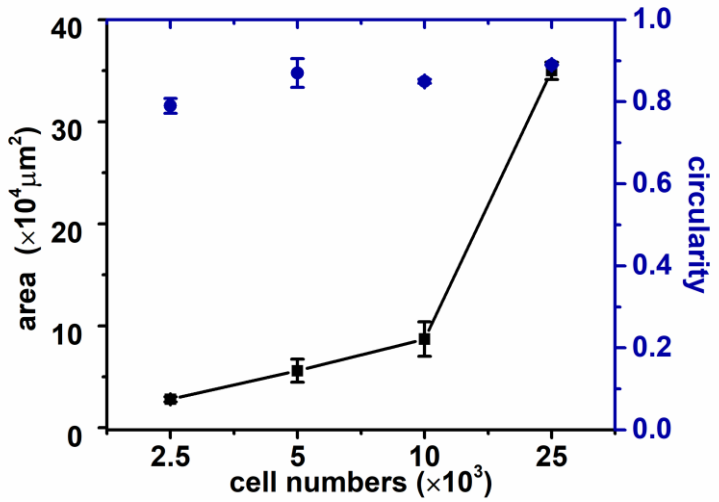

Figure 3.25. Representative spheroid area versus circularity of H9c2 spheroids for various initial cell numbers; 2.5, 5, 10, 25×10^3.

In addition to cell seeding number optimization, the effect of high Gx concentrations on spheroid formation and cell viability was investigated. Varied Gx concentrations such as 10, 30, 50, and 100 mM were applied while cell number was kept as 2.5×10^3 H9c2 cells as given Figure 3.26. Here, higher Gx concentration did not

result in a larger spheroid structures. [4,123] For that reason, 10 mM Gx was used for 3D cellular structure and spheroid formation because heterogenous H9c2 cells are aligned very close to each other by low magnetic forces at 10 mM Gx.

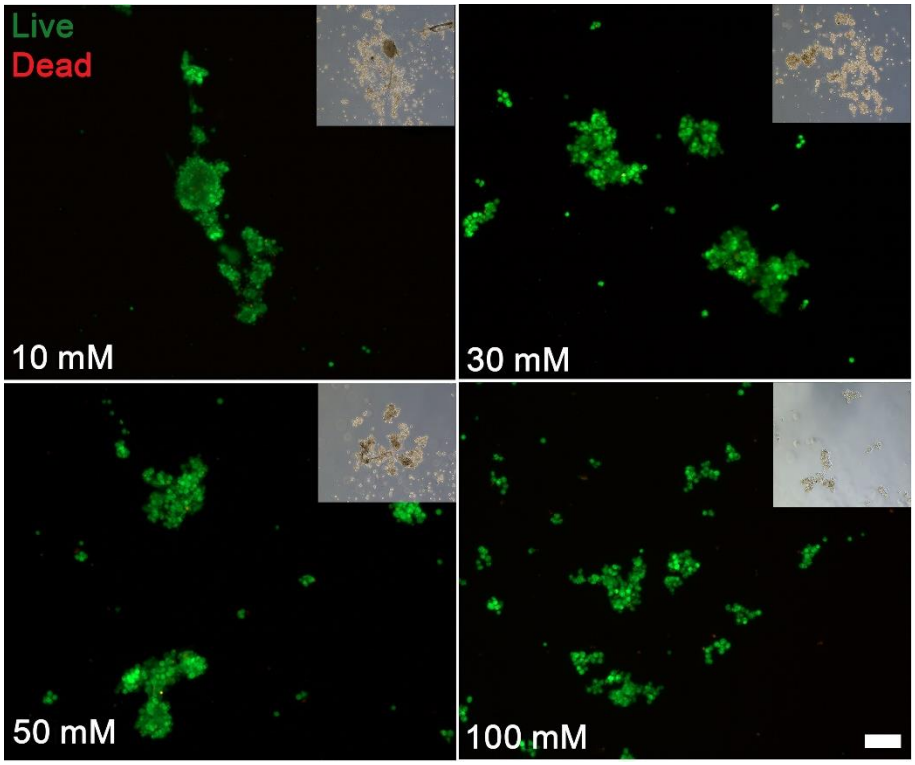

Figure 3.26. Cell viability images of H9c2 spheroids in varied Gx concentrations: 10, 30, 50 and 100 mM. Scale bar: 200 µm.

During long-term culture studies of 3D cardiac spheroids, initial cell number was used as 2.5×10^3 while Gx concentration was kept as 10 mM. Light microscopy images of 3D cellular structures were given in Figure 3.27**.** Around 3 hr, cells started to accumulate in the centre of the petri dish, and at around 5 and 8 hr, accumulated single cells turned into cellular aggregates. Increased cell-cell interaction resulted in the formation of spheroids at 22 hr. During the increased culture time (48, 72, 96, and 120 h), these small spheroids started to fuse and became larger and more compact spheroid structures.

The long culturing time of 3D cardiac spheroids was also investigated in terms of cell viability. As shown in Figures 3.28 and 3.29, the highest cell viability was 100% for 24 hr cultured 3D spheroids. Increased culturing time resulted in gradual decrease in cell viability; 65, 54, and 53% of cell viability was calculated for day 2, day 3, and day

4 respectively. At the end of day 5, the cell viability was 48% due to the diffusion limitation. In addition to cell viability, long-term cultured spheroids were also characterized in terms of area and circularity. Spheroid area and circularity were calculated, as given in Figure 3.30. The spheroid area was increased dramatically to 4.2 $\times 10^4$ μm^2 at day 2 because small 3D cellular structures were combined and formed a larger spheroid. Then this structure turned into a more compact structure after 24 hr. For that reason, the area of the spheroid started to decrease at the end of day 2. Area change was calculated as 3.7, 2.9, and 2.8 $\times 10^4$ μm^2 for day 3, day 4, and day 5 respectively. Circularity values of spheroids were obtained as 0.79, 0.76, 0.81, 0.83, and 0.82 for day 1, day 2, day 3, day 4, and day 5 respectively. This result supports that spheroids maintain their circular structure during culture time.

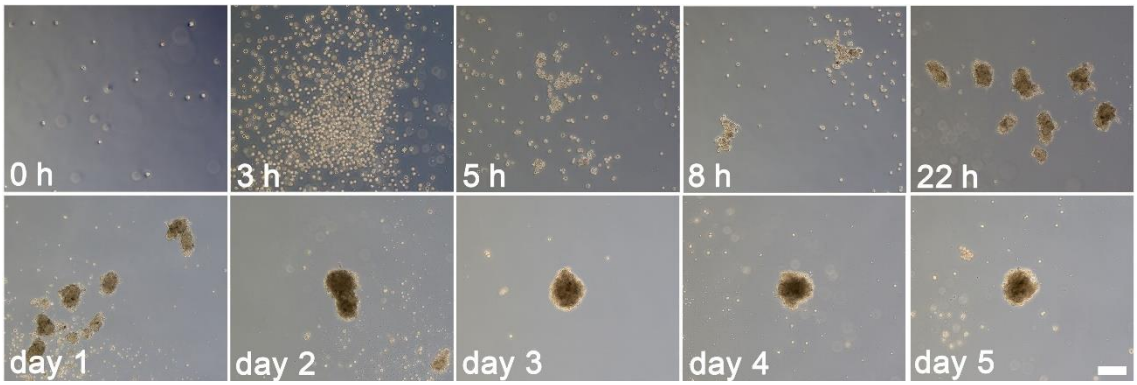

Figure 3.27. Time-dependent light microscopy images of spheroid formation for H9c2 cells via magnetic levitational assembly at 0, 3, 5, 8, 22, 24, 48, 72, 96, and 120 hr. scale bar:200 µm.

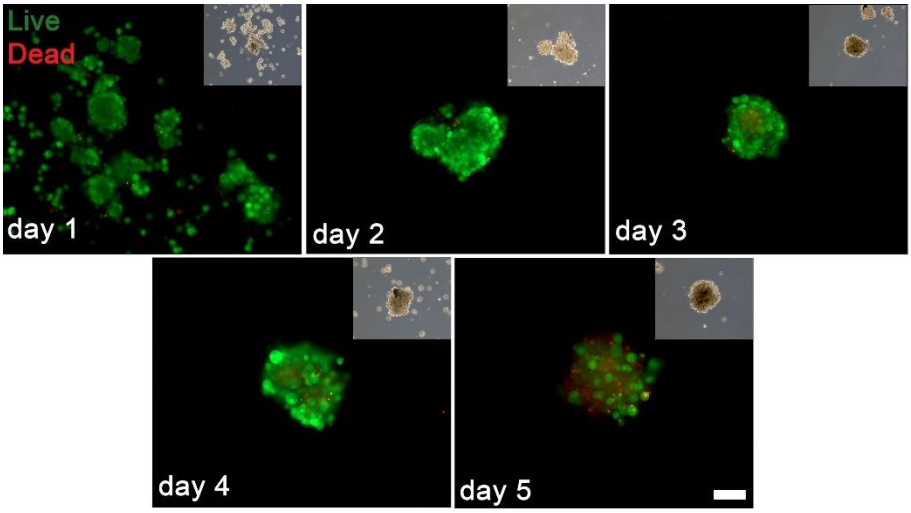

Figure 3.28. Cell viability images of H9c2 spheroids for various cell culture times (days 1/2/3/4/5). Scale bar: 200 µm (green: live cells, red: dead cells).

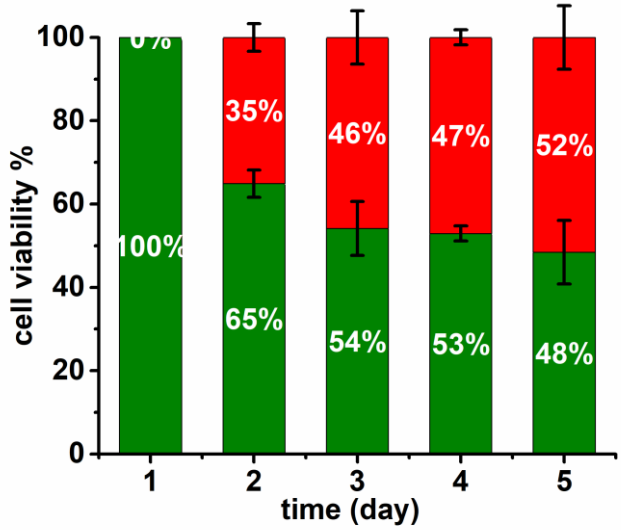

Figure 3.29. Cell viability values of H9c2 spheroids for varied cell culture times on days 1, 2, 3, 4, 5.

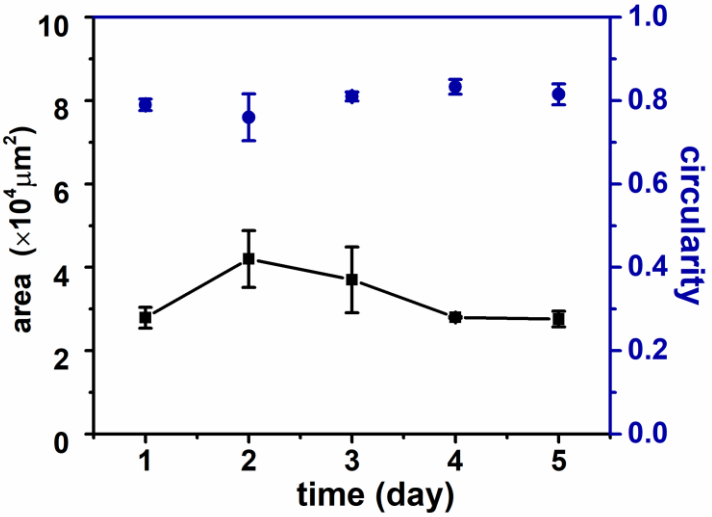

Figure 3.30. Representative spheroid area versus circularity for varied cell culture times on day 1, 2, 3, 4, 5.

3.1.10. Characterization of 3D Cardiac Spheroids

To characterize the 3D cardiac spheroids, cellular and ECM components were investigated via immunostaining of F-actin, and collagen type I, and DAPI nuclear staining. The nuclei of cells and the cytoskeleton component of F-actin were observed clearly for short- (day 1) and long-term (day 5) cultured 3D cardiac spheroids, as given in Figure 3.31. Collagen I is a significant component of the ECM that was also observed for short- and long-term cultured cardiac spheroids. [152] Compared to day 1 (Figure 3.31A), 3.7 fold higher fluorescence signal intensity was calculated [153] for day 5 cardiac spheroid (Figure 3.31B) which indicates that Collagen I secretion increased during long term culture.

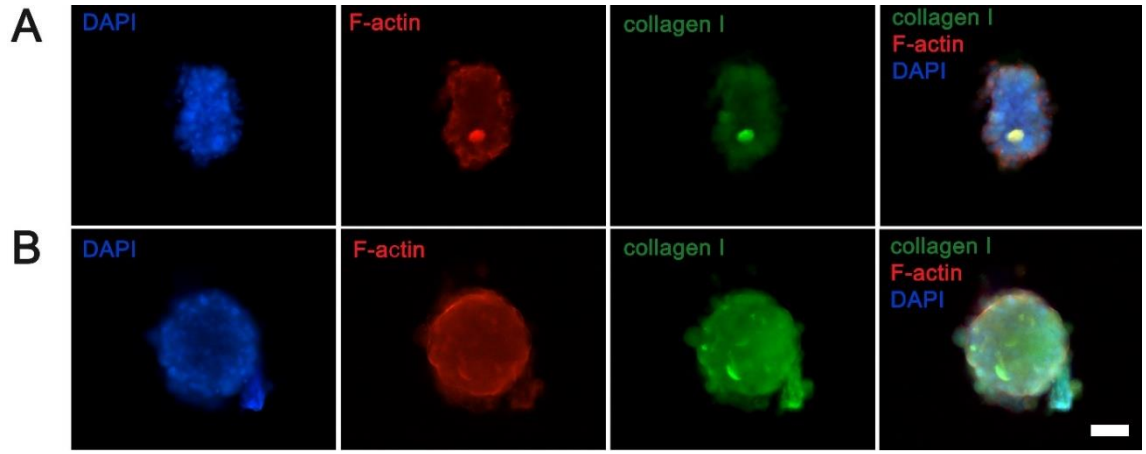

Figure 3.31. Immunofluorescence staining of H9c2 spheroids on A) day 1 B) day 5 Scale bar: 50 µm.

Moreover, to demonstrate the secretion of specific cardiac markers, cardiac troponin T and MYH6 immunofluorescence staining was performed for 3D cardiac spheroids. As shown in Figure 3.32A and Figure 3.32B, cardiac troponin T was observed for both day 1 and day 5, which is a cardiac regulatory protein that controls the calcium-mediated interaction between actin and myosin. [154] Also, MYH6 that encodes for the 1 α-cardiac myosin heavy chain is expressed primarily in the atria [155] was clearly observed for cardiac spheroids for both day 1 and day 5, as given in Figure 3.32C and Figure 3.32D. Moreover, DAPI staining was applied to observe the nuclei of cells.

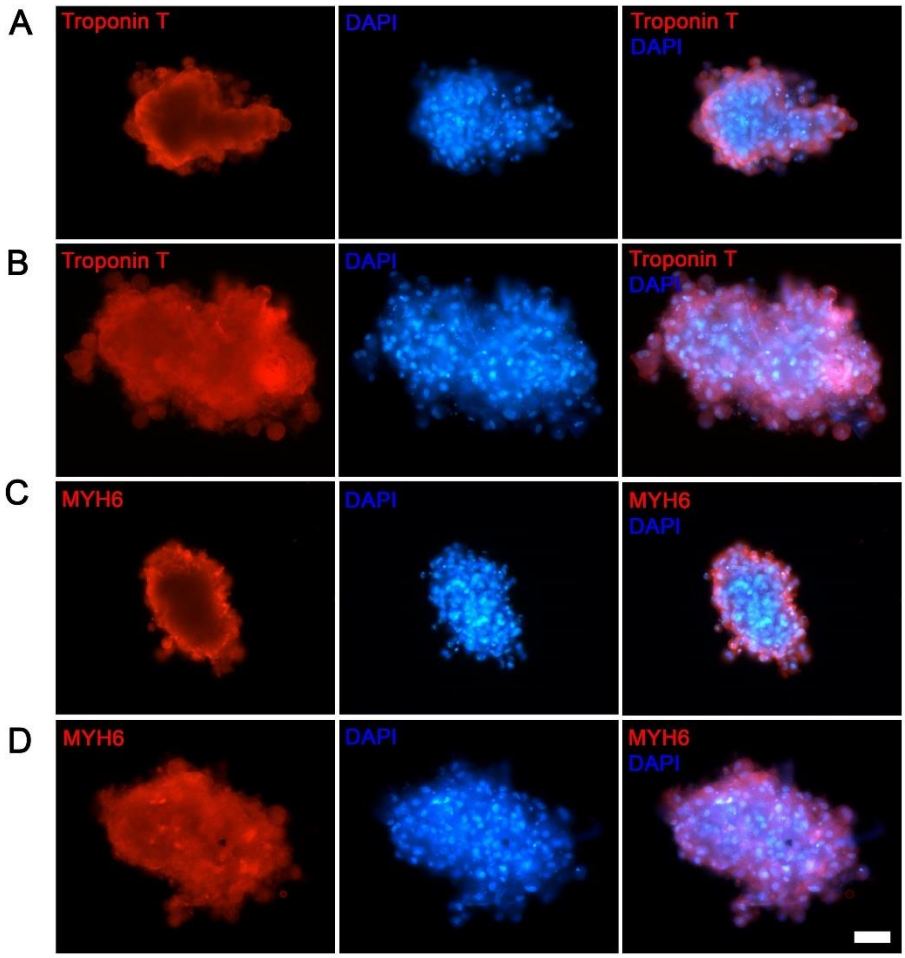

Figure 3.32. Immunofluorescence staining of H9c2 spheroids for cardiac markers of cardiac Troponin T on A) day 1 B) day 5 and MYH6 on C) day 1 D) day 5 Scale bar: 50 µm.

3.1.11. Dox-Induced Cardiotoxicity Study

To evaluate the drug response of cardiac spheroids that were fabricated through MagLev; 0, 1, 5, 10, 25, and 50 µM DOX were applied. DOX-applied 3D cardiac spheroids are given in Figure 3.33A, and the compact structure of spheroids turned into loose structures with the increased DOX concentrations but did not completely disperse. To evaluate DOX toxicity on spheroids, a MTT assay was performed, and formazan intensity was evaluated for cell toxicity. As expected and also observed in Figure 3.33B, formazan intensity decreased while DOX concentration increased. IC_{50} values were calculated as 3.5 and 14 µM for 2D control and 3D cardiac spheroids respectively (Figure 3.34). These results support that 3D cardiac structures are more resistant to drug

exposure. In addition to this, t-test analysis was done and resulted in drug responses of 2D cell culture and 3D cardiac spheroids being significantly different ($p < 0.05$).

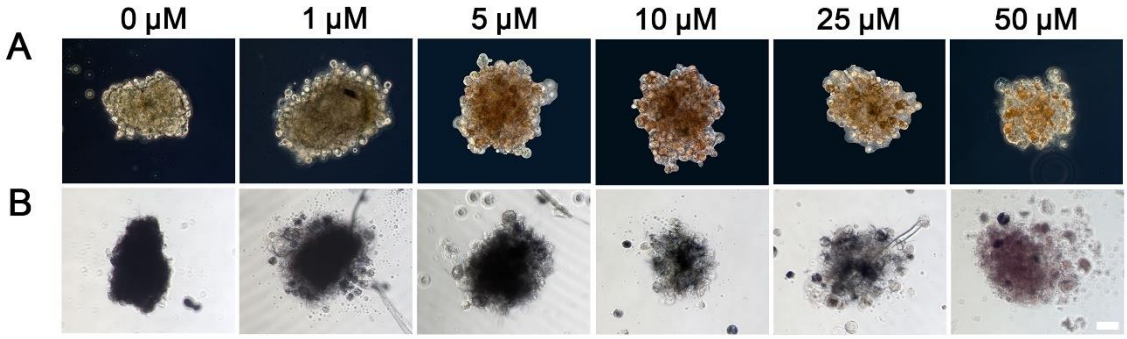

Figure 3.33. Light microscopy images of a) 0, 1, 5, 10, 25, and 50 µM DOX applied 3D cardiac spheroids; b) Formazan complex formation in 3D cardiac spheroids. Scale bar: 20 µm.

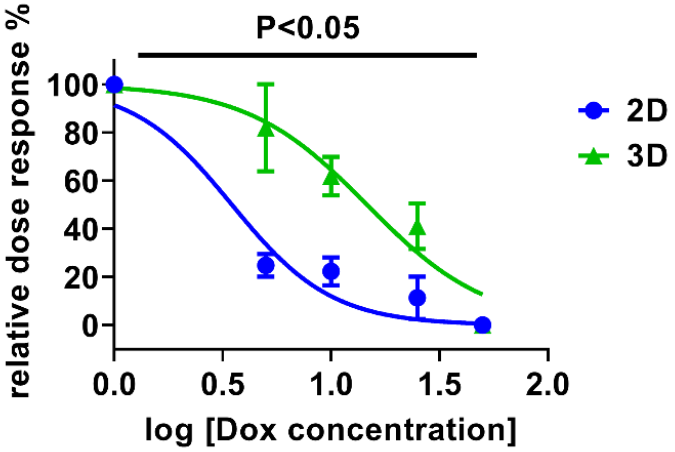

Figure 3.34. Dose response curves of 2D standard control and 3D cardiac spheroids. Error bars represent the standard error of mean, $p < 0.05$.

In literature response cells in 2D and 3D cell cultures has been investigated in terms of drug resistance. [134,156,157] Recently, varied spheroid models were developed, and their drug responses were evaluated via IC_{50} and EC_{50} values. Sirenko et al. (2017) fabricated 3D spheroids using human-induced pluripotent stem cell-derived cardiomyocytes via an ultra-low attachment (ULA) well plate. Then, they investigated 22 cardioactive and cardiotoxic drugs including DOX, and EC_{50} values were found to

be > 30 and 11.9 µM for 3D iPSC-derived cardiac spheroids and 2D control respectively. They indicate that 3D cardiac spheroids are more resistant to toxic drugs and more suitable for *in vitro* models. [158]

The reason for these significant differences is that cells have better cell-cell and cell-ECM interactions, which mimic the physiological microenvironment closely in 3D cell culture. Also, in a 3D spheroid structure, cells maintained their phenotype, function, and synthesize ECM. Moreover, exposure of molecules between cells on the exterior and cells in the interior are completely different in 2D cell culture where cells have uniform exposure. [159–162] Taken together; in this work it is successfully shown that 3D cardiac spheroids fabricated via MagLev are more resistant to drug exposure then conventional 2D model.

3.2. Biofabrication of 3D Cell Culture Models via the Magnetic Biopatterning Method

3.2.1. Optimization of Bio-ink Formulation by Using Experimental Design Models

In this study, optimization was carried out utilizing Plackett Burman and Box Behnken experimental design models. As given in Table 2.1, 8 parameters were considered to obtain 3D cellular structures. Plackett-Burman design was used to decrease the number of parameters and to determine effective parameters that contribute the most to 3D patterned structures. [163] Alginate is a natural polysaccharide that is composed of (1–4)-linked D-mannuronic acid (M units) and (1–4)-linked L-guluronic acid (G units) residues. Here, alginate is the main component of the bio-ink. Alginate forms gel, where there is a presence of divalent cations (Ca^{2+}, Sr^{2+}, and Ba^{2+}), through the ionic interaction between the cation and carboxyl group. Negatively charged G units (carboxyl group) and divalent cations form egg box structures. [164,165] Ca-alginate gelation occurs very rapidly when the $CaCl_2$ and Na-alginate meet in the same environment. [166] Gelation behavior of alginate depends on the concentration of alginate and Ca^{+2}, and their incubation time. Appropriate gelation parameters are required to obtain a hydrogel that allows cell attachment and also prevents cells dispersion out of

the hydrogel. For that reason, working parameters were defined as 0.08 and 0.5 % (w/v) alginate, 5 and 20 mM $CaCl_2$, 3 and 5 min incubation time. The parameter ranges were decided according to preliminary cell culture studies. The MNP enables contactless manipulation of cells under external magnetic field therefore, its concentration is another effective parameter for patterning of cells. Here, 400 and 800 µg/ml MNP concentration was used. On the other hand, cell density affect cell-cell and cell-ECM interactions, [167,168] where 5×10^5 and 1×10^6 cell numbers were investigated for optimization. The total volume was changing between 8–16 µl, adjusting the total volume is an important issue to get complete coverage of magnet surface while obtaining suitable alginate viscosity. As the last parameter of the Plackett-Burman design, incubation time of bio-ink was evaluated as 4 and 5 hours since this is the minimum time frame for cell adhesion.

As given in Table 3.1, 12 runs were performed to determine contribution percentage of parameters.

Table 3.1. Design of Plackett-Burman screening experiment with 8 parameters (F: Factor; Alg: Alginate).

Run	**F1: Alg. conc. (** w/v %**)**	**F2: Fe_3O_4 conc. (** µg/ml**)**	**F3: Cell number**	**F4: Alg. Volume** (µl)	**F5: Fe_3O_4 Volume** (µl)	**F6: $CaCl_2$ conc.** (mM)	**F7: $CaCl_2$ incubation time (min)**	**F8: Bio-ink incubation time** (h)
1	0.5	400	1×10^6	6	6	5	3	4
2	0.5	800	5×10^5	4	2	20	3	5
3	0.5	400	5×10^5	4	6	5	5	5
4	0.08	400	5×10^5	6	2	20	5	4
5	0.08	800	1×10^6	6	2	5	3	5
6	0.5	400	1×10^6	6	2	20	5	5
7	0.5	800	5×10^5	6	6	20	3	4
8	0.5	800	1×10^6	4	2	5	5	4
9	0.08	800	5×10^5	6	6	5	5	5
10	0.08	400	5×10^5	4	2	5	3	4
11	0.08	800	1×10^6	4	6	20	5	4
12	0.08	400	1×10^6	4	6	20	3	5

As seen in Figures 3.36 and 3.37, images show patterned bio-ink formulations in varying conditions between runs 1–12 according to the Plackett-Burman design model. Here, it was observed lower alginate concentration (0.08%) in run 5 resulted in a nicely patterned bio-ink compared to a higher alginate concentration (0.5%) in run 8 which caused random accumulation of bio-ink at fixed MNP (800 µg/ml) and $CaCl_2$ (5 mM).

Due to high alginate concentration (0.5%), gelation occurred before bio-ink patterned as the shape of magnet. Also, high concentration of $CaCl_2$ (20 mM) led to an accumulated bio-ink structure because of rapid gelation at run 2, run 4, run 6, run 7, run11, and run12 compared to the low concentration of $CaCl_2$ (5 mM) at run 5, run 9, and run 10. As a result, bio-ink with a suitable viscosity was obtained that would allow alginate take the shape of a magnet using appropriate alginate and $CaCl_2$ concentrations.

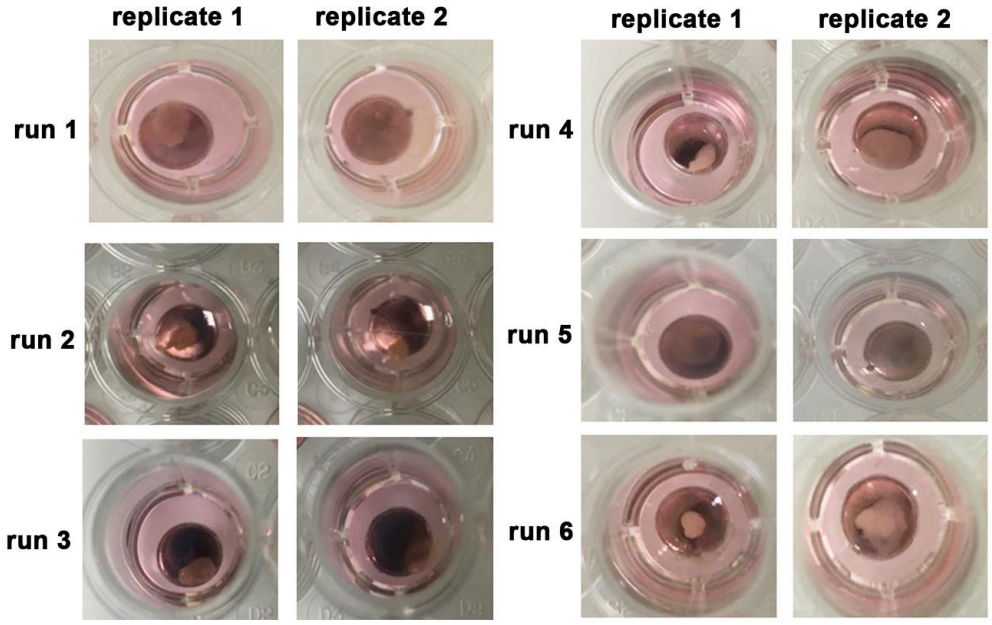

Figure 3. 35. Images of biopatterned bio-ink between runs 1–6.

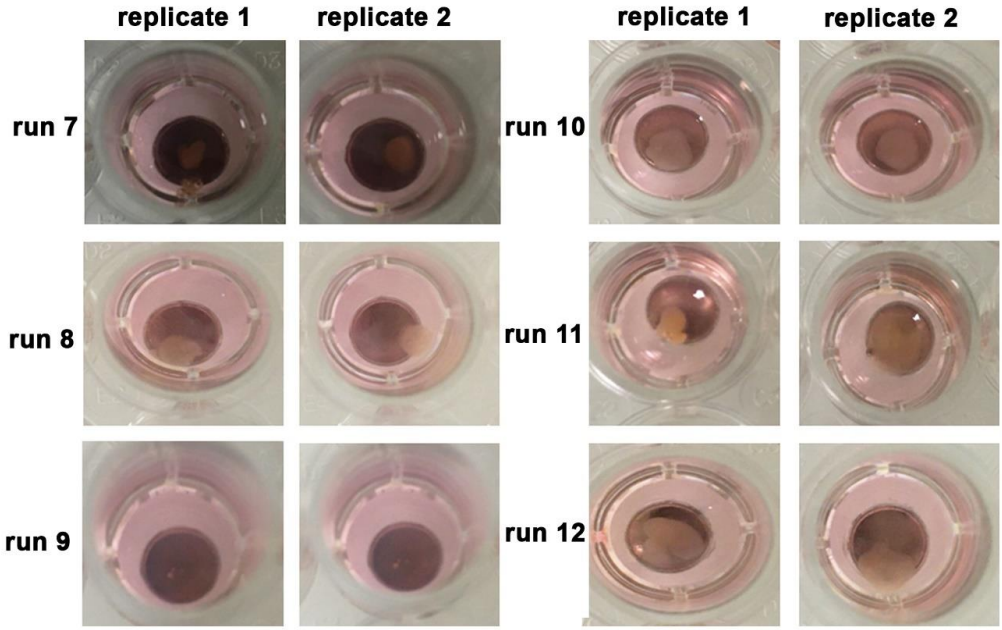

Figure 3. 36. Images of biopatterned bio-ink between runs 7–12.

As given in Figure 3.35 and 3.36, run 5 and run 9 were observed with nicely patterned bio-ink in the shape of a disc magnet. Moreover, light microscopy images of those two runs indicated that they had clear patterned bio-ink borders in the shape of a disc magnet, as given in Figures 3.37A and 3.37C. Also, after the disassociation step of alginate, patterned cells protected their borders as shown in Figures 3.37B and 3.37D. These two runs had the same parameters such as alginate concentration (0.08%), $CaCl_2$ (5 mM), MNP concentration (800 µg/ml), and incubation time of bio-ink (5 hr), while other parameters differed. The gelation rate was significant for obtaining a patternable bio-ink for this method, which was strongly related to alginate and $CaCl_2$ concentrations, as discussed previously. Therefore, low alginate and $CaCl_2$ concentrations resulted in patterned structures. Moreover, these two runs had another common parameter that was MNP concentration (800 µg/ml), and the high concentration also had a significant contribution to the well-defined borders of patterned bio-ink. On the other hand, cell number made a difference in patterned structures. As given in Figure 3.37D, low cell number (5×10^5) was not enough to form a 3D cellular structure on the microwell plate surface. This result supports that cell number is another important parameter for obtaining patterned structures. It is also important to point out the disassociation step for the formation of biopatterned structures. Disassociation of alginate occurs by elimination of calcium ions through the effect of chelators such as ethylenediaminetetraacetic acid (EDTA) and ethylene glycol-bis(β-aminoethyl ether)-N,N,N',N'-tetraacetic acid (EGTA), lactate, citrate, or phosphate agents. [169–172] This physical crosslinking property of alginate that association/disassociation reactions can be easily manipulated is one of the reasons that it was chosen in this study as a carrying agent, while encapsulating cells and MNPs. In this study, a citrate buffer (100 mM) was used for the disassociation of alginate. As seen in Figure 3.37B and 3.37D, patterned structures were observed after the disassociation and rinsing steps.

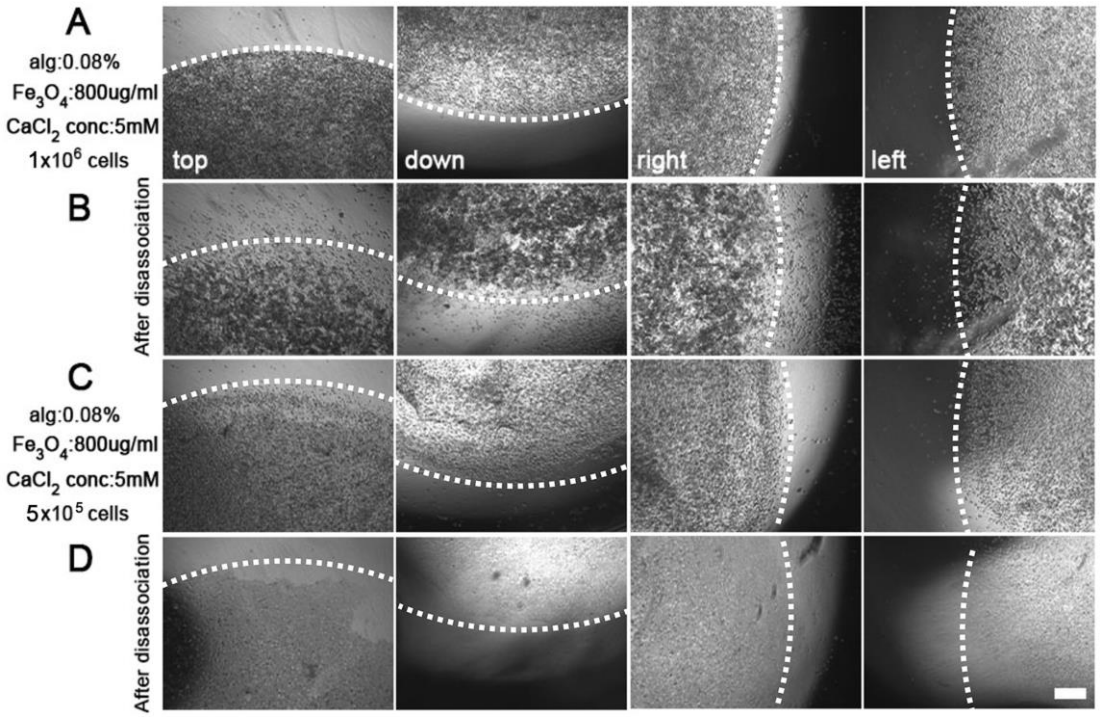

Figure 3.37. Light microscopy images of patterned cellular structures A) patterned bio-ink for run 5, B) patterned structures after disassociation of alginate for run 5, C) patterned bio-ink for run 9, D) patterned structures after disassociation of alginate for run 9. Scale bar: 200 µm.

Table 3.2. Screening experiment design via Plackett-Burman and results. (F: Factor, Alg: Alginate, R: Response).

Run	**F1: Alg. conc. (w/v %)**	**F2: Fe_3O_4 conc. (µg/ml)**	**F3: Cell number**	**F4: Alg. Volume (µl)**	**F5: Fe_3O_4 Volume (µl)**	**F6: $CaCl_2$ conc. (mM)**	**F7: $CaCl_2$ incubation time (min)**	**F8: Bio-ink incubation time (hr)**	**R1: cell patterning**
1	0.5	400	1×10^6	6	6	5	3	4	20
2	0.5	800	5×10^5	4	2	20	3	5	0
3	0.5	400	5×10^5	4	6	5	5	5	0
4	0.08	400	5×10^5	6	2	20	5	4	30
5	0.08	800	1×10^6	6	2	5	3	5	90
6	0.5	400	1×10^6	6	2	20	5	5	0
7	0.5	800	5×10^5	6	6	20	3	4	0
8	0.5	800	1×10^6	4	2	5	5	4	20
9	0.08	800	5×10^5	6	6	5	5	5	60
10	0.08	400	5×10^5	4	2	5	3	4	60
11	0.08	800	1×10^6	4	6	20	5	4	45
12	0.08	400	1×10^5	4	6	20	3	5	30

Table 3. 3. The contribution percentages of parameters was obtained from the Plackett-Burman design model.

Name	Contribution (%)
Alginate concentration (w/v %)	**66.88**
Fe_3O_4 concentration (µg/ml)	**4.97**
Cell number	2.68
Alginate volume (µl)	1.79
Fe_3O_4 volume (µl)	1.79
$CaCl_2$ concentration (mM)	**18.59**
$CaCl_2$ incubation time (min)	1.79
Bio-ink incubation time (hr)	0.022

Table 3. 4. ANOVA for the Plackett-Burman Screening Experiment.

Source	Sum of Squares	df	Mean Square	F-value	p-value Prob>F
Model	9383.33	8	1172.92	88.89	0.0018
A-Alginate conc	6302.08	1	6302.08	477.63	0.0002
B-Fe_3O_4 concentration	468.75	1	468.75	35.53	0.0094
C-Cell number	252.08	1	252.08	19.11	0.0222
D-Alginate volume	168.75	1	168.75	12.79	0.0374
E- Fe_3O_4 volume	168.75	1	168.75	12.79	0.0374
F-$CaCl_2$ concentration	1752.08	1	1752.08	132.79	0.0014
G- $CaCl_2$ volume	168.75	1	168.75	12.79	0.0374
J-J	102.08	1	102.08	7.74	0.0689
Residual	39.58	3	13.19		
Cor Total	9422.92	11			

After that, all the Plackett-Burman design model runs were evaluated by considering the surface coverage amount of patterned bio-ink as the shape of the magnet, then, the response values were calculated between 0–100, as seen in Table 3.2. According to the Plackett-Burman design model, the mostly contributing parameters were determined as alginate (66.88%), $CaCl_2$ (18.59%), and MNP (4.97%) concentrations, as given in Table 3.3. According to the Plackett-Burman design model, the mostly contributing parameters were determined as alginate (66.88%), $CaCl_2$ (18.59%), and MNP (4.97%) concentrations, as given in Table 3.3. Total contribution of these parameters was calculated as 90.44 % while the other parameters had no significant effect on cell patterning. Also, that model was statistically analysed by ANOVA (Table 3.4), and the F value and p-value were found to be 88.89 and 0.0018 respectively. A p-value (Prob > F) of less than 0.05 indicates that model terms are significant. [173] In addition to F-value and p-value; R-Squared, Adj R-Squared, Pred R-Squared and Adeq Precision values were obtained as 0.9958, 0.9846, 0.9328 and 29.405 respectively. The Pred R-Squared was 0.9328 which means this model was reliable and it was in reasonable agreement with the Adj R-Squared of 0.9846. Moreover, value of adequate precision greater than 4 is desirable. In this model, it was obtained as 29.405 which indicated the signal was adequate.

After evaluating Plackett Burman design results, optimization parameters were decreased to 3; alginate, $CaCl_2$, and MNP concentrations, which were further evaluated by a 3-level factorial Box-Behnken design, as given in Table 3.5. The Box-Behnken Design resulted in 16 experiment runs with 4 replicates on the centre point by using 3 parameters, as seen in Table 3.6.

Table 3.5. Experimental parameters that were used in Box Behnken design.

Parameters	**Unit**	**Variable levels**		
		low	**moderate**	**high**
Alginate concentration	w/v %	0.08	0.9	0.1
Fe_3O_4 concentration	µg/ml	400	600	800
$CaCl_2$ concentration	mM	5	7.5	10

Table 3. 6. The Box-Behnken Design with 16 runs to obtain the optimum parameters (F: Factor, Alg: Alginate).

Run	F1: Alg. Concentration (w/v %)	F2: Fe_3O_4 concentration (µg/ml)	F3: $CaCl_2$ concentration (mM)
1	0.09	800	10
2	0.09	600	7.5
3	0.1	600	10
4	0.09	600	7.5
5	0.08	600	5
6	0.09	400	5
7	0.08	600	10
8	0.08	800	7.5
9	0.1	400	7.5
10	0.1	600	5
11	0.09	600	7.5
12	0.09	600	7.5
13	0.09	400	10
14	0.1	800	7.5
15	0.09	800	5
16	0.08	400	7.5

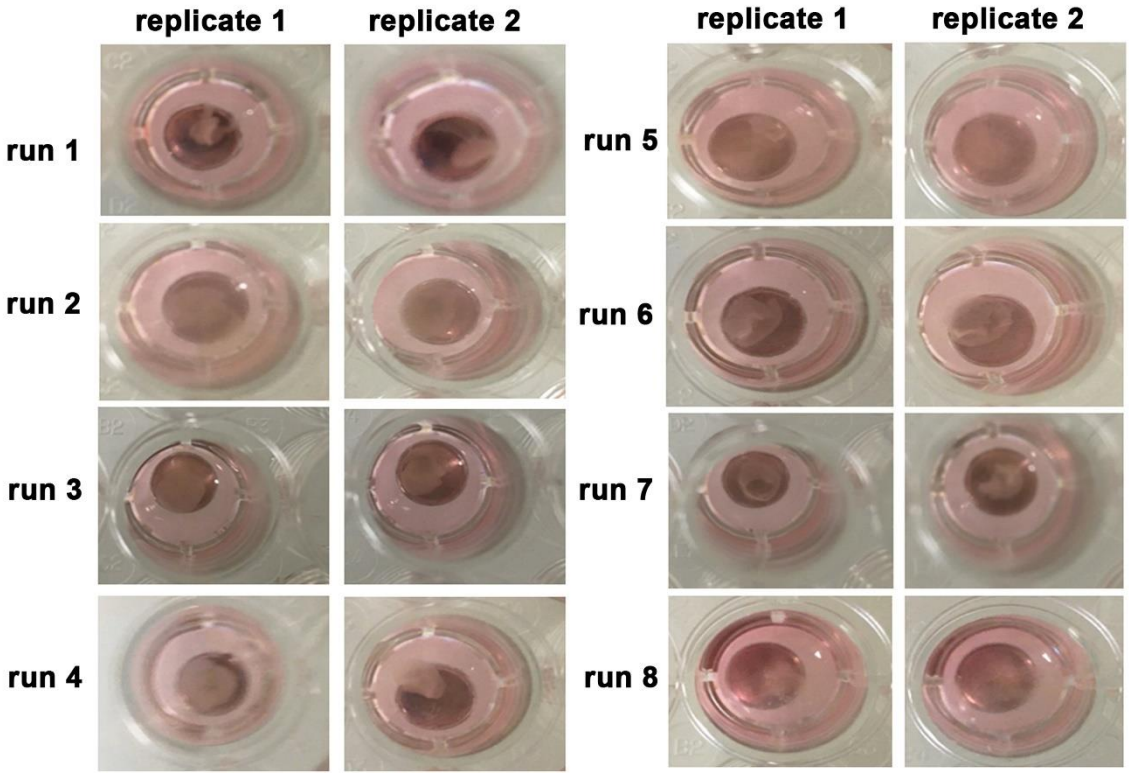

Figure 3. 38. Images of biopatterned bio-ink between run 1 and run 8.

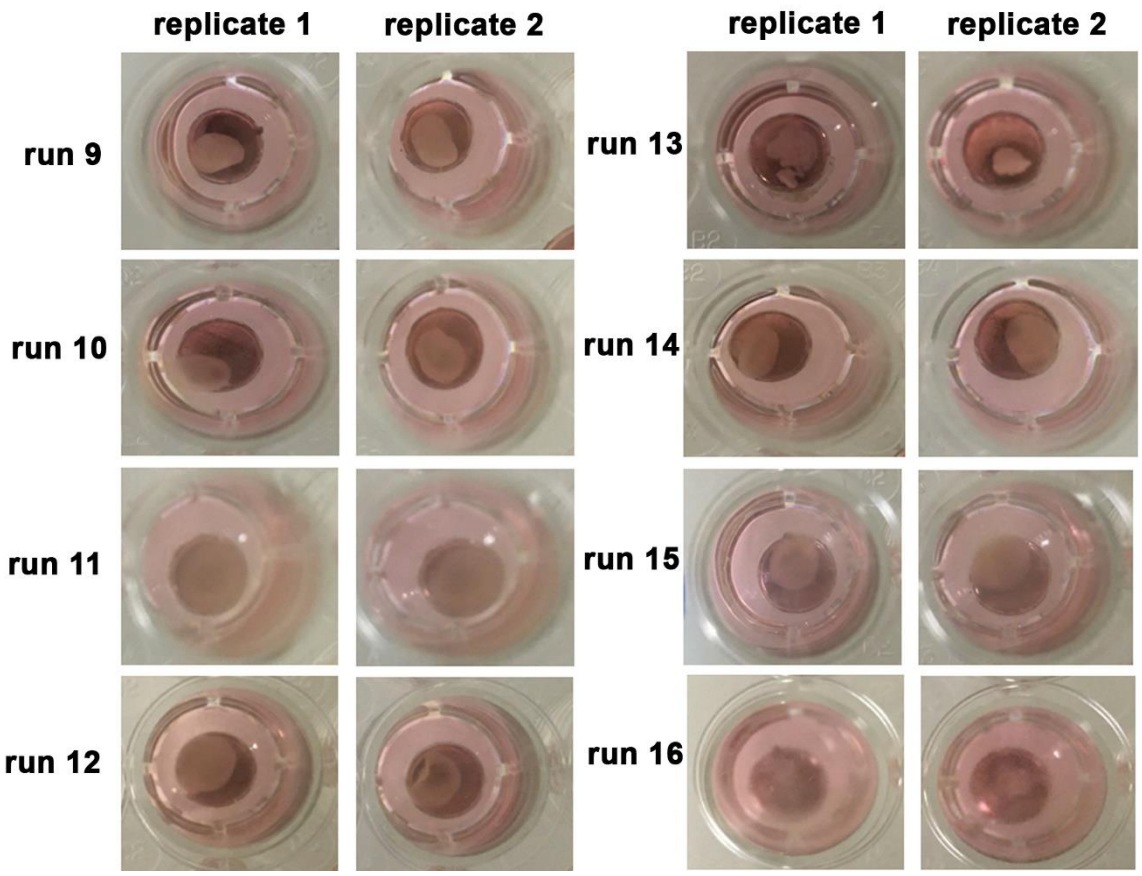

Figure 3. 39. Images of biopatterned bio-ink between run 9 and run 16.

Table 3.7. Response of cell patterning between 0-100 (F: Factor, Alg: Alginate, R: Response).

Run	**F1: Alg. Concentration (w/v %)**	**F2: Fe_3O_4 concentration (µg/ml)**	**F3: $CaCl_2$ concentration** (mM)	**R1: cell patterning**
1	0.09	800	10	0
2	0.09	600	7.5	50
3	0.1	600	10	50
4	0.09	600	7.5	40
5	0.08	600	5	90
6	0.09	400	5	20
7	0.08	600	10	10
8	0.08	800	7.5	20
9	0.1	400	7.5	30
10	0.1	600	5	30
11	0.09	600	7.5	60
12	0.09	600	7.5	40
13	0.09	400	10	10
14	0.1	800	7.5	30
15	0.09	800	5	50
16	0.08	400	7.5	0

Images of 16 runs are given in Figures 3.38 and 3.39. Box-Behnken model runs were evaluated by considering surface coverage of patterned bio-ink as the shape of the magnet, and then, the response values were calculated between 0–100 as shown Table 3.7. According to Box-Behnken design model cell biopatterning was fit to a second-order polynomial equation (Eq. 1);

$$\text{cell biopatterning} = +46.25 + 2.5A + 5B - 15C + 25AC - 26.25B^2 \qquad (1)$$

where A, B, and C are alginate, MNP and $CaCl_2$ concentrations respectively.

The F value and p-value of the model were found by the ANOVA to be 11.81 and 0.0006 respectively as shown in Table 3.8. This indicated that the model is significant ($p < 0.05$). The F value and p-value of lack of fit were obtained as 1.50 and 0.4013 which implies that lack of fit is not significant relative to the pure error. Non-significant lack of fit shows that results sufficiently fit the model. In addition to F-value and p-value; R-Squared, Adj R-Squared, Pred R-Squared and Adeq Precision values were obtained as 0.8552, 0.7827, 0.5473 and 12.294 respectively. The Pred R-Squared of 0.5473 is not as close with to the Adj R-Squared of 0.7827 as one might normally expect. Adeq Precision was obtained as 12.294 measures the signal to noise ratio and a ratio greater than 4 is desirable. It indicates an adequate signal in this model. Values of "p > F" less than 0.05 are considered as significant. Therefore, A, B, C, AC and B^2 are significant terms according to the Table 3.8.

Table 3.8. ANOVA for the Box Behnken design model.

Source	**Sum of Squares**	**df**	**Mean square**	**F value**	**p-value Prob>F**
Model	7306.25	5	1461.25	11.81	0.0006
A-Alginate concentration	50.00	1	50.00	0.40	0.5393
B-Fe_3O_4 concentration	200.00	1	200.00	1.62	0.2324
C-$CaCl_2$ concentration	1800.00	1	1800.00	14.55	0.0034
AC	2500.00	1	2500.00	20.20	0.0012
B^2	2756.25	1	2756.25	22.27	0.0008
Residual	1237.50	10	123.75		
Lack of Fit	962.50	7	137.50	1.50	0.4013
Pure Error	275.00	3	91.67		
Cor Total	8543.75	15			

As shown in Table 3.7, run 5 and 11 were scored the highest. Run 5 produced better patterning results compared to run 11 (Figure 3.40), which had higher concentrations of alginate (0.09%) and $CaCl_2$ (7.5 mM) that resulted in rapid gelation and random accumulation of bio-ink as explained previously. As a result, the optimized parameters of this model were decided as run 5 and these parameters were used for further studies. The parameter values of run 5 were 0.08% of alginate in 4 µl, 600 µg/ml of MNPs in 2 µl, 2×10^6 of NIH 3T3 cells in 4 µl, 5 mM of $CaCl_2$ concentration, 3 min of $CaCl_2$ incubation time, and 4 hr of bio-ink incubation time. Further cell culture studies and characterization were done based on these optimized parameters.

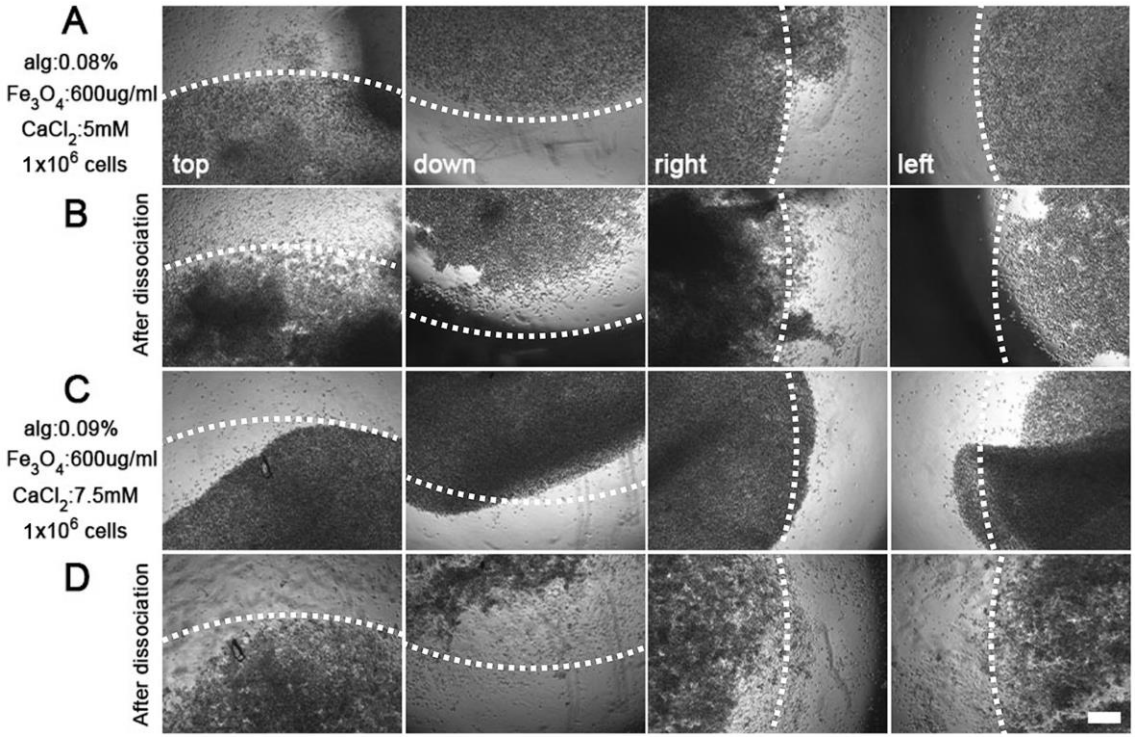

Figure 3.40. Light microscopy images of patterned cellular structures A) patterned bio-ink for run 5, B) patterned structures after disassociation of alginate for run 5, C) patterned bio-ink for run 11, D) patterned structures after disassociation of alginate for run 11. Scale bar: 200 µm.

3.2.2. Time-dependent Analysis of 3D Patterned Structures

The time-dependent behaviour of 3D patterned structures was investigated for long-term culture up to day 7, in terms of NIH/3T3 cell proliferation, migration, and viability. Time-dependent light microscopy images showed that cells proliferated and migrated towards well edges in increased culture time, as given in Figure 3.41. The borders of patterned structures were observed clearly for 3D cellular structures that were obtained after disassociation of alginate (t=0 h). At t=13 h, cells started to proliferate and migrate towards edges of the wells and the surface area of the patterned structure expanded. Migration behavior was investigated based on distances between patterned (i) and migrating cells (ii), which are indicated by white and red dashed lines, respectively. The relative migration distances of patterned structure were calculated to be 49, 68, and 100 % for 13, 72, and 120 h, respectively. Cell viability of patterned structures was investigated at 168 h by Live-Dead assay and high cell viability was observed indicating no diffusion limitations occurs for this model. Also, long-term cell viability (168 h) of patterned structures was investigated; 100 % for 3D and 98 % for 2D control were obtained by MTT assay (Figure 3.42), which supports the Live-Dead assay result.

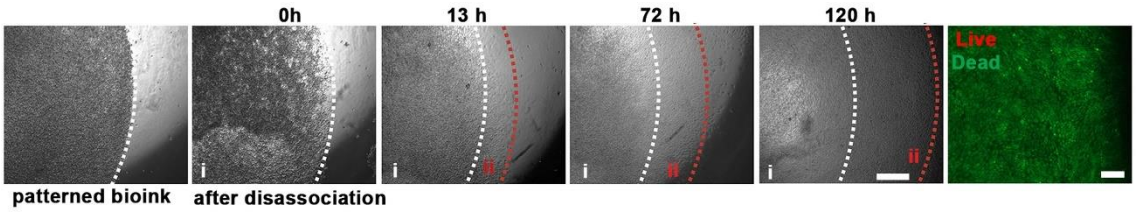

Figure 3.41. Light and Live/Dead assay images of time-dependent patterned 3D cellular structures. Scale bar: 200 µm.

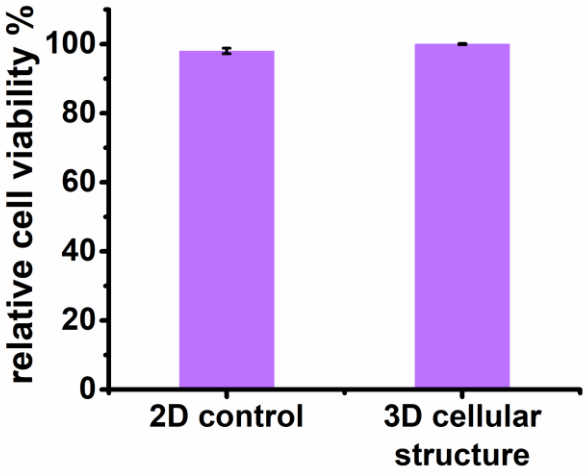

Figure 3.42. Relative cell viability % of disc-shaped patterned structures at day 7 obtained by the MTT assay.

3.2.3. Fabrication of 3D Cellular Structures by Different Magnet Shapes

Here, to investigate the applicability of the model in different formats and compatibility with different system components, the use of ring and rectangular magnets were evaluated. The patterned 3D cellular structure was obtained as the shape of the ring and rectangular with high cell adhesion after the disassociation of Ca-alginate, as shown in Figure 3.43 and 3.45. For the ring-shaped 3D cellular structure, cell proliferation and migration were observed at 48 hr and 168 hr. At the end of 48 hr, cells proliferated and migrated through the centre of the well, and ring closure with high cell viability was observed (Figure 3.43). At day 7, Live/Dead assays were performed to evaluate cell viability, and high cell viability was observed for the ring-shaped 3D cellular structure as shown in Figure 3.43, which fluorescent images for the different parts of the ring structure is given. In addition to the Live/Dead assay, relative cell viability was also evaluated by the MTT assay, and relative cell viability was obtained as 86% for ring-shaped 3D cellular structures, while 2D control was around 100% (Figure 3.44). As a result, cell proliferation and migration were observed for increased culture time with high cell viability. Moreover, patterned 3D cellular structures were obtained successfully, while using the rectangular magnet, as well as high cell adhesion

was obtained after the disassociation of alginate, as seen in Figure 3.45. Cell proliferation and migration were observed clearly at 72 hr and 168 hr culture times. As seen in Figure 3.45, high cell viability was observed at the 72 hr and 168 hr culture times for rectangular-shaped 3D cellular structures. In addition to the Live-dead assay, the MTT assay was performed to evaluate the relative cell viability of rectangular-shaped 3D cellular structures, which was obtained as 97%, while 2D control was 100%, as given in Figure 3.46. These results support that it is possible to modify bio-ink formulation to manipulate cells while using different magnet shapes. As a result, the viability, proliferation and migration behaviours of patterned 3D structures in long-term hold promise for the use of these models in drug screening applications.

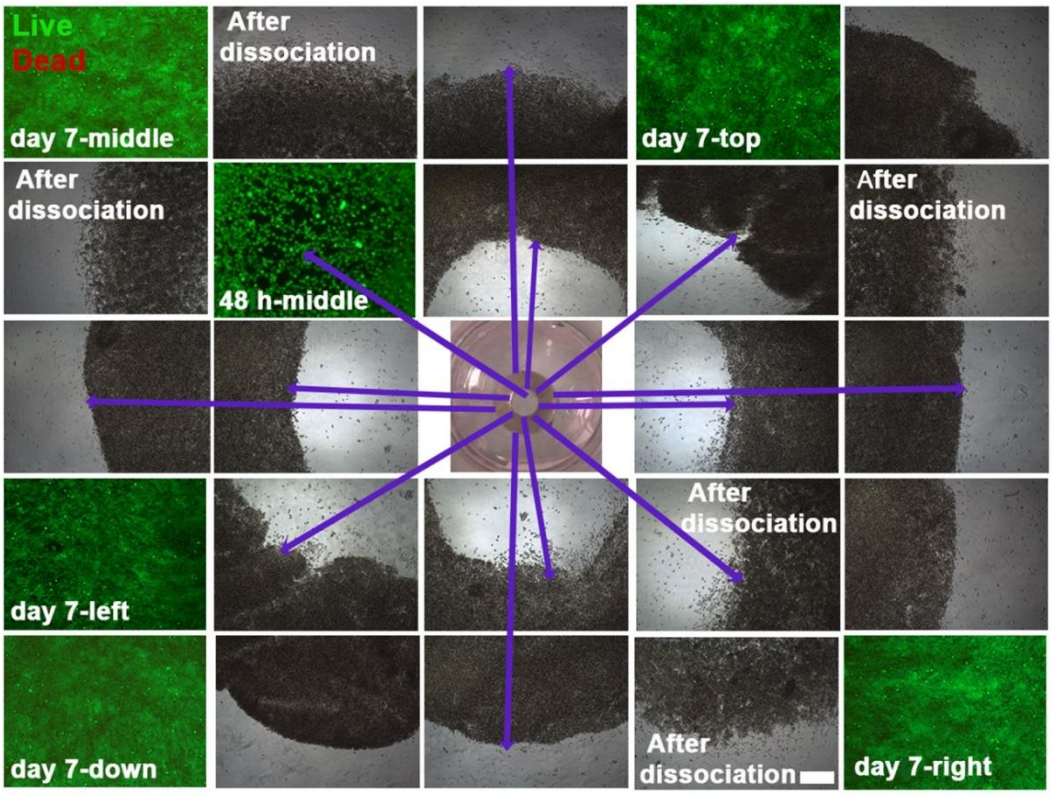

Figure 3.43. Light and fluorescent microscopy images of ring-shaped 3D cellular structures before and after the disassociation of alginate. Scale bar: 200 µm.

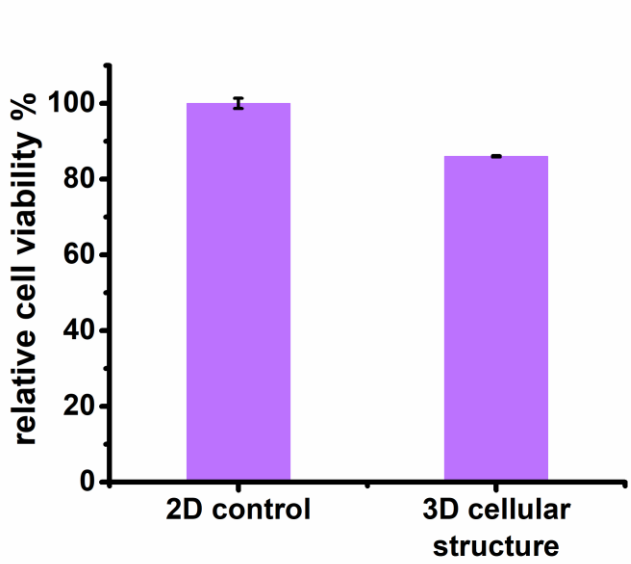

Figure 3.44. Relative cell viability % of ring-shaped patterned structures at day 7 obtained by the MTT assay.

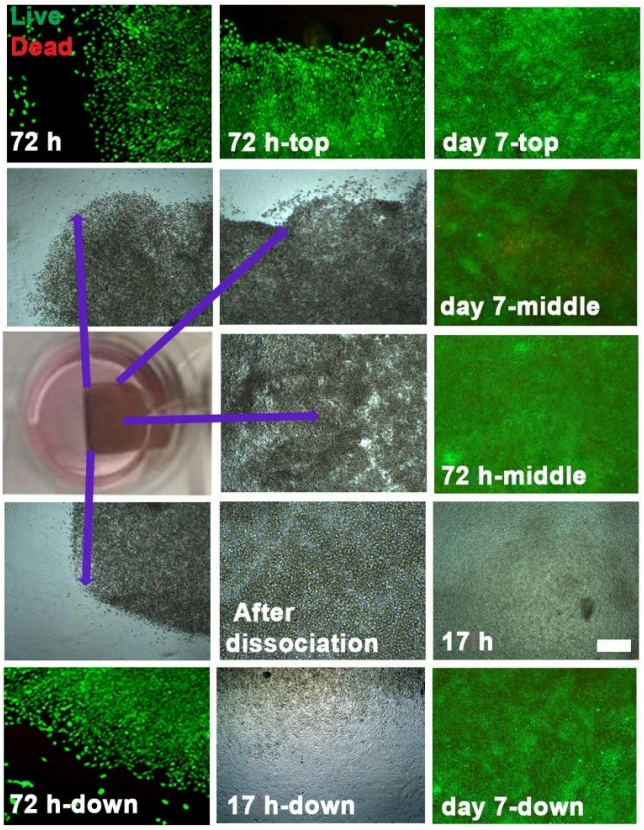

Figure 3.45. Relative cell viability % of rectangular-shaped patterned structures at day 7 obtained by the MTT assay.

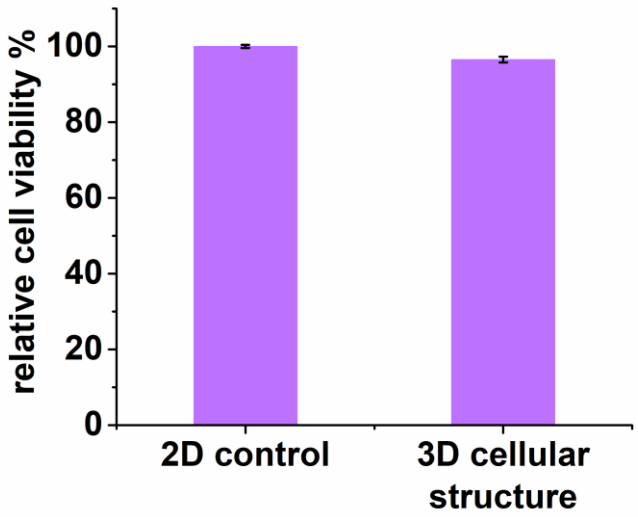

Figure 3.46. Light and fluorescent microscopy images of patterned cells before and after the disassociation of alginate for a rectangular-shaped magnet. Scale bar: 200 μm.

3.2.4. Characterization of Patterned 3D Cellular Structures

Cellular and extracellular components of 3D cellular structures for NIH/3T3 cells were investigated with immunostaining of collagen Type-I, F-actin, and DAPI staining. As given in Figure 3.47A, the nuclei of cells and actin filaments of 3D cellular structures were observed clearly. Cells proliferated and migrated towards edges of the well, and very dense 3D cellular structures were formed on day 7, as shown in Figure 3.47B. Collagen is one of the main components of ECM, therefore collagen secretion confirms formation of ECM. Very low collagen secretion was observed at day 1, which indicates 24 h culture time was not enough for collagen secretion for NIH/3T3 cells. The calculated fluorescence signal intensity of collagen I for day 7 was 23-fold higher, and fluorescence signal intensity of actin was 1.3-fold higher for day 7 compared to day 1.

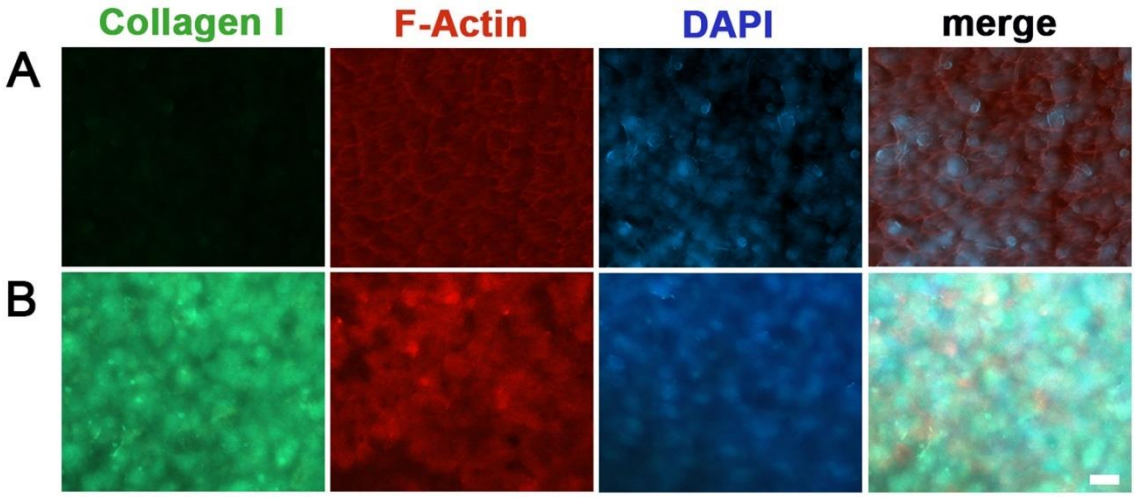

Figure 3.47. Immunofluorescent staining of patterned structures. A) day 1, B) day 7. Scale bar: 20 µm.

3.2.5. Biofabrication of 3D Cardiac Structures via Biopatterning Method

Fabrication of 3D cardiac cellular structures was carried out using H9c2 cardiomyocyte cells. Patterned H9c2 cells proliferated and migrated towards the centre of the ring structure and also towards the edges of the well as given in Figure 3.49. To evaluate cell viability, Live-Dead assay was done and high cell viability was observed (Figure 3.49). Moreover, relative cell viability was calculated as 80 % for 3D, and 100 % for 2D models via MTT assay (Figure 3.50). To obtain patterned 3D cardiac cellular structures with H9c2 cells, bio-ink incubation time increased to 24 hr while it was 4 hr for NIH/3T3 cells, which was related to the adhesion behaviour and adaptation ability and of cells to the 3D cell culture environment. Also, the relative cell viability % of NIH/3T3 3D cellular structures was obtained between 86–100%, compared to 2D control by using varied shapes of magnets. These differences in proliferation rates for 2D and 3D cell cultures related to the cell line and the type of 3D cell culture environment, which affects the adaptation time of cells. [174,175] The reason for different behaviours such as growth, proliferation, migration, and morphology in 2D and 3D cell culture is generally connected to the differential gene and/or protein expression. Cells in 2D cell culture proliferate more rapidly in comparison with the 3D cell culture model. However, cells in 2D cell culture lost their *in vivo* characteristics shortly. On the other

hand, cell adaptation in a 3D environment takes longer time, however it is important to preserve the transcriptional and translational functions at the *in vivo* level because, in the end, cells behave as they *in vivo*. [59] Here, ring-shape cardiac structure was fabricated to investigate cell migration towards center of wells as a parameter of drug toxicity. However, due to slow proliferation rate of H9c2 cells, evaluation of drug toxicity was done via MTT assay.

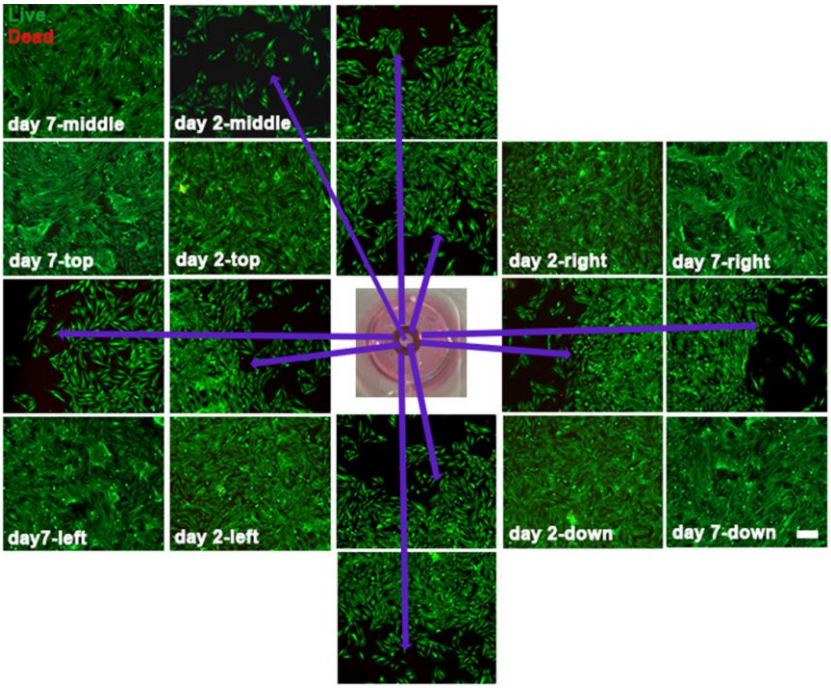

Figure 3.48. Fluorescent microscopy images of patterned 3D cardiac cellular structures at 7 day culture time. Scale bar: 200 µm.

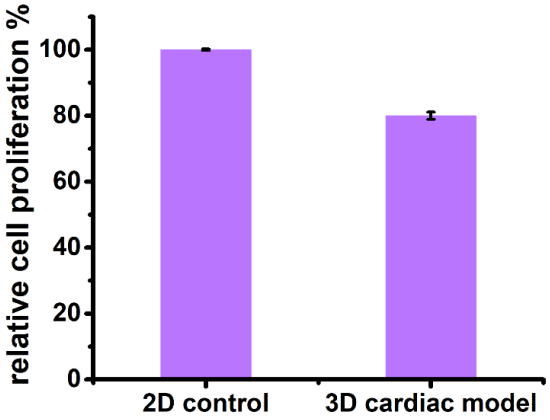

Figure 3.49. Relative cell proliferation of 3D cardiac model at 168h obtained by MTT.

Recently, a different approach for the manipulation and alignment of H9c2 cardiomyocyte cells in hydrogel by using a magnetic setup was developed. [176] For this aim, 3D-aligned patterning of H9c2 cells obtained magnetized cells using MNPs and based on the gel transition properties of Pluronic F-127 and fibrin hydrogels while applying an external magnetic field. They claim that this method had no harmful effect on cell metabolic activity and resulted in successful 3D-manipulated and -aligned cell organization which are correletes with our results in terms of cell viability.

Also, various 3D cardiac tissue models have been developed for drug screening and tissue regeneration studies using varied bio-ink formulations such as; GelMA/alginate,[177] GelMA hydrogel,[178] gelatine, [179] alginate/gelatine hydrogel, [180] and alginate/polyethylene glycol monoacrylate-fibrinogen. [181] Compared to other techniques like bio-printer, developed magnetic biopatterning methodology requires simple components, it is a cost-effective and user-friendly methodology.

3.2.6. Characterization of 3D Patterned Cardiac Structures

Cellular and extracellular components of 3D patterned H9c2 cells were investigated via immunostaining of collagen Type-I, F-actin, and DAPI staining for day 1 and day 7 as given in Figures 3.50A and 3.50B. Slight secretion of collagen was observed for patterned H9c2 cells on day 1 compared to NIH/3T3 cells, since adaptation of NIH/3T3 cells takes only 4 hr before disassociation while adaptation of H9c2 cells is

around 24 hr. As expected, fluorescence signal intensity of collagen I was 4.4-fold higher for day 7 (Figures 3.50B) compared to day 1 (Figures 3.50A), which indicates that collagen I secretion increased during long-term culture. In addition to cellular and extracellular component analysis, specific cardiac biomarkers were also investigated by immunostaining. Secretion of cardiac troponin T (Figure 3.51) and MYH6 (Figure 3.52) were observed clearly for both day 1 and day 7. Fluorescence signal intensity of cardiac troponin T and MYH6 were calculated as 1.8 and 1.2 fold higher for day 7 compared to day 1, respectively. Also, DAPI staining was done to visualize demonstrate the nuclei of cells.

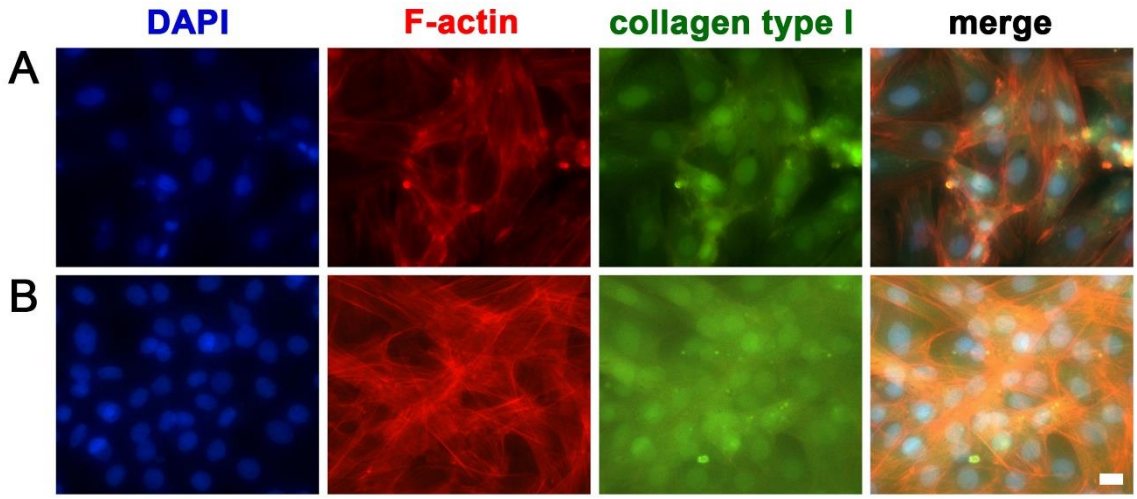

Figure 3.50. Immunofluorescent staining of patterned 3D cardiac structures. A) day 1, B) day 7. Scale bar: 20 µm.

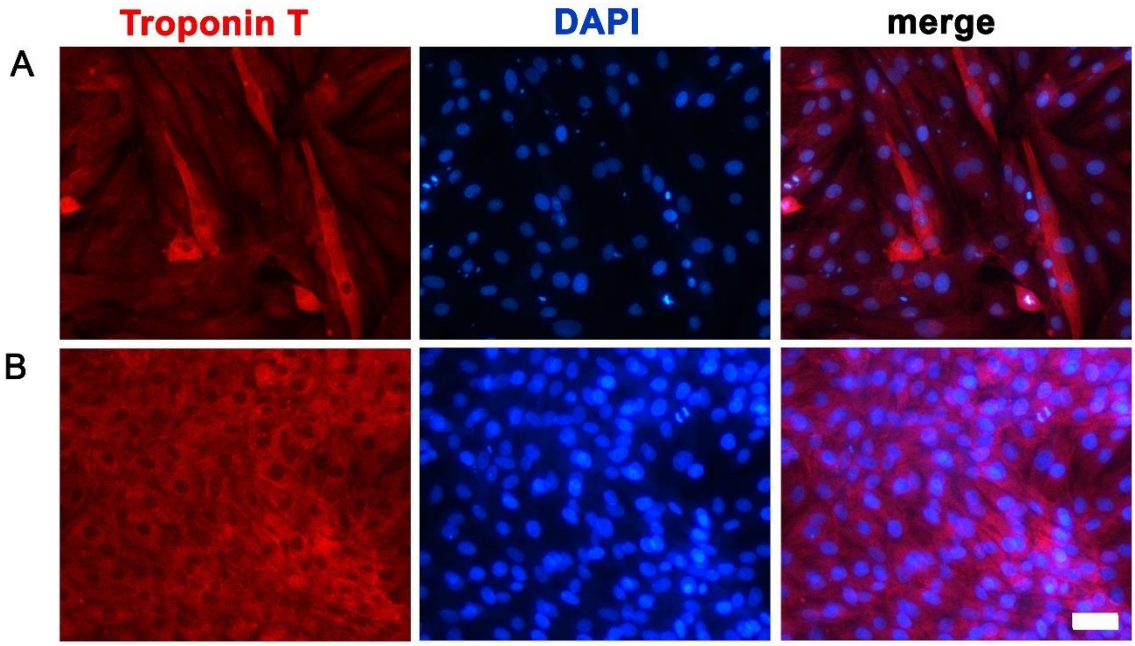

Figure 3.51. Immunofluorescence staining of 3D cardiac structures with cardiac Troponin T. A) Day 1, B) Day 7. Scale bar: 50 µm.

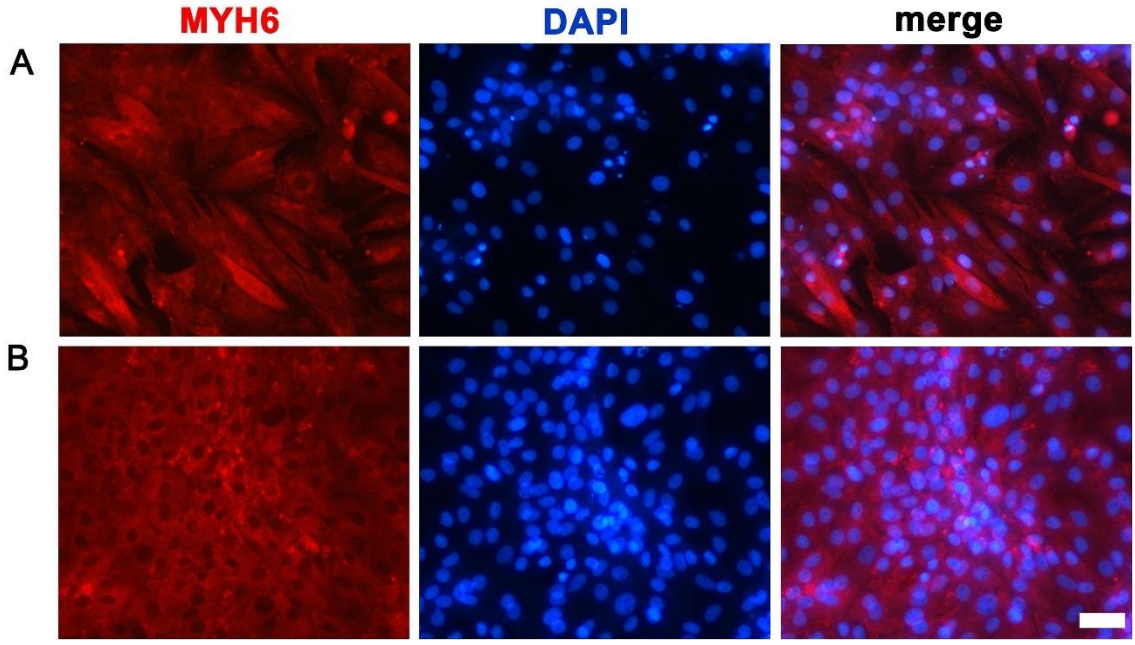

Figure 3.52. Immunofluorescence staining of 3D cardiac structures with MYH6 A) Day 1, B) Day 7. Scale bar: 50 µm.

3.2.7. Drug-Induced Cardiotoxicity Study

To evaluate drug response of 3D patterned cardiac structures, 0, 1, 5, 10, 25, and 50 µM of DOX was applied to them. Light microscopy images of DOX exposed patterned structures were given in Figures 3.53. Cell morphology was dramatically changed with 5 µM of DOX, and an enlarged nuclear area was observed due to a DOX-induced cardiotoxic effect. This phenomenon is known from literature where higher concentrations of DOX (5 and 10 µM) is used in cell culture an increased area of cell nuclei occurs. [52] Here, the dose-response curves of 2D control and 3D patterned structures were obtained by the MTT assay (Figure 3.54), and IC_{50} values were calculated as 3.5 and 8.1 µM, respectively. Also, the dose responses of patterned 3D cardiac cellular structures compared to 2D cell culture were significantly different according to t-test analysis ($p < 0.05$). In parallel to our previous findings, this results support that patterned 3D cardiac cellular structures are more resistant to drug exposure.

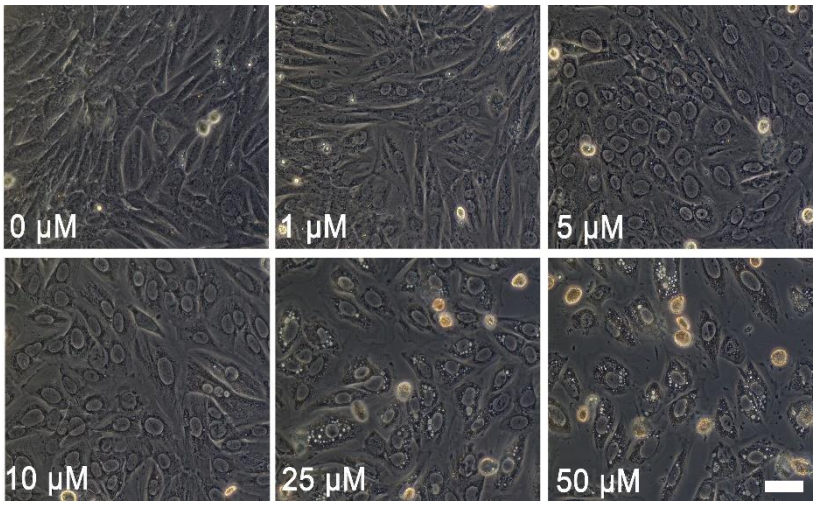

Figure 3.53. Light microscopy images of patterned 3D cardiac structures exposed varied DOX concentrations scale bar: 50 µm.

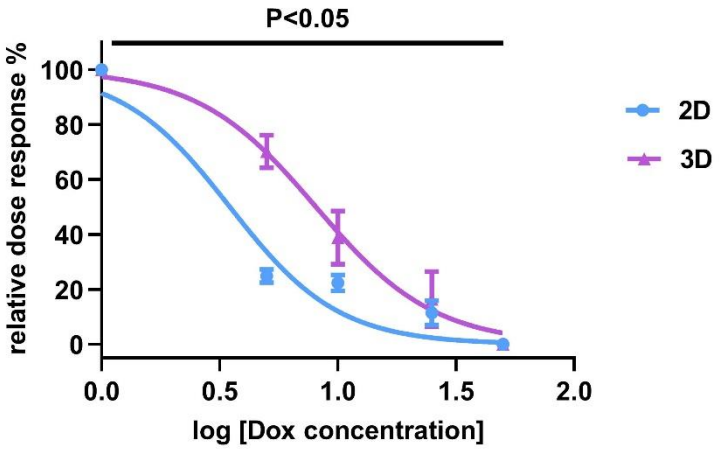

Figure 3.54. Relative dose-response % of 2D control and 3D cardiac cellular structures with fitted lines. Error bars represent the standard error of mean, p <0.05 compared to control.

3.2.8. Biofabrication of 3D Cardiac Model by Using hiPSC-derived Cardiomyocytes via Biopatterning Method

3.2.8.1. Optimization of Bio-ink Formulation and Biopatterning Parameters

Varied parameters were optimized such as cell number and bio-ink incubation time, to fabricate 3D cardiac model using hiPSC-derived cardiomyocytes via the biopatterning method because every cell line has a different characteristic.

The optimization of bio-ink incubation time, the disassociation step (citrate buffer) was applied at 24 hr culture time for 5 min as shown in Figure 3.55. However, cell clumping was observed in long term culture (day 9). Later, a citrate buffer was applied at 24h culture time for 10 min instead of 5 min as a disassociation step. However, cells were detached from the surface before 3D model forms, as shown in Figure 3.56. Further, the disassociation time was decreased to 20 hr, but still cells were detached (Figures 3.57).

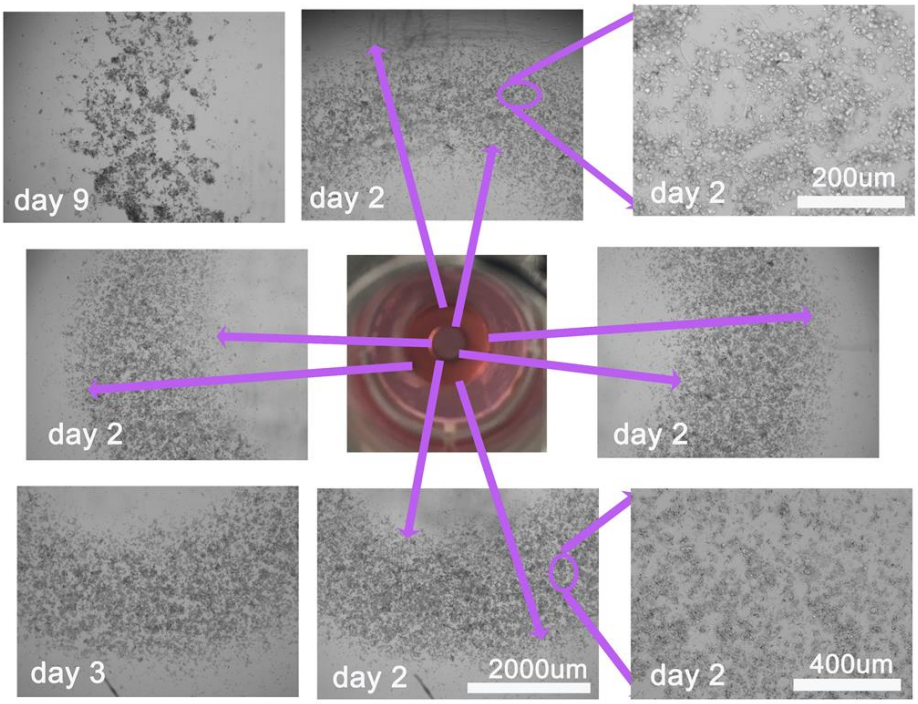

Figure 3.55. Light microscopy images of patterned cells in a ring shape after the disassociation of alginate (24 hr) at varied culture times.

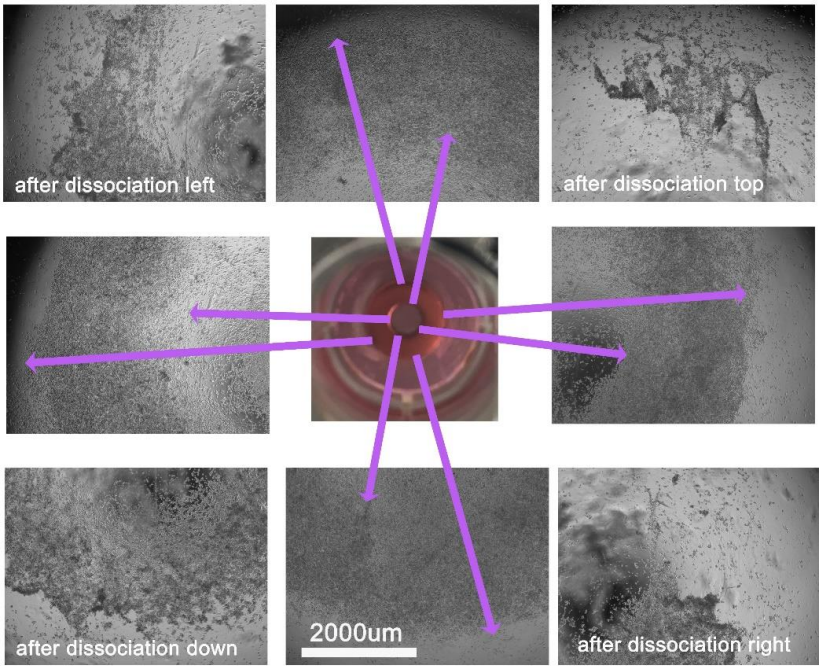

Figure 3.56. Light microscopy images of patterned cells in a ring shape at 24 hr culture time and citrate buffer applied for 10 min.

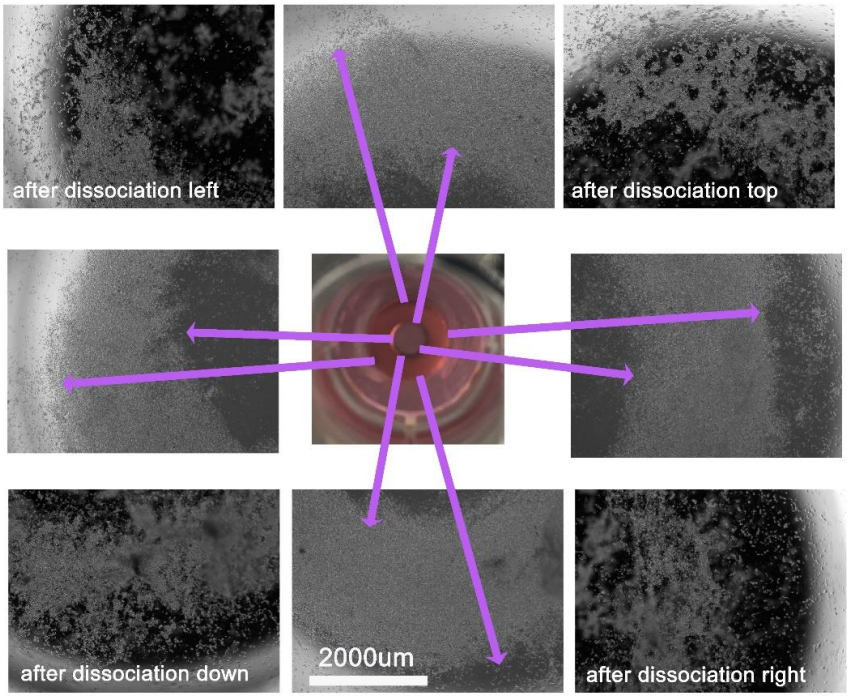

Figure 3.57. Light microscopy images of patterned cells in a ring shape after 20 hr culture time.

To overcome the cell clumping problem, alginate lyase was applied as the disassociation agent instead of a citrate buffer. Citrate buffer and alginate lyase have been used for the disassociation of alginate. However, they have different mechanisms of action. Alginate is degraded by alginate lyase through β-elimination of the glycosidic bond. [182] Alginate lyase was applied to one of the samples that had a cell number of 4×10^5 WTC cardiomyocytes for the disassociation of alginate for 5 min. As shown in Figure 3.58, dead cells were observed on top of the structure; however, cell clumping was not observed. For that reason, alginate lyase was decided to use as the disassociation agent.

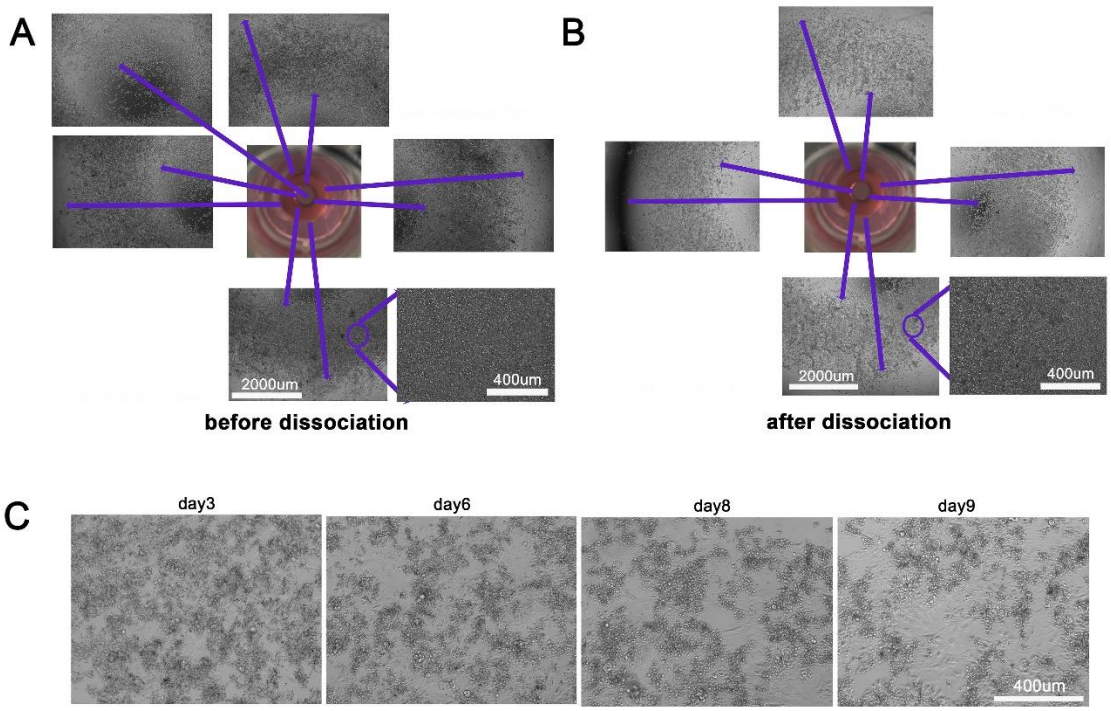

Figure 3.58. Light microscopy images of ring-shaped patterned WTC CMs. A) before disassociation, B) after disassociation, C) long-term cultured cellular structures.

For the further experiment, patterned cardiac structure was formed by using co-cultured WTC cardiomyocytes with 15 % cardiac fibroblast cells DRRAGN 3A1 (cFBs DRRAGN 3A1) while cell number was 6×10^5 to obtain more dense and more connected structure. Alginate lyase was applied for 15 min to disassociate the alginate. Compared to previous experiments more dense structure without clumping problem was obtained

as shown in Figures 3.59. Here, the interaction and communication of cardiomyocytes and cFBs affect the functioning of the tissue since the synthesis and degradation of many components of the extracellular matrix such as fibrin and collagen are done by cFBs. For that reason, the co-culture of cardiomyocytes with cFBs enhances cell-cell communication, and that results in the synchronized activity of cardiomyocytes. [183] Similar behaviour was reported using only iPSC-derived cardiomyocytes had some cracks or gaps within the tissue. It was overcome by addition of normal human cardiac fibroblasts into the tissues that made them denser. [29]

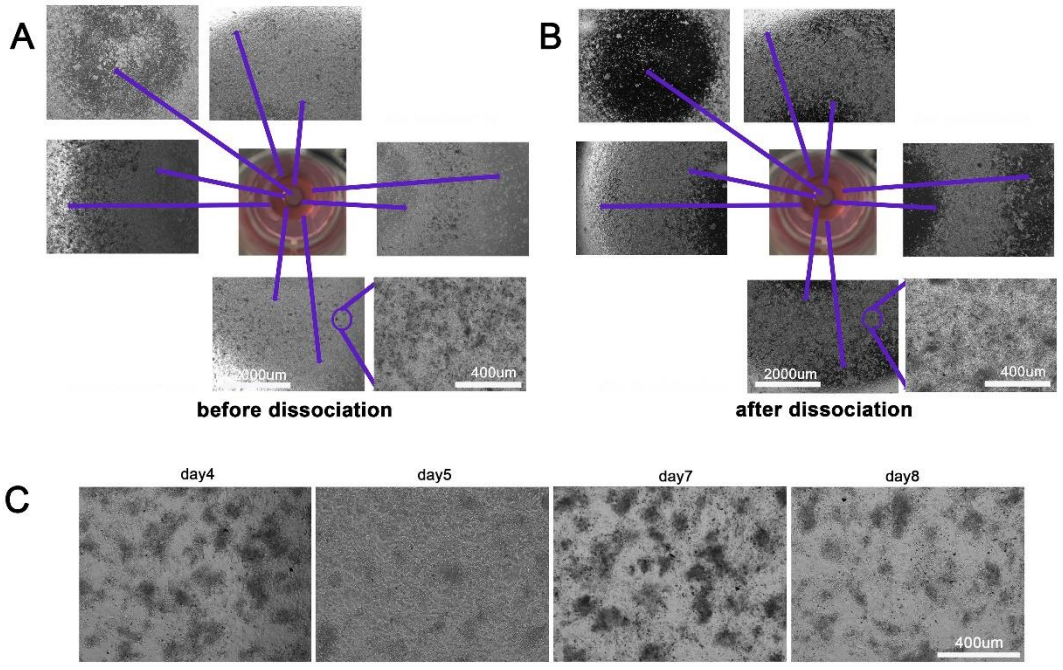

Figure 3.59. Light microscopy images of ring-shaped patterned WTC CMs with 15% cFBs. A) before disassociation, B) after disassociation, C) long-term cultured cardiac structures.

3.2.8.2. Cell viability and Characterization of 3D Patterned hiPSC-derived Cardiomyocytes

Live dead assay was done on patterned cardiac structures on day 13 to evaluate cell viability. High cell viability was observed for the patterned structure as given in Figure 3.60.

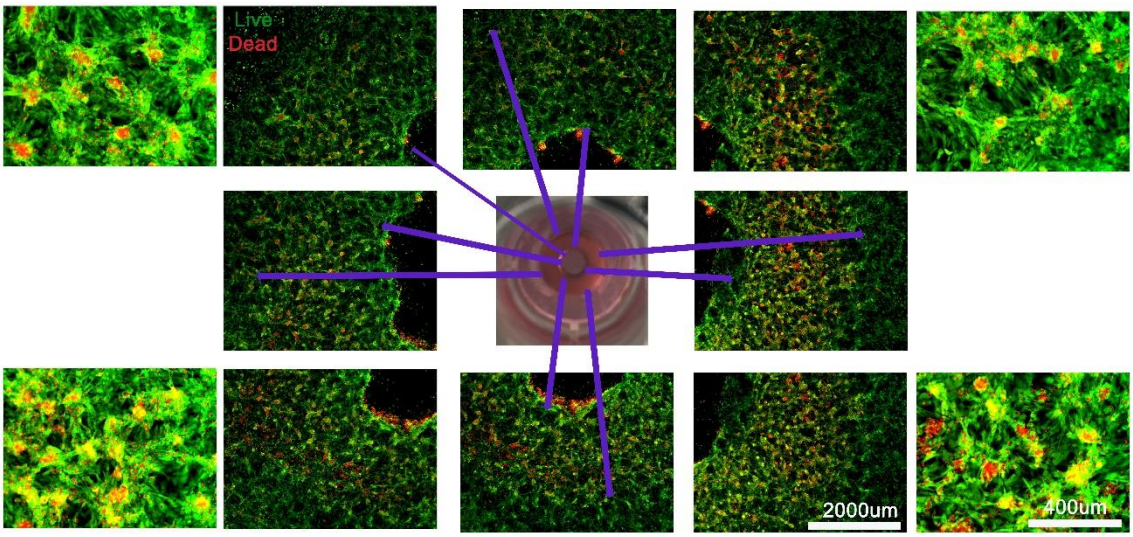

Figure 3. 60. Live dead assay images of patterned cardiac structures.

Characterization of patterned structures was carried out by applying, α-actinin, collagen I, Cx-43, Troponin T, and DAPI staining on day 13. Here, α-actinin indicated alignment of sarcomeres; Collagen I is the main component of the extracellular matrix and Cx-43 is a component of gap junctions which is associated with direct cell-cell communication gap junctions that are essential for the propagation of electrical depolarization in cardiomyocytes. Another marker investigated in this study is Troponin T, which is a cardiac regulatory protein that controls the calcium-mediated interaction between actin and myosin. These markers were observed clearly for patterned cardiac structures at day 13 as given in Figure 3.61.

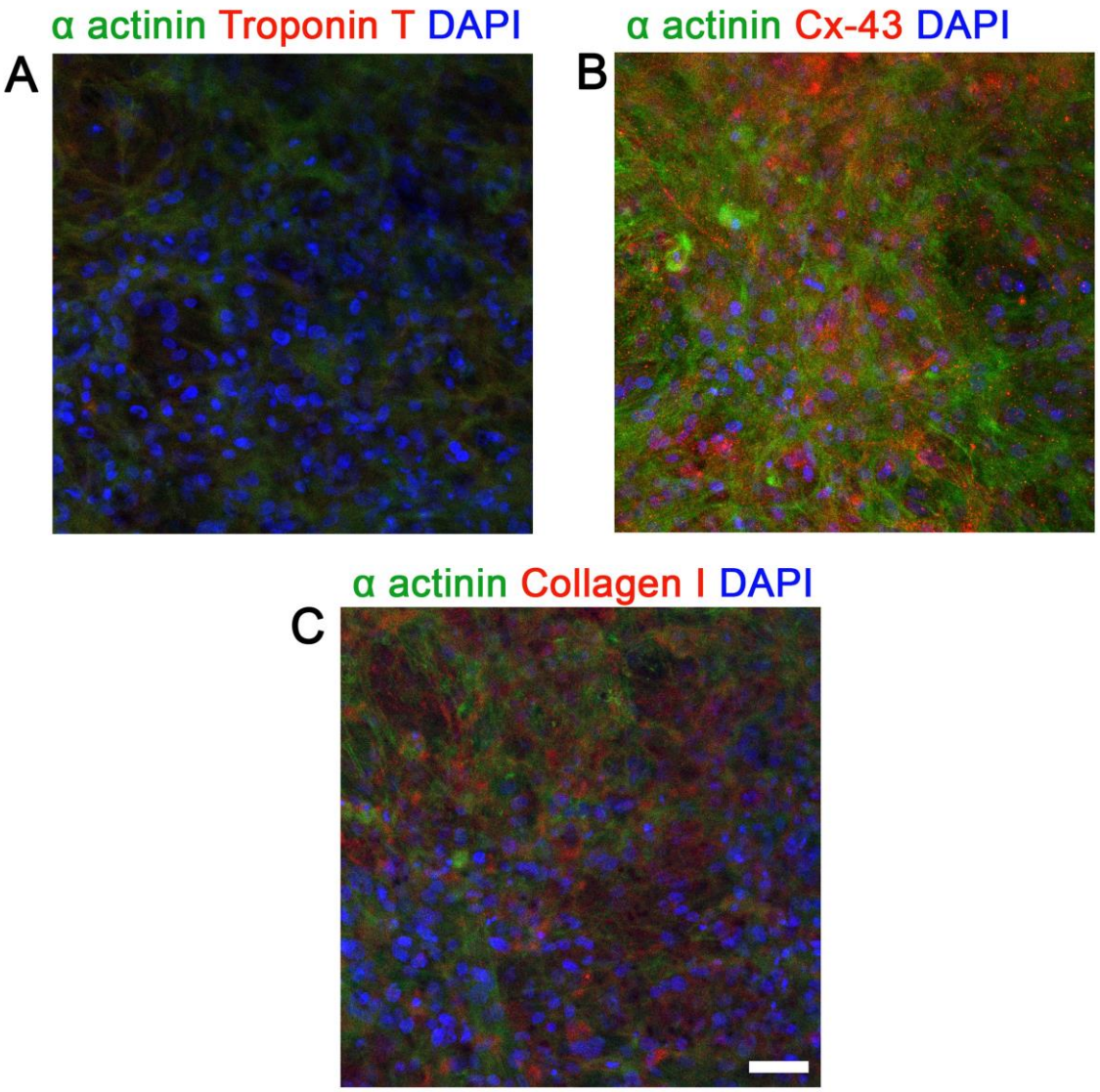

Figure 3.61. Immunostaining images of patterned cardiac structures A) α-actinin, Troponin T, and DAPI B) α-actinin, Cx-43, and DAPI C) α-actinin, collagen I, and DAPI scale bar: scale bar: 50 μm.

CHAPTER 4

CONCLUSION

The main purpose of this dissertation was to develop 3D cardiac models using contactless magnetic manipulation methodologies to use in tissue engineering applications, particularly for drug screening. For this aim, two contactless magnetic manipulation approaches; MagLev and biopatterning, were used.

In MagLev methodology, a new set-up was fabricated which had an 800 µl working volume that enabled changing medium easily and direct visualization was possible under the light microscopy. During the optimization steps, tunable spheroids, controllable spheroid size, area, circularity, and necrotic core formation, were obtained for NIH/3T3 cells by adjusting cell seeding numbers, Gx concentration, and culture time. Optimized parameters were obtained as 2.5×10^3 cells, 30 mM Gx, and 24 hr culture time while using 40×5 mm magnet (0.15 T). After optimization, cellular and extracellular components of spheroids; F-actin of cytoskeleton, collagen I of ECM and nucleus of cells were observed successfully for day 1 and day 7.

Moreover, 3D tumour models and co-culture models were obtained to demonstrate the applicability of the MagLev methodology for different applications. The spheroid morphology is directly affected by the cell type and their cellular adhesion molecules, but it can be also manipulated by changing culture parameters. Since the main aim of the thesis was to fabricate 3D cardiac models H9c2 cardiomyocyte cells were utilized for this purpose. Firstly, varied paramagnetic agents; Gadobutrol (Gx), Gadoteric acid (Dx), and Gadodiamide (Ox) were investigated in terms of their cytotoxic on H9c2 cells via Live-Dead and Alamar Blue Assays. The highest cell viability was obtained from Gx, which is connected to its slow dissociation of gadolinium ions. For that reason, Gx was used as a paramagnetic agent for further 3D cell culture studies. Cardiac spheroids were obtained after the optimization of parameters; which 2.5×10^3 cells, 10 mM Gx, 24 hr culture time and 40×5 mm magnet (0.15 T) were used for further culturing studies. Cellular and extracellular components; F-actin and collagen I were observed clearly for day 1 and day 5. Fluorescence signal intensity of collagen I and F-actin was 4.4-fold and 1.6-fold higher, respectively, for day

5 compared to day 1 which indicates that collagen I and F-actin secretion increased during long-term culture. Moreover, cardiac-specific markers; Troponin T and MYH6 were analyzed for both day 1 and day 5 that fluorescence signal intensity of cardiac troponin T and MYH6 were calculated as 1.9 and 1.2 fold higher for day 7, respectively. To investigate the drug response of cardiac spheroids, 0, 1, 5, 10, 25, and 50 µM DOX was applied. MTT assay was performed to evaluate DOX toxicity on cardiac spheroids and the intensity of formazan formation was analyzed. Increasing DOX concentrations led to lose structural integrity of cardiac spheroids and a decrease in viability. IC_{50} values were calculated as 3.5 and 14.7 µM for 2D standard control and 3D cardiac spheroids, respectively. These results supported that cardiac spheroids were more resistant to drug exposure and more reliable models for *in vitro* studies.

Another technique that was introduced to fabricate 3D cellular structures is biopatterning methodology. In this method, alginate-based bio-ink was formulated which consists of cells and MNP to fabricate 3D cellular structures. Optimization steps were completed using experimental design models; Plackett-Burman and Box-Behnken. Most effective parameters were obtained as alginate, $CaCl_2$, and MNP concentrations via the Plackett-Burman design model. Optimization was completed by using Box Behnken model, and patterned 3D cellular structures were obtained using NIH/3T3 cells as a model cell line. To investigate the applicability of bipatterning methodology, various shapes of 3D cellular structures were fabricated using disc, ring, and rectangular shape magnets. These biopatterned 3D cellular structures were cultured for 7 days and live-dead and MTT assays were used to evaluate cell viability. High cell viability was observed for all models and it was varying between 86 and 100 %. Moreover, secretion of collagen I and F-actin were investigated via immunostaining. Very low collagen secretion was observed at day 1, which indicates 24 h culture time was not enough for collagen secretion of NIH/3T3 cells. As expected, the calculated fluorescence signal intensity of collagen I for day 7 was 23-fold higher and the fluorescence signal intensity of actin was 1.3-fold higher for day 7 compared to day 1. After that, 3D cardiac models using H9c2 rat cardiomyocytes were fabricated by using biopatterning methodology. High cell viability was observed by Live-Dead assay, and also relative cell viability was calculated as 80 % for 3D, and 100 % for 2D models via MTT assay. Moreover, to indicate their cellular and extracellular components, including cardiac-specific markers, immunostaining was applied, and accordingly collagen I, F-actin, cardiac troponin T, and MYH6 were successfully observed. Fluorescence signal intensity of cardiac

troponin T and MYH6 were calculated as 1.9 and 1.2 fold higher for day 7, respectively. Finally, 1, 5, 10, 25, and 50 μM DOX was applied and dose response of 3D patterned cardiac structures, and 2D controls were evaluated by the MTT assay. Furthermore, IC50 values were obtained as 8.1 μM for 3D cardiac structures, while standard 2D control was 3.5 μM. 3D cardiac models showed more resistance to DOX exposure compared to standard 2D cell culture.

In the last part of thesis, patterned cardiac structures were fabricated using hiPSC-derived cardiomyocytes via biopatterning methodology. 3D patterned cardiac structures were obtained with recently optimized parameters. However, cell clumping problem occurred in long-term cell culture. To overcome this obstacle, co-culturing of WTC cardiomyocytes with 15 % fibroblast cells and applying alginate lyase as a disassociation agent was done. After that, live-dead assay was used to evaluate cell viability and high cell viability was observed for 3D patterned cardiac model. Characterization was carried out by immunostaining of α-actinin, collagen I, Cx-43, Troponin T, and DAPI staining.

MagLev and magnetic biopatterning methodologies were utilized to biofabricate 3D spheroids and patterned 3D cellular structures for drug screening studies. In the MagLev method, low cell number was used to fabricate spheroids and small compact structures were obtained using both NIH/3T3 and H9c2 cells. On the other hand, some of the cancer cell lines; MDA-MB 231 and PC-12 resulted in formation of loose spheroid structures. These results are not only related to the parameters of methodology but also related to specific cellular adhesion molecules of cell lines. In the other developed method, which is biopatterning technique, high cell number was needed to fabricate 3D cellular structures. Also, it is a biomaterial-based technique even the alginate was disassociated and removed from the microenvironment, cells needed some adaptation time. Taken together, these methodologies require simple components and offer rapid, cost-effective, and user-friendly biofabrication methods. Moreover, 3D cardiac models were obtained functionally considering their immunostaining and drug response results. That means these developed contactless magnetic manipulation methodologies would be good alternative approaches for functionality and drug screening studies.

Further, patterned cardiac structures obtained using co-cultured hiPSC-derived cardiomyocytes with cardiac fibroblast were fabricated succesfully. As a future perspective; they could be used for drug screening of cardiotoxic drugs like DOX or

could be used as a 3D arrhythmic model. Moreover, to obtain a more realistic cardiac model, hiPSC-derived cardiomyocytes could be co-cultured with fibroblast and endothelial cells because nitric oxide (NO) released from the endothelial cells protects cardiomyocytes against DOX-induced cardiotoxicity. Therefore, the cell ratios in cardiac structures that comprise endothelial cells and fibroblasts are important for evaluating responses to DOX since cross-talk between different cell types contributes to mediating the response of cardiotoxicity. [40] Also, hiPSC-derived cardiomyocytes could be cultured with fibroblast and endothelial cells to fabricate cardiac spheroids via MagLev methododogy to evaluate drug response and that would be an important contribution to the literature to compare the current results.

REFERENCES

(1) Langer, R.; Vacanti, J. P. *Tissue Engineering*. www.sciencemag.org.

(2) Stock, U. A.; Vacanti, J. P. Tissue Engineering: Current State and Prospects. *Annu. Rev. Med.* **2001**, *52*, 443–451. https://doi.org/10.1146/annurev.med.52.1.443.

(3) Bonassar, L. J.; Vacanti, C. A. Tissue Engineering: The First Decade and Beyond. *J. Cell. Biochem. Suppls* **1998**, *30*, 297–303. https://doi.org/10.1002/(SICI)1097-4644(1998)72:30/31.

(4) Lavik, E.; Langer, R. Tissue Engineering: Current State and Perspectives. *Applied Microbiology and Biotechnology 2004 65:1* **2004**, *65* (1), 1–8. https://doi.org/10.1007/S00253-004-1580-Z.

(5) Cao, Y.; Croll, T. I.; Lees, J. G.; Tuch, B. E.; Cooper-White, J. J.; Cao, Y.; Croll, T. I.; Lees, J. G.; Tuch, B. E.; Cooper-White, J. J. Scaffolds, Stem Cells, and Tissue Engineering: A Potent Combination! *Aust J Chem* **2005**, *58* (10), 691–703. https://doi.org/10.1071/CH05145.

(6) Vasita, R.; Shanmugam, K.; Katti, D. S. *Improved Biomaterials for Tissue Engineering Applications: Surface Modification of Polymers*; 2008; Vol. 8.

(7) Daley, W. P.; Peters, S. B.; Larsen, M. Extracellular Matrix Dynamics in Development and Regenerative Medicine. *J Cell Sci* **2008**, *121* (3), 255–264. https://doi.org/10.1242/jcs.006064.

(8) Rosso, F.; Giordano, A.; Barbarisi, M.; Barbarisi, A. From Cell-ECM Interactions to Tissue Engineering. *J Cell Physiol* **2004**, *199* (2), 174–180. https://doi.org/10.1002/JCP.10471.

(9) Labat-Robert, J.; Bihari-Varga, M.; Robert, L. Extracellular Matrix. *FEBS Lett* **1990**, *268* (2), 386–393. https://doi.org/10.1016/0014-5793(90)81291-U.

(10) *An Introduction to Tissue-Biomaterial Interactions | Wiley*. https://www.wiley.com/en-

us/An+Introduction+to+Tissue+Biomaterial+Interactions-p-9780471253945 (accessed 2022-07-31).

(11) DuRaine, G. D.; Brown, W. E.; Hu, J. C.; Athanasiou, K. A. Emergence of Scaffold-Free Approaches for Tissue Engineering Musculoskeletal Cartilages. *Ann Biomed Eng* **2014**, *43* (3), 543–554. https://doi.org/10.1007/S10439-014-1161-Y.

(12) Athanasiou, K. A.; Eswaramoorthy, R.; Hadidi, P.; Hu, J. C. Self-Organization and the Self-Assembling Process in Tissue Engineering. *Annu Rev Biomed Eng* **2013**, *15*, 115–136. https://doi.org/10.1146/ANNUREV-BIOENG-071812-152423.

(13) Lee, J. K.; Link, J. M.; Hu, J. C. Y.; Athanasiou, K. A. The Self-Assembling Process and Applications in Tissue Engineering. *Cold Spring Harb Perspect Med* **2017**, *7* (11). https://doi.org/10.1101/CSHPERSPECT.A025668.

(14) Eschenhagen, T.; Eder, A.; Vollert, I.; Hansen, A. Physiological Aspects of Cardiac Tissue Engineering. *Am J Physiol Heart Circ Physiol* **2012**, *303* (2), 133–143. https://doi.org/10.1152/AJPHEART.00007.2012/SUPPL_FILE/PODCAST.MP3.

(15) Chiu, L. L. Y.; Iyer, R. K.; Reis, L. A.; Nunes, S. S.; Radisic, M. Cardiac Tissue Engineering: Current State and Perspectives. *Frontiers in Bioscience* **2012**, *17* (4), 1533–1550. https://doi.org/10.2741/4002/PDF.

(16) Curtis, M. W.; Russell, B. Cardiac Tissue Engineering. *J Cardiovasc Nurs* **2009**, *24* (2), 87. https://doi.org/10.1097/01.JCN.0000343562.06614.49.

(17) Baillargeon, B.; Rebelo, N.; Fox, D. D.; Taylor, R. L.; Kuhl, E. The Living Heart Project: A Robust and Integrative Simulator for Human Heart Function. *European Journal of Mechanics - A/Solids* **2014**, *48* (1), 38–47. https://doi.org/10.1016/J.EUROMECHSOL.2014.04.001.

(18) MacDonald, E. A.; Rose, R. A.; Quinn, T. A. Neurohumoral Control of Sinoatrial Node Activity and Heart Rate: Insight From Experimental Models and Findings From Humans. *Front Physiol* **2020**, *11*, 170. https://doi.org/10.3389/FPHYS.2020.00170/BIBTEX.

(19) Kurokawa, Y. K.; George, S. C. Tissue Engineering the Cardiac Microenvironment: Multicellular Microphysiological Systems for Drug Screening. *Adv Drug Deliv Rev* **2016**, *96*, 225. https://doi.org/10.1016/J.ADDR.2015.07.004.

(20) Zhou, P.; Pu, W. T. Recounting Cardiac Cellular Composition. *Circ Res* **2016**, *118* (3), 368. https://doi.org/10.1161/CIRCRESAHA.116.308139.

(21) Perbellini, F.; Watson, S. A.; Bardi, I.; Terracciano, C. M. Heterocellularity and Cellular Cross-Talk in the Cardiovascular System. *Front Cardiovasc Med* **2018**, *5*, 143. https://doi.org/10.3389/FCVM.2018.00143.

(22) Parker, K. K.; Ingber, D. E. Extracellular Matrix, Mechanotransduction and Structural Hierarchies in Heart Tissue Engineering. *Philosophical Transactions of the Royal Society B: Biological Sciences* **2007**, *362* (1484), 1267. https://doi.org/10.1098/RSTB.2007.2114.

(23) Li, Z.; Guan, J. Hydrogels for Cardiac Tissue Engineering. *Polymers 2011, Vol. 3, Pages 740-761* **2011**, *3* (2), 740–761. https://doi.org/10.3390/POLYM3020740.

(24) Immohr, M. B.; dos Santos Adrego, F.; Teichert, H. L.; Schmidt, V.; Sugimura, Y.; Bauer, S.; Barth, M.; Lichtenberg, A.; Akhyari, P. 3D-Bioprinting of Aortic Valve Interstitial Cells: Impact of Hydrogel and Printing Parameters on Cell Viability. *Biomedical Materials* **2023**, *18* (1), 015004. https://doi.org/10.1088/1748-605x/ac9f91.

(25) Wu, Z.; Li, W.; Cheng, S.; Liu, J.; Wang, S. Novel Fabrication of Bioengineered Injectable Chitosan Hydrogel Loaded with Conductive Nanoparticles to Improve Therapeutic Potential of Mesenchymal Stem Cells in Functional Recovery after Ischemic Myocardial Infarction. *Nanomedicine* **2023**, *47*, 102616. https://doi.org/10.1016/j.nano.2022.102616.

(26) Moroni, F.; Mirabella, T. Decellularized Matrices for Cardiovascular Tissue Engineering. *Am J Stem Cells* **2014**, *3* (1), 1.

(27) Arai, K.; Kitsuka, T.; Nakayama, K. Scaffold-Based and Scaffold-Free Cardiac Constructs for Drug Testing. *Biofabrication*. IOP Publishing Ltd October 1, 2021. https://doi.org/10.1088/1758-5090/ac1257.

(28) Barbulescu, G. I.; Bojin, F. M.; Ordodi, V. L.; Goje, I. D.; Barbulescu, A. S.; Paunescu, V. Decellularized Extracellular Matrix Scaffolds for Cardiovascular Tissue Engineering: Current Techniques and Challenges. *Int J Mol Sci* **2022**, *23* (21), 13040. https://doi.org/10.3390/ijms232113040.

(29) Amano, Y.; Nishiguchi, A.; Matsusaki, M.; Iseoka, H.; Miyagawa, S.; Sawa, Y.; Seo, M.; Yamaguchi, T.; Akashi, M. Development of Vascularized IPSC Derived 3D-Cardiomyocyte Tissues by Filtration Layer-by-Layer Technique and Their Application for Pharmaceutical Assays. *Acta Biomater* **2016**, *33*, 110–121. https://doi.org/10.1016/j.actbio.2016.01.033.

(30) Chen, Y.; Chan, J. P. Y.; Wu, J.; Li, R. K.; Santerre, J. P. Compatibility and Function of Human Induced Pluripotent Stem Cell Derived Cardiomyocytes on an Electrospun Nanofibrous Scaffold, Generated from an Ionomeric Polyurethane Composite. *J Biomed Mater Res A* **2022**, *110* (12), 1932–1943. https://doi.org/10.1002/jbm.a.37428.

(31) Arai, K.; Murata, D.; Takao, S.; Nakamura, A.; Itoh, M.; Kitsuka, T.; Nakayama, K. Drug Response Analysis for Scaffold-Free Cardiac Constructs Fabricated Using Bio-3D Printer. *Sci Rep* **2020**, *10* (1). https://doi.org/10.1038/s41598-020-65681-y.

(32) Döhrmann, M.; Schorr, A.; Hülsenbeck, J.; Rasmussen, T. L.; Issinger, O. G.; Fritz, G. Comparative Analysis of Stress Responses of H9c2 Rat Cardiomyoblasts Following Treatment with Doxorubicin and TBOOH. *Exp Cell Res* **2012**, *318* (6), 779–788. https://doi.org/10.1016/J.YEXCR.2012.01.010.

(33) Lenčo, J.; Lenčová-Popelová, O.; Link, M.; Jirkovská, A.; Tambor, V.; Potůčková, E.; Stulík, J.; Šimůnek, T.; Štěrba, M. Proteomic Investigation of Embryonic Rat Heart-Derived H9c2 Cell Line Sheds New Light on the Molecular Phenotype of the Popular Cell Model. *Exp Cell Res* **2015**, *339* (2), 174–186. https://doi.org/10.1016/J.YEXCR.2015.10.020.

(34) Watkins, S. J.; Borthwick, G. M.; Arthur, H. M. The H9C2 Cell Line and Primary Neonatal Cardiomyocyte Cells Show Similar Hypertrophic Responses in Vitro. *In Vitro Cell Dev Biol Anim* **2011**, *47* (2), 125–131. https://doi.org/10.1007/S11626-010-9368-1.

(35) Witek, P.; Korga, A.; Burdan, F.; Ostrowska, M.; Nosowska, B.; Iwan, M.; Dudka, J. The Effect of a Number of H9C2 Rat Cardiomyocytes Passage on Repeatability of Cytotoxicity Study Results. *Cytotechnology* **2016**, *68* (6), 2407–2415. https://doi.org/10.1007/S10616-016-9957-2/FIGURES/7.

(36) Lou, Y.; Wang, Z.; Xu, Y.; Zhou, P.; Cao, J.; Li, Y.; Chen, Y.; Sun, J.; Fu, L. Resveratrol Prevents Doxorubicin-Induced Cardiotoxicity in H9c2 Cells through the Inhibition of Endoplasmic Reticulum Stress and the Activation of the Sirt1 Pathway. *Int J Mol Med* **2015**, *36* (3), 873–880. https://doi.org/10.3892/IJMM.2015.2291/HTML.

(37) Branco, A. F.; Pereira, S. P.; Gonzalez, S.; Gusev, O.; Rizvanov, A. A.; Oliveira, P. J. Gene Expression Profiling of H9c2 Myoblast Differentiation towards a Cardiac-Like Phenotype. *PLoS One* **2015**, *10* (6), e0129303. https://doi.org/10.1371/JOURNAL.PONE.0129303.

(38) Budharaju, H.; Subramanian, A.; Sethuraman, S. Recent Advancements in Cardiovascular Bioprinting and Bioprinted Cardiac Constructs. *Biomaterials Science*. Royal Society of Chemistry March 21, 2021, pp 1974–1994. https://doi.org/10.1039/d0bm01428a.

(39) Beqqali, A.; van Eldik, W.; Mummery, C.; Passier, R. Review Human Stem Cells as a Model for Cardiac Differentiation and Disease. https://doi.org/10.1007/s00018-009-8476-0.

(40) Arai, K.; Kitsuka, T.; Nakayama, K. Scaffold-Based and Scaffold-Free Cardiac Constructs for Drug Testing. *Biofabrication* **2021**, *13* (4), 042001. https://doi.org/10.1088/1758-5090/AC1257.

(41) Wnorowski, A.; Sharma, A.; Chen, H.; Wu, H.; Shao, N. Y.; Sayed, N.; Liu, C.; Countryman, S.; Stodieck, L. S.; Rubins, K. H.; Wu, S. M.; Lee, P. H. U.; Wu, J. C. Effects of Spaceflight on Human Induced Pluripotent Stem Cell-Derived Cardiomyocyte Structure and Function. *Stem Cell Reports* **2019**, *13* (6), 960–969. https://doi.org/10.1016/J.STEMCR.2019.10.006.

(42) Karakikes, I.; Ameen, M.; Termglinchan, V.; Wu, J. C. Human Induced Pluripotent Stem Cell-Derived Cardiomyocytes: Insights into Molecular,

Cellular, and Functional Phenotypes. *Circ Res* **2015**, *117* (1), 80–88. https://doi.org/10.1161/CIRCRESAHA.117.305365.

(43) Braam, S. R.; Passier, R.; Mummery, C. L. Cardiomyocytes from Human Pluripotent Stem Cells in Regenerative Medicine and Drug Discovery. *Trends Pharmacol Sci* **2009**, *30* (10), 536–545. https://doi.org/10.1016/J.TIPS.2009.07.001.

(44) Benjamin, E. J.; Blaha, M. J.; Chiuve, S. E.; Cushman, M.; Das, S. R.; Deo, R.; de Ferranti, S. D.; Floyd, J.; Fornage, M.; Gillespie, C.; Isasi, C. R.; Jim'nez, M. C.; Jordan, L. C.; Judd, S. E.; Lackland, D.; Lichtman, J. H.; Lisabeth, L.; Liu, S.; Longenecker, C. T.; MacKey, R. H.; Matsushita, K.; Mozaffarian, D.; Mussolino, M. E.; Nasir, K.; Neumar, R. W.; Palaniappan, L.; Pandey, D. K.; Thiagarajan, R. R.; Reeves, M. J.; Ritchey, M.; Rodriguez, C. J.; Roth, G. A.; Rosamond, W. D.; Sasson, C.; Towfghi, A.; Tsao, C. W.; Turner, M. B.; Virani, S. S.; Voeks, J. H.; Willey, J. Z.; Wilkins, J. T.; Wu, J. H. Y.; Alger, H. M.; Wong, S. S.; Muntner, P. Heart Disease and Stroke Statistics—2017: A Report From the American Heart Association. *Circulation* **2017**, *135* (10), e146. https://doi.org/10.1161/CIR.0000000000000485.

(45) *Hearts: technical package for cardiovascular disease management in primary health care*. https://apps.who.int/iris/handle/10665/252661 (accessed 2022-06-15).

(46) Ribas, J.; Sadeghi, H.; Manbachi, A.; Leijten, J.; Brinegar, K.; Zhang, Y. S.; Ferreira, L.; Khademhosseini, A. Cardiovascular Organ-on-a-Chip Platforms for Drug Discovery and Development. *Appl In Vitro Toxicol* **2016**, *2* (2), 82. https://doi.org/10.1089/AIVT.2016.0002.

(47) Li, X.; Zhang, R.; Zhao, B.; Lossin, C.; Cao, Z. Cardiotoxicity Screening: A Review of Rapid-Throughput in Vitro Approaches. *Arch Toxicol* **2016**, *90* (8), 1803–1816. https://doi.org/10.1007/S00204-015-1651-1.

(48) Pai, V. B.; Nahata, M. C. *Cardiotoxicity of Chemotherapeutic Agents Incidence, Treatment and Prevention*.

(49) Arcamone, F.; Cassinelli, G.; Fantini, G.; Grein, A.; Orezzi, P.; Pol, C.; Spalla, C. Adriamycin, 14-hydroxydaimomycin, a New Antitumor Antibiotic from S.

Peucetius Var. Caesius. *Biotechnol Bioeng* **1969**, *11* (6), 1101–1110. https://doi.org/10.1002/bit.260110607.

(50) Sheibani, M.; Azizi, Y.; Shayan, M.; Nezamoleslami, S.; Eslami, F.; Farjoo, M. H.; Dehpour, A. R. Doxorubicin-Induced Cardiotoxicity: An Overview on Pre-Clinical Therapeutic Approaches. *Cardiovascular Toxicology*. Springer April 1, 2022, pp 292–310. https://doi.org/10.1007/s12012-022-09721-1.

(51) de Angelis, A.; Urbanek, K.; Cappetta, D.; Piegari, E.; Ciuffreda, L. P.; Rivellino, A.; Russo, R.; Esposito, G.; Rossi, F.; Berrino, L. Doxorubicin Cardiotoxicity and Target Cells: A Broader Perspective. *Cardio-Oncology* **2016**, *2* (1). https://doi.org/10.1186/s40959-016-0012-4.

(52) Sardão, V. A.; Oliveira, P. J.; Holy, J.; Oliveira, C. R.; Wallace, K. B. Morphological Alterations Induced by Doxorubicin on H9c2 Myoblasts: Nuclear, Mitochondrial, and Cytoskeletal Targets. *Cell Biol Toxicol* **2009**, *25* (3), 227–243. https://doi.org/10.1007/S10565-008-9070-1.

(53) Wallace, K. B. Doxorubicin-Induced Cardiac Mitochondrionopathy. *Pharmacol Toxicol* **2003**, *93* (3), 105–115. https://doi.org/10.1034/J.1600-0773.2003.930301.X.

(54) Onbas, R.; Bilginer, R.; Arslan Yildiz, A. On-Chip Drug Screening Technologies for Nanopharmaceutical and Nanomedicine Applications. *Environmental Chemistry for a Sustainable World* **2021**, *1*, 311–346. https://doi.org/10.1007/978-3-030-44925-4_8.

(55) Rak-Raszewska, A.; Vainio, S. Nephrogenesis in Organoids to Develop Novel Drugs and Progenitor Cell Based Therapies. *Eur J Pharmacol* **2016**, *790*, 3–11. https://doi.org/10.1016/J.EJPHAR.2016.07.011.

(56) Jensen, G.; Morrill, C.; Huang, Y. 3D Tissue Engineering, an Emerging Technique for Pharmaceutical Research. *Acta Pharm Sin B* **2018**, *8* (5), 756–766. https://doi.org/10.1016/J.APSB.2018.03.006.

(57) Eder, A.; Vollert, I.; Hansen, A.; Eschenhagen, T. Human Engineered Heart Tissue as a Model System for Drug Testing. *Adv Drug Deliv Rev* **2016**, *96*, 214–224. https://doi.org/10.1016/J.ADDR.2015.05.010.

(58) Breslin, S.; O'Driscoll, L. Three-Dimensional Cell Culture: The Missing Link in Drug Discovery. *Drug Discovery Today*. March 2013, pp 240–249. https://doi.org/10.1016/j.drudis.2012.10.003.

(59) Edmondson, R.; Broglie, J. J.; Adcock, A. F.; Yang, L. Three-Dimensional Cell Culture Systems and Their Applications in Drug Discovery and Cell-Based Biosensors. *Assay and Drug Development Technologies*. Mary Ann Liebert Inc. May 1, 2014, pp 207–218. https://doi.org/10.1089/adt.2014.573.

(60) Bracken, M. B. Why Animal Studies Are Often Poor Predictors of Human Reactions to Exposure. *Journal of the Royal Society of Medicine*. March 1, 2009, pp 120–122. https://doi.org/10.1258/jrsm.2008.08k033.

(61) Park, J.; Wetzel, I.; Dréau, D.; Cho, H. 3D Miniaturization of Human Organs for Drug Discovery. *Advanced Healthcare Materials*. Wiley-VCH Verlag January 24, 2018. https://doi.org/10.1002/adhm.201700551.

(62) Astashkina, A.; Mann, B.; Grainger, D. W. A Critical Evaluation of in Vitro Cell Culture Models for High-Throughput Drug Screening and Toxicity. *Pharmacol Ther* **2012**, *134* (1), 82–106. https://doi.org/10.1016/J.PHARMTHERA.2012.01.001.

(63) Meli, L.; Jordan, E. T.; Clark, D. S.; Linhardt, R. J.; Dordick, J. S. Influence of a Three-Dimensional, Microarray Environment on Human Cell Culture in Drug Screening Systems. *Biomaterials* **2012**, *33* (35), 9087–9096. https://doi.org/10.1016/J.BIOMATERIALS.2012.08.065.

(64) Longati, P.; Jia, X.; Eimer, J.; Wagman, A.; Witt, M. R.; Rehnmark, S.; Verbeke, C.; Toftgård, R.; Löhr, M.; Heuchel, R. L. 3D Pancreatic Carcinoma Spheroids Induce a Matrix-Rich, Chemoresistant Phenotype Offering a Better Model for Drug Testing. *BMC Cancer* **2013**, *13* (1), 1–13. https://doi.org/10.1186/1471-2407-13-95/FIGURES/9.

(65) Poloznikov, A. A.; Nikulin, S. v.; Bolotina, L. v.; Gaisina, I. N.; Alexeev, B. Y. Comparison of 2D and 3D Cell Cultures of Colorectal Adenocarcinoma as Models for Drug Screening. *Russian Chemical Bulletin 2019 68:12* **2020**, *68* (12), 2377–2380. https://doi.org/10.1007/S11172-019-2716-8.

(66) Elliott, N. T.; Yuan, F. A Review of Three-Dimensional in Vitro Tissue Models for Drug Discovery and Transport Studies. *Journal of Pharmaceutical Sciences*. John Wiley and Sons Inc. 2011, pp 59–74. https://doi.org/10.1002/jps.22257.

(67) Gurski, L. A.; Petrelli, N. J.; Jia, X.; Farach-Carson, M. C. 3D Matrices for Anti-Cancer Drug Testing and Development. *http://dx.doi.org/10.1080/10463356.2010.11883480* **2017**, *25* (1), 20–25. https://doi.org/10.1080/10463356.2010.11883480.

(68) Langhans, S. A. Three-Dimensional in Vitro Cell Culture Models in Drug Discovery and Drug Repositioning. *Front Pharmacol* **2018**, *9* (JAN), 6. https://doi.org/10.3389/FPHAR.2018.00006/BIBTEX.

(69) Wilson, C. J.; Clegg, R. E.; Leavesley, D. I.; Pearcy, M. J. Mediation of Biomaterial-Cell Interactions by Adsorbed Proteins: A Review. *Tissue Eng* **2005**, *11* (1–2), 1–18. https://doi.org/10.1089/TEN.2005.11.1.

(70) Reynaud, E. Three-Dimensional Tissue Cultures: Current Trends and Beyond. *Article in Cell and Tissue Research* **2012**. https://doi.org/10.1007/s00441-012-1441-5.

(71) Anton, D.; Burckel, H.; Josset, E.; Noel, G. Three-Dimensional Cell Culture: A Breakthrough in Vivo. *Int J Mol Sci* **2015**, *16* (3), 5517–5527. https://doi.org/10.3390/IJMS16035517.

(72) Tung, Y. C.; Hsiao, A. Y.; Allen, S. G.; Torisawa, Y. S.; Ho, M.; Takayama, S. High-Throughput 3D Spheroid Culture and Drug Testing Using a 384 Hanging Drop Array. *Analyst* **2011**, *136* (3), 473–478. https://doi.org/10.1039/c0an00609b.

(73) Mehta, G.; Hsiao, A. Y.; Ingram, M.; Luker, G. D.; Takayama, S. Opportunities and Challenges for Use of Tumor Spheroids as Models to Test Drug Delivery and Efficacy. *Journal of Controlled Release* **2012**, *164* (2), 192–204. https://doi.org/10.1016/j.jconrel.2012.04.045.

(74) Leung, B. M.; Lesher-Perez, S. C.; Matsuoka, T.; Moraes, C.; Takayama, S. Media Additives to Promote Spheroid Circularity and Compactness in Hanging Drop Platform. *Biomater Sci* **2015**, *3* (2), 336–344. https://doi.org/10.1039/c4bm00319e.

(75) Fang, G.; Lu, H.; Law, A.; Gallego-Ortega, D.; Jin, D.; Lin, G. Gradient-Sized Control of Tumor Spheroids on a Single Chip. *Lab Chip* **2019**, *19* (24), 4093–4103. https://doi.org/10.1039/C9LC00872A.

(76) Türker, E.; Demirçak, N.; Arslan-Yildiz, A. Scaffold-Free Three-Dimensional Cell Culturing Using Magnetic Levitation. *Biomater Sci* **2018**, *6* (7), 1745–1753. https://doi.org/10.1039/c8bm00122g.

(77) Cui, X.; Hartanto, Y.; Zhang, H. Advances in Multicellular Spheroids Formation. *J R Soc Interface* **2017**, *14* (127). https://doi.org/10.1098/RSIF.2016.0877.

(78) Lin, R. Z.; Chang, H. Y. Recent Advances in Three-Dimensional Multicellular Spheroid Culture for Biomedical Research. *Biotechnol J* **2008**, *3* (9–10), 1172–1184. https://doi.org/10.1002/BIOT.200700228.

(79) Shi, W.; Kwon, J.; Huang, Y.; Tan, J.; Uhl, C. G.; He, R.; Zhou, C.; Liu, Y. Facile Tumor Spheroids Formation in Large Quantity with Controllable Size and High Uniformity. *Scientific Reports 2018 8:1* **2018**, *8* (1), 1–9. https://doi.org/10.1038/s41598-018-25203-3.

(80) Timm, D. M.; Chen, J.; Sing, D.; Gage, J. A.; Haisler, W. L.; Neeley, S. K.; Raphael, R. M.; Dehghani, M.; Rosenblatt, K. P.; Killian, T. C.; Tseng, H.; Souza, G. R. A High-Throughput Three-Dimensional Cell Migration Assay for Toxicity Screening with Mobile Device-Based Macroscopic Image Analysis. *Sci Rep* **2013**, *3*. https://doi.org/10.1038/srep03000.

(81) Leonard, F.; Godin, B. 3d in Vitro Model for Breast Cancer Research Using Magnetic Levitation and Bioprinting Method. In *Methods in Molecular Biology*; Humana Press Inc., 2016; Vol. 1406, pp 239–251. https://doi.org/10.1007/978-1-4939-3444-7_21.

(82) Tseng, H.; Gage, J. A.; Haisler, W. L.; Neeley, S. K.; Shen, T.; Hebel, C.; Barthlow, H. G.; Wagoner, M.; Souza, G. R. A High-Throughput in Vitro Ring Assay for Vasoactivity Using Magnetic 3D Bioprinting. *Sci Rep* **2016**, *6* (1). https://doi.org/10.1038/srep30640.

(83) Ma, X.; Qu, X.; Zhu, W.; Li, Y. S.; Yuan, S.; Zhang, H.; Liu, J.; Wang, P.; Lai, C. S. E.; Zanella, F.; Feng, G. S.; Sheikh, F.; Chien, S.; Chen, S. Deterministically Patterned Biomimetic Human IPSC-Derived Hepatic Model via

Rapid 3D Bioprinting. *Proc Natl Acad Sci U S A* **2016**, *113* (8), 2206–2211. https://doi.org/10.1073/pnas.1524510113.

(84) Qi, H.; Huang, G.; Han, Y. L.; Lin, W.; Li, X.; Wang, S.; Lu, T. J.; Xu, F. In Vitro Spatially Organizing the Differentiation in Individual Multicellular Stem Cell Aggregates. *Critical Reviews in Biotechnology*. Taylor and Francis Ltd January 2, 2016, pp 20–31. https://doi.org/10.3109/07388551.2014.922917.

(85) Ruiz, S. A.; Chen, C. S. Emergence of Patterned Stem Cell Differentiation Within Multicellular Structures. *Stem Cells* **2008**, *26* (11), 2921–2927. https://doi.org/10.1634/STEMCELLS.2008-0432.

(86) Ino, K.; Okochi, M.; Honda, H. Application of Magnetic Force-Based Cell Patterning for Controlling Cell-Cell Interactions in Angiogenesis. *Biotechnol Bioeng* **2009**, *102* (3), 882–890. https://doi.org/10.1002/bit.22104.

(87) Brown, A.; Burke, G. A.; Meenan, B. J. Patterned Cell Culture Substrates Created by Hot Embossing of Tissue Culture Treated Polystyrene. *J Mater Sci Mater Med* **2013**, *24* (12), 2797–2807. https://doi.org/10.1007/s10856-013-5011-5.

(88) He, W.; Halberstadt, C. R.; Gonsalves, K. E. Lithography Application of a Novel Photoresist for Patterning of Cells. *Biomaterials* **2004**, *25* (11), 2055–2063. https://doi.org/10.1016/j.biomaterials.2003.08.055.

(89) Shrirao, A. B.; Hussain, A.; Cho, C. H.; Perez-Castillejos, R. Adhesive-Tape Soft Lithography for Patterning Mammalian Cells: Application to Wound-Healing Assays. *Biotechniques* **2012**, *53* (5), 315–318. https://doi.org/10.2144/000113928.

(90) Hwang, H.; Kang, G.; Yeon, J. H.; Nam, Y.; Park, J. K. Direct Rapid Prototyping of PDMS from a Photomask Film for Micropatterning of Biomolecules and Cells. *Lab Chip* **2009**, *9* (1), 167–170. https://doi.org/10.1039/B810341K.

(91) Roth, E. A.; Xu, T.; Das, M.; Gregory, C.; Hickman, J. J.; Boland, T. Inkjet Printing for High-Throughput Cell Patterning. *Biomaterials* **2004**, *25* (17), 3707–3715. https://doi.org/10.1016/J.BIOMATERIALS.2003.10.052.

(92) Wu, Y.; Ao, Z.; Chen, B.; Muhsen, M.; Bondesson, M.; Lu, X.; Guo, F. Acoustic Assembly of Cell Spheroids in Disposable Capillaries. *Nanotechnology* **2018**, *29* (50). https://doi.org/10.1088/1361-6528/aae4f1.

(93) Guven, S.; Chen, P.; Inci, F.; Tasoglu, S.; Erkmen, B.; Demirci, U. Multiscale Assembly for Tissue Engineering and Regenerative Medicine. *Trends Biotechnol* **2015**, *33* (5), 269–279. https://doi.org/10.1016/J.TIBTECH.2015.02.003.

(94) Ino, K.; Ito, A.; Honda, H. Cell Patterning Using Magnetite Nanoparticles and Magnetic Force. *Biotechnol Bioeng* **2007**, *97* (5), 1309–1317. https://doi.org/10.1002/bit.21322.

(95) Frasca, G.; Gazeau, F.; Wilhelm, C. Formation of a Three-Dimensional Multicellular Assembly Using Magnetic Patterning. *Langmuir* **2009**, *25* (4), 2348–2354. https://doi.org/10.1021/la8030792.

(96) Souza, G. R.; Tseng, H.; Gage, J. A.; Mani, A.; Desai, P.; Leonard, F.; Liao, A.; Longo, M.; Refuerzo, J. S.; Godin, B. Magnetically Bioprinted Human Myometrial 3D Cell Rings as a Model for Uterine Contractility. *Int J Mol Sci* **2017**, *18* (4). https://doi.org/10.3390/ijms18040683.

(97) Abdel Fattah, A. R.; Mishriki, S.; Kammann, T.; Sahu, R. P.; Geng, F.; Puri, I. K. 3D Cellular Structures and Co-Cultures Formed through the Contactless Magnetic Manipulation of Cells on Adherent Surfaces. *Biomater Sci* **2018**, *6* (3), 683–694. https://doi.org/10.1039/c7bm01050h.

(98) Gan, J.; Chen, H.; Zhou, F.; Huang, H.; Zheng, J.; Song, W.; Yuan, L.; Wu, Z. Fabrication of Cell Pattern on Poly(Dimethylsiloxane) by Vacuum Ultraviolet Lithography. *Colloids Surf B Biointerfaces* **2010**, *76* (1), 381–385. https://doi.org/10.1016/J.COLSURFB.2009.11.013.

(99) Deguchi, S.; Nagasawa, Y.; Saito, A. C.; Matsui, T. S.; Yokoyama, S.; Sato, M. Development of Motorized Plasma Lithography for Cell Patterning. *Biotechnol Lett* **2014**, *36* (3), 507–513. https://doi.org/10.1007/S10529-013-1391-3.

(100) Offenhäusser, A.; Böcker-Meffert, S.; Decker, T.; Helpenstein, R.; Gasteier, P.; Groll, J.; Möller, M.; Reska, A.; Schäfer, S.; Schulte, P.; Vogt-Eisele, A. Microcontact Printing of Proteins for Neuronal Cell Guidance. *Soft Matter*. Royal Society of Chemistry 2007, pp 290–298. https://doi.org/10.1039/b607615g.

(101) Jang, M. J.; Nam, Y. Aqueous Micro-Contact Printing of Cell-Adhesive Biomolecules for Patterning Neuronal Cell Cultures. *Biochip J* **2012**, *6* (2), 107–113. https://doi.org/10.1007/s13206-012-6201-9.

(102) Xia, Y.; Rogers, J. A.; Paul, K. E.; Whitesides, G. M. Unconventional Methods for Fabricating and Patterning Nanostructures. *Chem Rev* **1999**, *99* (7), 1823–1848. https://doi.org/10.1021/cr980002q.

(103) Matsusaki, M.; Sakaue, K.; Kadowaki, K.; Akashi, M. Three-Dimensional Human Tissue Chips Fabricated by Rapid and Automatic Inkjet Cell Printing. *Adv Healthc Mater* **2013**, *2* (4), 534–539. https://doi.org/10.1002/adhm.201200299.

(104) Xu, T.; Zhao, W.; Zhu, J. M.; Albanna, M. Z.; Yoo, J. J.; Atala, A. Complex Heterogeneous Tissue Constructs Containing Multiple Cell Types Prepared by Inkjet Printing Technology. *Biomaterials* **2013**, *34* (1), 130–139. https://doi.org/10.1016/j.biomaterials.2012.09.035.

(105) Martinez-Rivas, A.; González-Quijano, G. K.; Proa-Coronado, S.; Séverac, C.; Dague, E. Methods of Micropatterning and Manipulation of Cells for Biomedical Applications. *Micromachines*. MDPI AG November 29, 2017. https://doi.org/10.3390/mi8120347.

(106) Zhang, M.; Krishnamoorthy, S.; Song, H.; Zhang, Z.; Xu, C. Ligament Flow during Drop-on-Demand Inkjet Printing of Bioink Containing Living Cells. *J Appl Phys* **2017**, *121* (12). https://doi.org/10.1063/1.4978744.

(107) Zhu, Y.; Serpooshan, V.; Wu, S.; Demirci, U.; Chen, P.; Güven, S. Tissue Engineering of 3D Organotypic Microtissues by Acoustic Assembly. *Methods in Molecular Biology* **2019**, *1576*, 301–312. https://doi.org/10.1007/7651_2017_68/COVER.

(108) Chen, P.; Chen, P.; Wu, H.; Lee, S.; Sharma, A.; Hu, D. A.; Venkatraman, S.; Ganesan, A. V.; Usta, O. B.; Yarmush, M.; Yang, F.; Wu, J. C.; Demirci, U.; Wu, S. M. Bioacoustic-Enabled Patterning of Human IPSC-Derived Cardiomyocytes into 3D Cardiac Tissue. *Biomaterials* **2017**, *131*, 47–57. https://doi.org/10.1016/J.BIOMATERIALS.2017.03.037.

(109) Souza, G. R.; Tseng, H.; Gage, J. A.; Mani, A.; Desai, P.; Leonard, F.; Liao, A.; Longo, M.; Refuerzo, J. S.; Godin, B. Magnetically Bioprinted Human Myometrial 3D Cell Rings as a Model for Uterine Contractility. *Int J Mol Sci* **2017**, *18* (4). https://doi.org/10.3390/ijms18040683.

(110) Timm, D. M.; Chen, J.; Sing, D.; Gage, J. A.; Haisler, W. L.; Neeley, S. K.; Raphael, R. M.; Dehghani, M.; Rosenblatt, K. P.; Killian, T. C.; Tseng, H.; Souza, G. R. A High-Throughput Three-Dimensional Cell Migration Assay for Toxicity Screening with Mobile Device-Based Macroscopic Image Analysis. *Sci Rep* **2013**, *3*. https://doi.org/10.1038/srep03000.

(111) Tseng, H.; Gage, J. A.; Haisler, W. L.; Neeley, S. K.; Shen, T.; Hebel, C.; Barthlow, H. G.; Wagoner, M.; Souza, G. R. A High-Throughput in Vitro Ring Assay for Vasoactivity Using Magnetic 3D Bioprinting. *Sci Rep* **2016**, *6* (1). https://doi.org/10.1038/srep30640.

(112) Gupta, T.; Aithal, S.; Mishriki, S.; Sahu, R. P.; Geng, F.; Puri, I. K. Label-Free Magnetic-Field-Assisted Assembly of Layer-on-Layer Cellular Structures. *ACS Biomater Sci Eng* **2020**, *6* (7), 4294–4303. https://doi.org/10.1021/ACSBIOMATERIALS.0C00233/ASSET/IMAGES/LARGE/AB0C00233_0008.JPEG.

(113) Parfenov, V. A.; Khesuani, Y. D.; Petrov, S. v; Karalkin, P. A.; Koudan, E. v; Nezhurina, E. K.; das Pereira, F.; Krokhmal, A. A.; Gryadunova, A. A.; Bulanova, E. A.; Vakhrushev, I. v; Babichenko, I. I.; Kasyanov, V.; Petrov, O. F.; Vasiliev, M. M.; Brakke, K.; Belousov, S. I.; Grigoriev, T. E.; Osidak, E. O.; Rossiyskaya, E. I.; Buravkova, L. B.; Kononenko, O. D.; Demirci, U.; Mironov, V. A. *B I O E N G I N E E R I N G Magnetic Levitational Bioassembly of 3D Tissue Construct in Space*; 2020. http://advances.sciencemag.org/.

(114) Parfenov, V. A.; Koudan, E. v.; Bulanova, E. A.; Karalkin, P. A.; das Pereira, F.; Norkin, N. E.; Knyazeva, A. D.; Gryadunova, A. A.; Petrov, O. F.; Vasiliev, M. M.; Myasnikov, M. I.; Chernikov, V. P.; Kasyanov, V. A.; Marchenkov, A. Y.; Brakke, K.; Khesuani, Y. D.; Demirci, U.; Mironov, V. A. Scaffold-Free, Label-Free and Nozzle-Free Biofabrication Technology Using Magnetic Levitational Assembly. *Biofabrication* **2018**, *10* (3). https://doi.org/10.1088/1758-5090/aac900.

(115) Turker, E.; Arslan-Yildiz, A. Recent Advances in Magnetic Levitation: A Biological Approach from Diagnostics to Tissue Engineering. *ACS Biomaterials Science and Engineering*. American Chemical Society March 12, 2018, pp 787–799. https://doi.org/10.1021/acsbiomaterials.7b00700.

(116) Tasoglu, S.; Yu, C. H.; Liaudanskaya, V.; Guven, S.; Migliaresi, C.; Demirci, U. Magnetic Levitational Assembly for Living Material Fabrication. *Adv Healthc Mater* **2015**, *4* (10), 1469–1476. https://doi.org/10.1002/adhm.201500092.

(117) Anil-Inevi, M.; Delikoyun, K.; Mese, G.; Tekin, H. C.; Ozcivici, E. Magnetic Levitation Assisted Biofabrication, Culture, and Manipulation of 3D Cellular Structures Using a Ring Magnet Based Setup. *Biotechnol Bioeng* **2021**, *118* (12), 4771–4785. https://doi.org/10.1002/BIT.27941.

(118) Onbas, R.; Arslan Yildiz, A. Fabrication of Tunable 3D Cellular Structures in High Volume Using Magnetic Levitation Guided Assembly. *ACS Appl Bio Mater* **2021**, *4* (2), 1794–1802. https://doi.org/10.1021/acsabm.0c01523.

(119) Souza, G. R.; Molina, J. R.; Raphael, R. M.; Ozawa, M. G.; Stark, D. J.; Levin, C. S.; Bronk, L. F.; Ananta, J. S.; Mandelin, J.; Georgescu, M. M.; Bankson, J. A.; Gelovani, J. G.; Killian, T. C.; Arap, W.; Pasqualini, R. Three-Dimensional Tissue Culture Based on Magnetic Cell Levitation. *Nat Nanotechnol* **2010**, *5* (4), 291–296. https://doi.org/10.1038/nnano.2010.23.

(120) Haisler, W. L.; Timm, D. M.; Gage, J. A.; Tseng, H.; Killian, T. C.; Souza, G. R. Three-Dimensional Cell Culturing by Magnetic Levitation. *Nat Protoc* **2013**, *8* (10), 1940–1949. https://doi.org/10.1038/nprot.2013.125.

(121) Tseng, H.; Gage, J. A.; Raphael, R. M.; Moore, R. H.; Killian, T. C.; Grande-Allen, K. J.; Souza, G. R. Assembly of a Three-Dimensional Multitype Bronchiole Coculture Model Using Magnetic Levitation. *Tissue Eng Part C Methods* **2013**, *19* (9), 665–675. https://doi.org/10.1089/ten.tec.2012.0157.

(122) Tocchio, A.; Durmus, N. G.; Sridhar, K.; Mani, V.; Coskun, B.; el Assal, R.; Demirci, U. Magnetically Guided Self-Assembly and Coding of 3D Living Architectures. *Advanced Materials* **2018**, *30* (4). https://doi.org/10.1002/ADMA.201705034.

(123) Matijevi, E.; Scheiner, P. *Ferric Hydrous Oxide Sols II1. Preparation of Uniform Particles by Hydrolysis of Fe(Lll)-Chloride,-Nitrate, and-Perchlorate Solutions 1"2*; 1978.

(124) Cavazzuti, M. *Optimization Methods: From Theory to Design Critical Flows View Project Tunnel Ventilation View Project*; 2013. https://www.researchgate.net/publication/261750290.

(125) Ma, Y.; Zhang, Y.; Zhao, S.; Wang, Y.; Wang, S.; Zhou, Y.; Li, N.; Xie, H.; Yu, W.; Liu, Y.; Wang, W.; Ma, X. Modeling and Optimization of Membrane Preparation Conditions of the Alginate-Based Microcapsules with Response Surface Methodology. *J Biomed Mater Res A* **2012**, *100 A* (4), 989–998. https://doi.org/10.1002/jbm.a.34032.

(126) Myers H Raymond, M. C. D. & A.-C. C. C. Response Surface Methodology: Process and Product Optimization Using ... -. **2016**, 894.

(127) Mishriki, S.; Aithal, S.; Gupta, T.; Sahu, R. P.; Geng, F.; Puri, I. K. Fibroblasts Accelerate Formation and Improve Reproducibility of 3D Cellular Structures Printed with Magnetic Assistance. *Research* **2020**, *2020*, 1–15. https://doi.org/10.34133/2020/3970530.

(128) Hirschhaeuser, F.; Menne, H.; Dittfeld, C.; West, J.; Mueller-Klieser, W.; Kunz-Schughart, L. A. Multicellular Tumor Spheroids: An Underestimated Tool Is Catching up Again. *J Biotechnol* **2010**, *148* (1), 3–15. https://doi.org/10.1016/j.jbiotec.2010.01.012.

(129) Lin, R. Z.; Chang, H. Y. Recent Advances in Three-Dimensional Multicellular Spheroid Culture for Biomedical Research. *Biotechnology Journal*. Wiley-VCH Verlag 2008, pp 1172–1184. https://doi.org/10.1002/biot.200700228.

(130) Mueller-Klieser, W. Tumor Biology and Experimental Therapeutics. *Crit Rev Oncol Hematol* **2000**, *36* (2–3), 123–139. https://doi.org/10.1016/S1040-8428(00)00082-2.

(131) Nath, S.; Devi, G. R. Three-Dimensional Culture Systems in Cancer Research: Focus on Tumor Spheroid Model. *Pharmacol Ther* **2016**, *163*, 94–108. https://doi.org/10.1016/J.PHARMTHERA.2016.03.013.

(132) Däster, S.; Amatruda, N.; Calabrese, D.; Ivanek, R.; Turrini, E.; Droeser, R. A.; Zajac, P.; Fimognari, C.; Spagnoli, G. C.; Iezzi, G.; Mele, V.; Muraro, M. G. *Induction of Hypoxia and Necrosis in Multicellular Tumor Spheroids Is Associated with Resistance to Chemotherapy Treatment*; 2017; Vol. 8. www.impactjournals.com/oncotarget/.

(133) Weaver, V. M.; Leliè, S.; Lakins, J. N.; Chrenek, M. A.; Jones, J. C. R.; Giancotti, F.; Werb, Z.; Bissell, M. J. *4 Integrin-Dependent Formation of Polarized Three-Dimensional Architecture Confers Resistance to Apoptosis in Normal and Malignant Mammary Epithelium*.

(134) Fontoura, J. C.; Viezzer, C.; dos Santos, F. G.; Ligabue, R. A.; Weinlich, R.; Puga, R. D.; Antonow, D.; Severino, P.; Bonorino, C. Comparison of 2D and 3D Cell Culture Models for Cell Growth, Gene Expression and Drug Resistance. *Mater Sci Eng C Mater Biol Appl* **2020**, *107*. https://doi.org/10.1016/J.MSEC.2019.110264.

(135) Theodoraki, M. A.; Rezende, C. O.; Chantarasriwong, O.; Corben, A. D.; Theodorakis, E. A.; Alpaugh, M. L. *Spontaneously-Forming Spheroids as an in Vitro Cancer Cell Model for Anticancer Drug Screening*; 2015; Vol. 6. www.impactjournals.com/oncotarget/.

(136) Rezende, R. A.; Pereira, F. D. A. S.; Kasyanov, V.; Kemmoku, D. T.; Maia, I.; da Silva, J. V. L.; Mironov, V. Scalable Biofabrication of Tissue Spheroids for Organ Printing. In *Procedia CIRP*; Elsevier B.V., 2013; Vol. 5, pp 276–281. https://doi.org/10.1016/j.procir.2013.01.054.

(137) Yu, Y.; Ozbolat, I. T. Tissue Strands as "Bioink" for Scale-up Organ Printing. In *2014 36th Annual International Conference of the IEEE Engineering in Medicine and Biology Society, EMBC 2014*; Institute of Electrical and Electronics Engineers Inc., 2014; pp 1428–1431. https://doi.org/10.1109/EMBC.2014.6943868.

(138) Kawai, Y.; Tohyama, S.; Shimizu, H.; Fukuda, K.; Kobayashi, E. *Pigs as Models of Preclinical Studies and In Vivo Bioreactors for Generation of Human Organs*. www.intechopen.com.

(139) Lee, J. I.; Sato, M.; Kim, H. W.; Mochida, J. Transplantatation of Scaffold-Free Spheroids Composed of Synovium-Derived Cells and Chondrocytes for the Treatment of Cartilage Defects of the Knee. *Eur Cell Mater* **2011**, *22*. https://doi.org/10.22203/ecm.v022a21.

(140) Ota, H.; Miki, N. Microtechnology-Based Three-Dimensional Spheroid Formation. *Front Biosci (Elite Ed)* **2013**, *5* (1), 37–48. https://doi.org/10.2741/E594.

(141) Torisawa, Y.-S.; Takag1, A.; Shiku, H.; Yasukawa, T.; Matsue, T. *A Multicellular Spheroid-Based Drug Sensitivity Test by Scanning Electrochemical Microscopy*; 2005; Vol. 13.

(142) Vindin, H.; Gunning, P. Cytoskeletal Tropomyosins: Choreographers of Actin Filament Functional Diversity. *Journal of Muscle Research and Cell Motility*. August 2013, pp 261–274. https://doi.org/10.1007/s10974-013-9355-8.

(143) Smyrek, I.; Mathew, B.; Fischer, S. C.; Lissek, S. M.; Becker, S.; Stelzer, E. H. K. E-Cadherin, Actin, Microtubules and FAK Dominate Different Spheroid Formation Phases and Important Elements of Tissue Integrity. *Biol Open* **2019**, *8* (1). https://doi.org/10.1242/bio.037051.

(144) Kobayashi, H.; Mizuki, T.; Wada, A.; Izumi, F. *CELL-CELL CONTACT MODULATES EXPRESSION OF CELL ADHESION MOLECULE L1 IN PC12 CELLS*; 1992; Vol. 49.

(145) Ivascu, A.; Kubbies, M. Diversity of Cell-Mediated Adhesions in Breast Cancer Spheroids. *Int J Oncol* **2007**, *31* (6), 1403–1413. https://doi.org/10.3892/IJO.31.6.1403/HTML.

(146) Wahl, J. K.; Kim, Y. J.; Cullen, J. M.; Johnson, K. R.; Wheelock, M. J. N-Cadherin-Catenin Complexes Form Prior to Cleavage of the Proregion and Transport to the Plasma Membrane. *Journal of Biological Chemistry* **2003**, *278* (19), 17269–17276. https://doi.org/10.1074/jbc.M211452200.

(147) Ho, V. H. B.; Müller, K. H.; Barcza, A.; Chen, R.; Slater, N. K. H. Generation and Manipulation of Magnetic Multicellular Spheroids. *Biomaterials* **2010**, *31* (11), 3095–3102. https://doi.org/10.1016/j.biomaterials.2009.12.047.

(148) Kook, Y. M.; Jeong, Y.; Lee, K.; Koh, W. G. Design of Biomimetic Cellular Scaffolds for Co-Culture System and Their Application. *J Tissue Eng* **2017**, *8*. https://doi.org/10.1177/2041731417724640.

(149) Trédan, O.; Galmarini, C. M.; Patel, K.; Tannock, I. F. Drug Resistance and the Solid Tumor Microenvironment. *Journal of the National Cancer Institute*. October 2007, pp 1441–1454. https://doi.org/10.1093/jnci/djm135.

(150) Kassim, Y. L.; Tawil, E. al; Buquet, C.; Cerf, D. le; PierreVannier, J. Three Dimensional Tumor Engineering by Co-Culture of Breast Tumor and Endothelial Cells Using a Hyaluronic Acid Hydrogel Model. *J Clin Exp Oncol* **2017**, *06* (05). https://doi.org/10.4172/2324-9110.1000194.

(151) Idée, J. M.; Port, M.; Medina, C.; Lancelot, E.; Fayoux, E.; Ballet, S.; Corot, C. Possible Involvement of Gadolinium Chelates in the Pathophysiology of Nephrogenic Systemic Fibrosis: A Critical Review. *Toxicology* **2008**, *248* (2–3), 77–88. https://doi.org/10.1016/J.TOX.2008.03.012.

(152) Kleinman, H. K.; Philp, D.; Hoffman, M. P. Role of the Extracellular Matrix in Morphogenesis. *Current Opinion in Biotechnology*. Elsevier Ltd 2003, pp 526–532. https://doi.org/10.1016/j.copbio.2003.08.002.

(153) Sozen, B.; Jorgensen, V.; Weatherbee, B. A. T.; Chen, S.; Zhu, M.; Zernicka-Goetz, M. Reconstructing Aspects of Human Embryogenesis with Pluripotent Stem Cells. *Nature Communications 2021 12:1* **2021**, *12* (1), 1–13. https://doi.org/10.1038/s41467-021-25853-4.

(154) Sharma, S.; Jackson, P. G.; Makan, J. Cardiac Troponins. *J Clin Pathol* **2004**, *57* (10), 1025–1026. https://doi.org/10.1136/JCP.2003.015420.

(155) Gelb, B. D.; Chin, S. E. Genetics of Congenital Heart Disease. *Muscle* **2012**, *1*, 473–480. https://doi.org/10.1016/B978-0-12-381510-1.00034-X.

(156) Riedl, A.; Schlederer, M.; Pudelko, K.; Stadler, M.; Walter, S.; Unterleuthner, D.; Unger, C.; Kramer, N.; Hengstschläger, M.; Kenner, L.; Pfeiffer, D.; Krupitza, G.; Dolznig, H. Comparison of Cancer Cells in 2D vs 3D Culture Reveals Differences in AKT-MTOR-S6K Signaling and Drug Responses. *J Cell Sci* **2017**, *130* (1), 203–218. https://doi.org/10.1242/JCS.188102.

(157) Melissaridou, S.; Wiechec, E.; Magan, M.; Jain, M. V.; Chung, M. K.; Farnebo, L.; Roberg, K. The Effect of 2D and 3D Cell Cultures on Treatment Response, EMT Profile and Stem Cell Features in Head and Neck Cancer. *Cancer Cell Int* **2019**, *19* (1). https://doi.org/10.1186/S12935-019-0733-1.

(158) Sirenko, O.; Hancock, M. K.; Crittenden, C.; Hammer, M.; Keating, S.; Carlson, C. B.; Chandy, G. Phenotypic Assays for Characterizing Compound Effects on Induced Pluripotent Stem Cell-Derived Cardiac Spheroids. *Assay Drug Dev Technol* **2017**, *15* (6), 280–296. https://doi.org/10.1089/adt.2017.792.

(159) Cukierman, E.; Pankov, R.; Stevens, D. R.; Yamada, K. M. Taking Cell-Matrix Adhesions to the Third Dimension. *Science (1979)* **2001**, *294* (5547), 1708–1712. https://doi.org/10.1126/science.1064829.

(160) Pampaloni, F.; Reynaud, E. G.; Stelzer, E. H. K. The Third Dimension Bridges the Gap between Cell Culture and Live Tissue. *Nat Rev Mol Cell Biol* **2007**, *8* (10), 839–845. https://doi.org/10.1038/NRM2236.

(161) Tseng, H.; Gage, J. A.; Shen, T.; Haisler, W. L.; Neeley, S. K.; Shiao, S.; Chen, J.; Desai, P. K.; Liao, A.; Hebel, C.; Raphael, R. M.; Becker, J. L.; Souza, G. R. A Spheroid Toxicity Assay Using Magnetic 3D Bioprinting and Real-Time Mobile Device-Based Imaging. *Sci Rep* **2015**, *5*. https://doi.org/10.1038/srep13987.

(162) Beauchamp, P.; Jackson, C. B.; Ozhathil, L. C.; Agarkova, I.; Galindo, C. L.; Sawyer, D. B.; Suter, T. M.; Zuppinger, C. 3D Co-Culture of HiPSC-Derived Cardiomyocytes With Cardiac Fibroblasts Improves Tissue-Like Features of Cardiac Spheroids. *Front Mol Biosci* **2020**, *7*, 14. https://doi.org/10.3389/FMOLB.2020.00014/BIBTEX.

(163) Zhou, N.; Liu, C.; Lv, S.; Sun, D.; Qiao, Q.; Zhang, R.; Liu, Y.; Xiao, J.; Sun, G. Degradation Prediction Model and Stem Cell Growth of Gelatin-PEG Composite Hydrogel. *J Biomed Mater Res A* **2016**, *104* (12), 3149–3156. https://doi.org/10.1002/jbm.a.35847.

(164) Draget, K. I.; Smidsrød, O.; Skjåk-Bræk, G. Alginates from Algae. *Biopolymers Online* **2002**. https://doi.org/10.1002/3527600035.BPOL6008.

(165) Sosnik, A. Alginate Particles as Platform for Drug Delivery by the Oral Route: State-of-the-Art. *ISRN Pharm* **2014**, *2014*, 1–17. https://doi.org/10.1155/2014/926157.

(166) Draget, K. I.; Taylor, C. Chemical, Physical and Biological Properties of Alginates and Their Biomedical Implications. *Food Hydrocoll* **2011**, *25* (2), 251–256. https://doi.org/10.1016/j.foodhyd.2009.10.007.

(167) Radisic, M.; Malda, J.; Epping, E.; Geng, W.; Langer, R.; Vunjak-Novakovic, G. Oxygen Gradients Correlate with Cell Density and Cell Viability in Engineered Cardiac Tissue. *Biotechnol Bioeng* **2006**, *93* (2), 332–343. https://doi.org/10.1002/bit.20722.

(168) Daly, A. C.; Davidson, M. D.; Burdick, J. A. 3D Bioprinting of High Cell-Density Heterogeneous Tissue Models through Spheroid Fusion within Self-Healing Hydrogels. *Nat Commun* **2021**, *12* (1). https://doi.org/10.1038/s41467-021-21029-2.

(169) Gombotz, W. R.; Fong Wee, S. *Protein Release from Alginate Matrices*; 1998; Vol. 31.

(170) Grünhagen, T. *Characterisation of the Degrading Properties of Alginate under Influence of Citrate*; 2002.

(171) Cohen, J.; Zaleski, K. L.; Nourissat, G.; Julien, T. P.; Randolph, M. A.; Yaremchuk, M. J. Survival of Porcine Mesenchymal Stem Cells over the Alginate Recovered Cellular Method. *J Biomed Mater Res A* **2011**, *96 A* (1), 93–99. https://doi.org/10.1002/jbm.a.32961.

(172) Rodriguez, S.; Lau, H.; Corrales, N.; Heng, J.; Lee, S.; Stiner, R.; Alexander, M.; Lakey, J. R. T. Characterization of Chelator-Mediated Recovery of Pancreatic Islets from Barium-Stabilized Alginate Microcapsules. *Xenotransplantation* **2020**, *27* (1). https://doi.org/10.1111/xen.12554.

(173) Pour Hosseini, S. R.; Tavakoli, O.; Sarrafzadeh, M. H. Experimental Optimization of SC-CO2 Extraction of Carotenoids from Dunaliella Salina. *Journal of Supercritical Fluids* **2017**, *121*, 89–95. https://doi.org/10.1016/j.supflu.2016.11.006.

(174) Gurski, L. A.; Petrelli, N. J.; Jia, X.; Farach-Carson, M. C. 3D Matrices for Anti-Cancer Drug Testing and Development. *http://dx.doi.org/10.1080/10463356.2010.11883480* **2017**, *25* (1), 20–25. https://doi.org/10.1080/10463356.2010.11883480.

(175) Hongisto, V.; Jernström, S.; Fey, V.; Mpindi, J. P.; Kleivi Sahlberg, K.; Kallioniemi, O.; Perälä, M. High-Throughput 3D Screening Reveals Differences in Drug Sensitivities between Culture Models of JIMT1 Breast Cancer Cells. *PLoS One* **2013**, *8* (10), e77232. https://doi.org/10.1371/JOURNAL.PONE.0077232.

(176) Richard, S.; Silva, A. K. A.; Mary, G.; Ragot, H.; Perez, J. E.; Ménager, C.; Gazeau, F.; Boucenna, I.; Agbulut, O.; Wilhelm, C. 3D Magnetic Alignment of Cardiac Cells in Hydrogels. *ACS Appl Bio Mater* **2020**, *3* (10), 6802–6810. https://doi.org/10.1021/acsabm.0c00754.

(177) Zhang, Y. S.; Arneri, A.; Bersini, S.; Shin, S. R.; Zhu, K.; Goli-Malekabadi, Z.; Aleman, J.; Colosi, C.; Busignani, F.; Dell'Erba, V.; Bishop, C.; Shupe, T.; Demarchi, D.; Moretti, M.; Rasponi, M.; Dokmeci, M. R.; Atala, A.; Khademhosseini, A. Bioprinting 3D Microfibrous Scaffolds for Engineering Endothelialized Myocardium and Heart-on-a-Chip. *Biomaterials* **2016**, *110*, 45–59. https://doi.org/10.1016/j.biomaterials.2016.09.003.

(178) Liu, J.; He, J.; Liu, J.; Ma, X.; Chen, Q.; Lawrence, N.; Bioprinting, W. Z.-; 2019, undefined. Rapid 3D Bioprinting of in Vitro Cardiac Tissue Models Using Human Embryonic Stem Cell-Derived Cardiomyocytes. *Elsevier*.

(179) Noor, N.; Shapira, A.; Edri, R.; Gal, I.; Wertheim, L.; Dvir, T. 3D Printing of Personalized Thick and Perfusable Cardiac Patches and Hearts. *Advanced Science* **2019**, *6* (11), 1900344. https://doi.org/10.1002/ADVS.201900344.

(180) Roche, C. D.; Sharma, P.; Ashton, A. W.; Jackson, C.; Xue, M.; Gentile, C. Printability, Durability, Contractility and Vascular Network Formation in 3D Bioprinted Cardiac Endothelial Cells Using Alginate–Gelatin Hydrogels. *Front Bioeng Biotechnol* **2021**, *9*. https://doi.org/10.3389/fbioe.2021.636257.

(181) Maiullari, F.; Costantini, M.; Milan, M.; Pace, V.; Chirivì, M.; Maiullari, S.; Rainer, A.; Baci, D.; Marei, H. E. S.; Seliktar, D.; Gargioli, C.; Bearzi, C.; Rizzi,

R. A Multi-Cellular 3D Bioprinting Approach for Vascularized Heart Tissue Engineering Based on HUVECs and IPSC-Derived Cardiomyocytes. *Sci Rep* **2018**, *8* (1). https://doi.org/10.1038/s41598-018-31848-x.

(182) Zhu, B.; Yin, H. Alginate Lyase: Review of Major Sources and Classification, Properties, Structure-Function Analysis and Applications. *http://dx.doi.org/10.1080/21655979.2015.1030543* **2015**, *6* (3), 125–131. https://doi.org/10.1080/21655979.2015.1030543.

(183) Saini, H.; Navaei, A.; van Putten, A.; Nikkhah, M. 3D Cardiac Microtissues Encapsulated with the Co-Culture of Cardiomyocytes and Cardiac Fibroblasts. *Adv Healthc Mater* **2015**, *4* (13), 1961–1971. https://doi.org/10.1002/adhm.201500331.

VITA

Personal information

Rabia Önbaş

Education

PhD in Bioengineering 2017-2022, İzmir Institute of Technology, İzmir, Turkey
MSc in Biomedical Technologies 2015-2017, Ege University, İzmir, Turkey
B.S. in Bioengineering 2009-2014, Ege University, İzmir, Turkey

Project Experience

Collaboration project with Applied Stem Cell Technologies, Twente University supported by The Scientific and Technological Research Council of Turkey (TUBITAK), Developing 3D Cardiac Model by Using hPSC-derived Cardiomyocytes via Biopatterning for Drug Screening, Researcher, 2021-2022

Scientific Research Project (Izmir Institute of Technology), 2021IYTE-1-0065, Single Chain Cationic Polymer Dot with High Penetration use as a Fluorescent Probe for 3D Tumor Models, Researcher, 2021-2022

Scientific Research Project (Izmir Institute of Technology), 2020IYTE0006, Large-scale Spheroid Production and Characterization via Magnetic Levitation Method, Researcher, 2020-2021

The Scientific and Technological Research Council of Turkey (TUBITAK), 119Z569, Development of 3D Cardiac Model via Magnetic Levitation, Researcher, 2019-2020

Scholarships

The Scientific and Technological Research Council of Turkey (TUBITAK) 2214-A International Research Fellowship Programme for Ph.D. Students (Ph.D. collaboration project with University of Twente/The Netherlands) 2021-2022

The Scientific and Technological Research Council of Turkey (TUBITAK) 2211-A National Ph.D. Scholarship 2018-2022

Council of Higher Education Ph.D. Scholarship at 100/2000 Program – Biomaterials and Tissue Engineering 2017-2021

List of Selected Publications/Articles

Onbas, R., Arslan-Yildiz, A., Fabrication of Tunable 3D Cellular Structures in High Volume Using Magnetic Levitation Guided Assembly, ***ACS Appl. Bio Mater***. 2021, 4, 1794−1802

Onbas R., Bilginer, R., Arslan Yildiz, A. On-Chip Drug Screening Technologies for Nanopharmaceutical and Nanomedicine Applications. In: Yata VK, Ranjan S, Dasgupta N, Lichtfouse E, (eds) Nanopharmaceuticals: Principles and Applications Vol. 1. Environmental Chemistry for a Sustainable World, vol 46. Springer, 2021, Cham.

Köksal, B., **Onbas, R.**, Baskurt, M., Sahin, H., Arslan-Yildiz, A., Yildiz, U.H., Boosting up printability of biomacromolecule based bio-ink by modulation of hydrogen bonding pairs, ***European Polymer Journal,*** 2020, 141:110070

Onbas, R., Arslan-Yildiz, A., Biofabrication of 3D cardiac spheroids via magnetic levitation guided assembly for doxorubicin-induced cardiotoxicity study (under review).

Onbas, R., Arslan-Yildiz, A., Formulation of an alginate based bio-ink to fabricate biopatterned 3D cellular structures via contactless magnetic manipulation (in preparation).

List of Selected Publications/Poster and Oral Presentations

Onbas, R., Arslan-Yıldız, A. Biofabrication of scaffold-free 3D cellular structures using magnetic levitational assembly to study cardiac toxicity, TERMIS EU, 28.06-01.07.2022, Krakow/Poland (Oral Presentation)

Onbas, R., Arslan-Yıldız, A. Biopatterning of 3D cellular structures via contactless magnetic manipulation for drug screening, TERMIS EU, 28.06-01.07.2022, Krakow/Poland (Poster Presentation)

Onbas, R., Arslan-Yıldız, A. Development of 3D cardiac models via magnetic manipulation for drug screening studies, TERMIS 6th World Congress, 15-19 November 2021, Maastricht/ The Netherlands (Poster Presentation)

Onbas, R., Arslan-Yıldız, A. Scaffold-free biofabrication of 3D cellular structures via magnetic levitation, Xth International Biomechanics Congress, 26-27 March 2021, İzmir/ Turkey (Oral Presentation)